INVESTIGATIONS OF THE BIOGEOCHEMICAL AND HYDRODYNAMIC IMPACTS OF OPTICAL ATTENUATION BY COLORED DETRITAL MATTER IN AN EARTH SYSTEM MODEL

by

Grace E. Kim

A dissertation submitted to The Johns Hopkins University in conformity with the

requirements for the degree of Doctor of Philosophy.

Baltimore, Maryland

December, 2016

Abstract

Light in the surface ocean is necessary for photosynthesis by marine algae. It is also a major source of heating. Visible light diminishes approximately exponentially with increasing depth in the upper ocean. In most of the current generation of Earth System Models used for climate projection, the vertical profile of in-water shortwave radiation is calculated as an exponentially decaying function where the attenuation coefficient is parameterized in terms of phytoplankton photosynthetic pigment (chlorophyll-a) concentration. In doing so, the attenuation of light by all other aquatic constituents is assumed to co-vary with chlorophyll-a concentration. The work in this dissertation presents a revised parameterization for the light attenuation coefficient that varies as a function of chlorophyll-a concentration and the light absorption coefficient for colored detrital matter (CDM). By separating the contribution by CDM, it is free to vary independently. Two ESM model runs were conducted: the experimental run, where the light attenuation coefficient was calculated as a function of both chlorophyll-a concentration and light absorption by CDM and the control run, where the light attenuation coefficient was calculated as a function of chlorophyll-a concentration only. The geographical distribution of light absorption by CDM was pre-

ABSTRACT

scribed using an ocean color satellite data product using data retrieved from the Moderate

Resolution Imaging Spectroradiometer (MODIS) on the Aqua Earth-observing satellite.

The difference between the results of these two model runs showed increased light attenu-

ation by CDM decreased total ocean biological productivity, increased wintertime ice for-

mation and resulted in more extreme sea surface temperatures compared to the control run.

These studies are the first global-scale investigations of the biological and hydrodynamic

impacts of optical attenuation by CDM in an Earth System Model. They demonstrate the

importance of accurately representing light attenuation by independently varying aquatic

constituents.

Primary Reader, Thesis advisor: Dr. Anand Gnanadesikan, Johns Hopkins University De-

partment of Earth and Planetary Sciences

Secondary Reader: Dr. Carlos Del Castillo, Goddard Space Flight Center, Ocean Ecology

Laboratory

Acknowledgments

Dedication

This thesis is dedicated to my grandmothers, Won Sook Park and Jea Sook Kim.

Contents

CONTENTS

List of Figures

List of Tables

Chapter 1

Introduction

The ocean's color is a consequence of the interaction of light with water and optically-active aquatic constituents. Systematic observations of ocean color exist from as early as the 1890s when a color scale for classifying natural waters was developed. The colors of the Forel-Ule scale (Forel, 1890; Ule, 1892) were derived from mixtures of standard chemical solutions to reproduce colors in the visible range, from 380nm-780nm. This scale was recently reconstructed and characterized with modern techniques to be used as a tool for deriving historic concentrations of the photosynthetic algal pigment, chlorophyll-a. An analysis of open ocean Forel-Ule observations from 1889-1999 found no overall global trend in derived chlorophyll concentrations, but found varying trends across ocean basins. Increasing chlorophyll concentrations were reported for the Atlantic Ocean and decreasing concentrations for the Indian and Pacific Oceans (Wernand et al., 2013).

Much more technologically advanced methods of characterizing and observing ocean color and observing global chlorophyll concentrations have been developed since the Forel-Ule scale. Since the successful launch of the first ocean color satellite sensor, the Coastal Zone Color Scanner (CZCS), in 1978, oceanographers have been equipped with daily, global estimates of chlorophyll concentration. Gregg and Rousseaux (2014) recently analyzed global satellite ocean color data from 1998 to 2012 to find no significant trend in global chlorophyll concentration. However, northern hemisphere ocean basins and the tropical Indian Ocean basin were found to have declining trends in chlorophyll concentration.

Why study trends in ocean color? Field et al. (1998) used CZCS data to estimate that photosynthetic carbon fixation by marine phytoplankton accounts for roughly half of the

global net annual primary production. Satellite-derived global distributions of chlorophyll

concentration provide a proxy for where the oceans are most productive, since phytoplank-

ton constitute the base of the marine food web. It is also relevant for biogeochemical

processes on longer timescales. Carbon dioxide emissions from fossil fuel burning and

land use changes between 1750-2014 are estimated to total 570 gigatons of carbon (GtC),

29% of which has been removed by the ocean (Le Quéré et al., 2015). The ocean takes up

carbon dioxide in two ways: (1) the dissolution of carbon dioxide into cold, sinking waters

at high latitude regions and (2) biological uptake of CO_2 by phytoplankton and conversion

into organic carbon. This organic carbon has the potential for long-term sequestration by

burial on the ocean floor via consumption by other marine organisms or physical transport

to the deep ocean. Monitoring ocean color is a powerful tool for observing the biological

state of the ocean and understanding its role in the carbon cycle and marine ecosystems.

Satellite ocean color data products extend beyond estimates of phytoplankton pigment

concentration. Algorithms have been developed to derive information about the upper

ocean optical properties, providing global-scale quantitative estimates of the interaction

of light with aquatic constituents. Light in water is attenuated by absorption and scattering.

These processes depend on the aquatic medium. When water or some other aquatic con-

stituent interacts with light, the radiation energy can be absorbed and converted to another

form of energy (e.g. mechanical, chemical) or the light can be scattered in many different

directions. The spectral absorption ($a(\lambda)$ $[m^{-1}]$) and scattering ($b(\lambda)$ $[m^{-1}]$) coefficients

are two inherent optical properties (IOPs) that represent the fraction of an incident beam of

45 light on a small volume of water that is absorbed and scattered over a given distance. The

46 sum of these two gives the spectral attenuation coefficient, $c(\lambda) = a(\lambda) + b(\lambda) \ [m^{-1}]$.

47   Furthermore, since IOPs are additive, they can be separated by the contribution of each

48 aquatic constituent. For example, for the total absorption coefficient of light, $a_{tot}[m^{-1}]$,

49 can be expressed as the sum of the absorption coefficients of the optically active aquatic

50 constituents:

$$a_{tot}(\lambda) = a_w(\lambda) + a_{phyt}(\lambda) + a_{CDOM}(\lambda) + a_{NAP}(\lambda), \quad (1.1)$$

51 where a_w is the spectrally dependent absorption coefficient of light by pure seawater,

52 a_{phyt} for phytoplankton, a_{CDOM} for chromophoric dissolved organic matter and a_{NAP}

53 for non-algal particles. These are all defined at some given wavelength, λ [nm]. Given

54 that the absorption spectrum for pure seawater is the same everywhere, spatial variations

55 in oceanic optical properties largely depend on the relative abundance of phytoplankton,

56 CDOM and non-algal particles (NAP). The light absorption coefficient for colored detrital

57 matter (CDM) is defined as the sum of the light absorption coefficient for CDOM and NAP;

58 i.e. $a_{dg} = a_{CDOM} + a_{NAP}$.

59   Radiance describes the spatial, temporal, directional and wavelength structure of the

60 light field. Measurements of light in the ocean are radiometric quantities, which can be

61 derived from the radiance function. For example, the spectral downwelling plane irradi-

62 ance is the radiance integrated over all azimuth and zenith angles pointing in the downward

direction. Although radiometric quantities can be used to describe the optical properties of a medium, they are not particularly useful for comparing two media because they are sensitive to changes in external environmental conditions. Instead, the light in aquatic environments is often characterized in terms of ratios or derivatives of radiometric quantities, which observations have shown to be relatively stable despite varying environmental conditions. These apparent optical properties (AOPs) depend on the properties of the aquatic medium and the directionality of the light field.

The vertical profile of light in the ocean is often approximated as an exponentially decaying function. The incident light at the surface of the ocean is a spectral downwelling plane irradiance at the surface, $I_d(0, \lambda)$ $[W\ m^{-2}]$, and diminishes with depth $z\ [m]$ as

$$I_d(z, \lambda) = I_d(0, \lambda)e^{\int_0^z k_d(z', \lambda)dz'}. \tag{1.2}$$

The reciprocal of $k_d(\lambda)$ $[m^{-1}]$, the diffuse attenuation coefficient for downwelling irradiance, is the e-folding depth for the incident light. The diffuse attenuation coefficient is an AOP, which varies with the inherent optical properties of an aquatic environment but is stable to variations in the external environment.

Morel (1988) developed a predictive model of the diffuse attenuation coefficient, $k_d(\lambda)$, for open ocean waters based on chlorophyll concentration. This was motivated by observations at the time which suggested that optical properties of the ocean are tightly subordinated to the abundance of pigmented algal cells. Similarly, Sathyendranath and Platt (1988)

developed a model for the diffuse attenuation coefficient that depended on the absorption
and scattering coefficients of aquatic constituents, whereby the absorption coefficient for
phytoplankton varied linearly as a function of chlorophyll concentration and the concentration of yellow substances varied proportionately to total absorption.

Repeat measurements of IOPs in ocean waters have since shown that the contribution by
CDOM, previously referred to as yellow substances (Kalle, 1938), accounts for a substantial proportion of the non-water light absorption in the open ocean. Furthermore, Bricaud
et al. (1981) showed that variations in spectral values of light absorption by CDOM from
various oceanic environments seem more influenced by land-based discharges than by marine biological activity. This finding has implications for the use of chlorophyll-based k_{d}
models that approximate the vertical profile of light where the optical properties are influenced by terrestrial and biological processes that vary independently of phytoplankton
growth. In the high latitude northern hemisphere and in coastal regions globally, the attenuation of light by terrestrially-derived CDOM and non-algal particles (NAP) are largely
influenced by freshwater fluxes. In the open ocean, CDOM production can depend on the
particular bacterial, algal and zooplankton assemblage in a given location, as all of those
organisms have been shown to produce CDOM.

Fully coupled Earth System Models (ESMs) are numerical simulations of the atmosphere and ocean circulations, including interactions with land and ice. ESMs have been
valuable tools for predicting future environmental change, most notably for their contributions to the synthesis efforts of the International Panel on Climate Change (IPCC). Several

102 of these IPCC-class ESMs utilize an ocean optical model that calculates k_{d} as a function of

103 chlorophyll concentration. In doing so, they are misrepresenting light attenuation for most

104 of the surface ocean.

105   This dissertation is concerned with the biogeochemical and hydrodynamic impacts

106 of de-coupling the light attenuation by chlorophyll concentration and other aquatic con-

107 stituents in a k_{d} model as implemented in the GFDL CM2Mc ESM (Galbraith et al., 2011),

108 a coarse resolution coupled climate model. The existing $k_{\mathrm{d}}(\lambda)$ parameterization is revised

109 to separate the contribution to light attenuation by chlorophyll concentration and colored

110 detrital matter (CDM), which is operationally defined as the sum of CDOM and NAP ab-

111 sorption coefficients. The spatial distribution of light attenuation by CDM is prescribed

112 according to a satellite data product $a_{\mathrm{dg}}(443)\ [m^{-1}]$, the light absorption coefficient for

113 CDM at 443nm.

114   Ocean color data products are derived from algorithms that relate in-situ measurements

115 of geophysical variables to remote sensing reflectance ($R_{rs}(\lambda)\ [sr^{-1}]$), an AOP:

$$R_{rs}(\theta, \phi, \lambda) = \frac{L_w(\theta, \phi, \lambda)}{E_d(\lambda)}. \tag{1.3}$$

116 where $L_w\ [W\ m^{-2}]$ is the water-leaving radiance through a solid angle $[sr^{-1}]$, centered

117 around a direction specified by its spherical coordinates (θ, ϕ), and $E_d\ [W\ m^{-2}]$ is the

118 downwelling plane irradiance which is the integral of all radiant energy in the downward

119 direction. These three measurements are all functions of wavelength ($\lambda[nm]$).

120   The ocean color satellite sensor detects radiance leaving the top of the atmosphere,

121   L_{TOA}, which is a radiometric quantity. This is converted to the AOP R_{rs}, by applying

122   an atmospheric correction to estimate the water-leaving radiance ($L_w(\lambda)$). This is then

123   divided by the mean extraterrestrial solar irradiance corrected for atmospheric attenuation

124   of the downwelling irradiance. Because R_{rs} is a ratio of radiometric quantities, it is less

125   sensitive to environmental conditions (e.g. sky conditions).

126   Two types of algorithms are primarily used for deriving ocean color satellite data prod-

127   ucts: empirical and semi-analytical. Empirical algorithms utilize best-fit functions that

128   relate in-situ measurements to $R_{rs}(\lambda)$. The first ocean color algorithms were empirical

129   algorithms, based on the observation that radiometric measurements over the ocean with

130   high chlorophyll concentrations were associated with a relative increase in reflectance in

131   the green wavelengths and a relative decrease in reflectance in the blue wavelengths (Clarke

132   et al., 1970).

133   Semi-analytical algorithms (SAAs), use linear and nonlinear least squares methods to

134   spectrally match satellite $R_{rs}(\lambda)$ with the spectral absorption ($a(\lambda)$) and scattering ($b(\lambda)$)

135   coefficients of water and aquatic constituents. Carder et al. (1991) developed a semi-

136   analytical algorithm to separate the absorption by colored detrital matter in coastal regions

137   and areas downstream from upwelling regions. Using the semi-analytical algorithm re-

138   duced the average error for chlorophyll-a retrievals from 61% to 23% in the California

139   Current upwelling region compared to the empirical algorithm. Siegel et al. (2005b) and

140   Siegel et al. (2005a) found large regions of the ocean where estimates from the empirical

algorithm exceeded those of the semi-analytical algorithm. These regions largely overlap

areas with greater light absorption by CDM. This suggests that empirical algorithms tend

to bias chlorophyll concentrations high because they are mistakenly assigning the optical

signal from CDM to chlorophyll. Furthermore, the authors suggest that the processes pro-

ducing CDM are fundamentally different from those related to phytoplankton growth and

therefore chlorophyll concentration in the upper ocean.

The bio-optical assumption states that ocean optical properties co-vary with chlorophyll

concentration. Applied to satellite remote sensing, this assumption is implicitly employed

in empirical algorithms for chlorophyll concentration. In other words, these algorithms rely

on the assumption that the remote sensing reflectance should change only as a function of

chlorophyll concentration. While this assumption may hold for large regions of the open

ocean, the processes controlling the production and decay of CDOM and NAP are likely

unrelated to phytoplankton abundance yet still contribute to the remote sensing reflectance.

Semi-analytical algorithms for chlorophyll concentration separate the optical contributions

of phytoplankton, CDOM, NAP. In doing so, it is less reliant on the bio-optical assumption

by quantifying the optical contribution to R_{rs} by other aquatic constituents.

The work in this dissertation investigates the consequences of disentangling the bio-

optical assumption in an Earth System Model by evaluating the role of light attenuation

by CDM as it varies independently of chlorophyll concentration. The experimental setup

for the following three studies is as follows. A parameterization for the diffuse attenuation

coefficient for downwelling irradiance in the blue-green wavelengths, $k_{\mathrm{d}}(bg)$ $[m^{-1}]$, was

162 developed to vary as a function of both chlorophyll concentration and light absorption by

163 CDM. The chlorophyll concentration is predicted by a biogeochemical model embedded

164 in the ESM. The light absorption by CDM is spatially prescribed using the ocean color

165 satellite data product for light absorption by CDM at 443nm, $a_{\mathrm{dg}}(443)$, which is derived

166 from a semi-analytical algorithm. The control model run calculates $k_{\mathrm{d}}(bg)$ as a function of

167 chlorophyll concentration only. The experimental model run calculates $k_{\mathrm{d}}(bg)$ as a function

168 of both chlorophyll concentration and $a_{\mathrm{dg}}(443)$. By taking the difference between these two

169 model outputs, we can quantify the role of light attenuation by CDM in the earth system.

170   Chapter 2 presents the $k_{\mathrm{d}}(bg)$ parameterization used in these studies, an empirical rela-

171 tionship between in situ measurements of $k_{\mathrm{d}}(\lambda)$, chlorophyll-a concentration and $a_{\mathrm{dg}}(443)$.

172 These in situ measurements show that there is no clear single relationship between $a_{\mathrm{dg}}(443)$

173 and chlorophyll-a concentrations as measured by high performance liquid chromatography

174 (HPLC). The bio-optical assumption does not hold for these data.

175   The satellite data product for $a_{\mathrm{dg}}(443)$ used in the model runs is also introduced in this

176 chapter. Ocean color sensors are passive sensors that simply observe the sunlight that is

177 scattered out of the water. Therefore, obstructions between the water and the sensor such

178 as clouds and ice prohibit data collection. Composite data products combine observations

179 over longer periods of time to maximize spatial coverage. For the purposes of these model

180 runs, we averaged annual composite MODIS Aqua data for $a_{\mathrm{dg}}(443)$ from 2002-2013 to

181 minimize extrapolated points in the dataset.

182   Comparing the results from these two model runs results in a shoaling of the attenua-

tion depth globally when CDM is included. Shrinking the euphotic zone increases modeled

chlorophyll concentrations and phytoplankton biomass near the surface but decreases pro-

ductivity at greater depths. The net integrated impact is a decrease in total biomass globally,

which reduces global nutrient uptake. This creates a situation where light is reduced but

nutrients are more abundant. The effect of these changes in light and nutrient limitation on

phytoplankton biomass are explored in various ocean biomes.

Chapters 3 and 4 are concerned with the role of changing light on hydrodynamic prop-

erties of the ocean. Chapter 3 addresses the role of optics on ocean circulation and ice

formation in the high latitude northern hemisphere. Differences in temperature tendency

between the two model runs are well represented by the combined changes in heating by

penetrating shortwave radiation, mixing and surface heat fluxes in the upper 100m. Short-

wave radiation is attenuated closer to the surface, which reduces heating below 10m during

summer months. Mixing entrains colder waters into the mixed layer during the autumn

and winter months. Increased cloudiness and ice thickness reduce incoming shortwave

radiation. The net effect of these changes in water column heating is colder SSTs in the

wintertime, resulting in greater ice formation. Chapter 4 investigates how including light

attenuation by CDM increases the range of sea surface temperatures (SSTs). Anomalous

penetrative shortwave heating in the upper 10m of the ocean is positively correlated with

anomalous SSTs in high latitude regions. Regions where including CDM results in more

extreme SSTs are mostly found in subpolar and temperature latitudes. Regional changes in

shortwave heating, surface heat fluxes and mixed layer depths are presented.

This dissertation concludes with a discussion of current advances in the field of charac-terizing CDOM, some challenges for including CDM in coupled biogeochemical-optical-hydrodynamic models and suggestions for future progress.

The work presented in this dissertation builds upon previous advances in utilizing satel-lite datasets to inform optical properties in simulations of the global oceans, which were not presented here. I refer the reader to the introductory material in the following chapters for references relating to the effects of changes in ocean light attenuation in Earth System Models. Previous discussions of hydrologic optics in this introduction can mostly be traced back to Kirk (1994) and Mobley (1994).   Other invaluable resources include the Ocean Optics Web Book (`http://www.oceanopticsbook.info/`) and lectures from the 2013 Ocean Optics Summer Course at the University of Maine Darling Marine Center.

Chapter 2

Quantifying the biological impact of surface ocean light attenuation by colored detrital matter in an ESM using a new optical parameterization

The work in this chapter has been published as a manuscript in the journal *Biogeosciences* (Kim et al., 2015) and is reproduced here.

CHAPTER 2. BIOLOGICAL IMPACT OF INCREASED LIGHT ATTENUATION BY
CDM IN AN ESM

Abstract

Light attenuation by colored detrital material (CDM) was included in a fully coupled Earth

system model (ESM). This study presents a modified parameterization for shortwave at-

tenuation, which is an empirical relationship between 244 concurrent measurements of the

diffuse attenuation coefficient for downwelling irradiance, chlorophyll concentration and

light absorption by CDM. Two ESM model runs using this parameterization were con-

ducted, with and without light absorption by CDM. The light absorption coefficient for

CDM was prescribed as the average of annual composite MODIS Aqua satellite data from

2002 to 2013. Comparing results from the two model runs shows that changes in light lim-

itation associated with the inclusion of CDM decoupled trends between surface biomass

and nutrients. Increases in surface biomass were expected to accompany greater nutrient

uptake and therefore diminish surface nutrients. Instead, surface chlorophyll, biomass and

nutrients increased together. These changes can be attributed to the different impact of

light limitation on surface productivity versus total productivity. Chlorophyll and biomass

increased near the surface but decreased at greater depths when CDM was included. The

net effect over the euphotic zone was less total biomass leading to higher nutrient con-

centrations. Similar results were found in a regional analysis of the oceans by biome,

investigating the spatial variability of response to changes in light limitation using a single

parameterization for the surface ocean. In coastal regions, surface chlorophyll increased by

35% while total integrated phytoplankton biomass diminished by 18%. The largest relative

increases in modeled surface chlorophyll and biomass in the open ocean were found in the

14

equatorial biomes, while the largest decreases in depth-integrated biomass and chlorophyll were found in the subpolar and polar biomes. This mismatch of surface and subsurface trends and their regional dependence was analyzed by comparing the competing factors of diminished light availability and increased nutrient availability on phytoplankton growth in the upper 200 m. Understanding changes in biological productivity requires both surface and depth-resolved information. Surface trends may be minimal or of the opposite sign than depth-integrated amounts, depending on the vertical structure of phytoplankton abundance.

2.1 INTRODUCTION

The attenuation of shortwave solar radiation in the surface ocean exerts a primary control on ocean biology since light is necessary for photosynthesis by phytoplankton. The decay of incident surface irradiance $I_{\mathrm{d}}(0,\lambda)$ with increasing depth z in the water column can be approximated as an exponential function:

$$I_{\mathrm{d}}(z,\lambda) = I_{\mathrm{d}}(0,\lambda)\exp\left(-\int_{0}^{z}k_{\mathrm{d}}(z',\lambda)\mathrm{d}z'\right),\tag{2.1}$$

where k_{d} (units of m^{-1}) is the spectral attenuation coefficient for downwelling irradiance. The reciprocal of k_{d} is the first e-folding depth of the incident light on the surface of the ocean, an intuitive length scale for the well-lit surface ocean. Variations in shortwave attenuation have been related to measured quantities of constituents in the aquatic medium,

such as concentrations of the phytoplankton pigment chlorophyll a. Morel (1988) observed increasing k_d with increasing chlorophyll a pigment concentrations in 176 concurrent in situ measurements, excluding stations where light attenuation was dominated by "yellow substance" or turbidity. These measurements were used to develop a function that relates k_d to chlorophyll a concentration of the form:

$$k_d(\lambda) = k_w(\lambda) + \chi(\lambda)[\text{chl}]^{e(\lambda)}, \tag{2.2}$$

where $k_w(\lambda)$ is the attenuation by pure seawater, [chl] is the chlorophyll a concentration and $\chi(\lambda)$ and $e(\lambda)$ are the wavelength-dependent coefficient and exponent. This parameterization implicitly includes the light attenuation of all other aquatic constituents presumed to be directly in proportion with chlorophyll concentration. Ohlmann and Siegel (2000) used a radiative transfer numerical model to develop an extended parameterization for k_d which depended on chlorophyll concentration, cloudiness and solar zenith angle to include the effects of varying physical conditions over ocean waters. Among these four variables, chlorophyll concentration was found to have the largest influence on reducing solar transmission below 1m.

These initial parameterizations have been adapted for use in ocean general circulation models (OGCMs) and Earth system models (ESMs) to study the influence of spatially varying light attenuation associated with varying concentrations of phytoplankton pigments in the ocean. Although numerous model experiments of this type have been conducted, we

mostly limit our introductory material to studies that utilized versions of the parameterization shown in Eq. (2.2). These studies examined the effects of applying a spatially varying k_d calculated from annual mean chlorophyll data, estimated by ocean color satellites, compared to the base case of a constant attenuation depth. Murtugudde et al. (2002) employed the Morel parameterization (Eq. 2.2) spectrally averaged over visible wavelengths, from 400 to 700nm, to calculate $k_\mathrm{d}(\mathrm{vis})$ using chlorophyll a concentration estimates from the Coastal Zone Color Scanner (CZCS). Spatially varying the attenuation depth improved the OGCM sea surface temperature (SST) simulation in the Pacific cold tongue and during ENSO events and in the Atlantic near river outflows. Subsequent studies employed an optics model that separately attenuated visible light in two bands of equal energy, nominally the "blue–green", $k_\mathrm{d}(\mathrm{bg})$, and "red" bands, $k_\mathrm{d}(r)$, as specified in Manizza et al. (2005):

$$k_\mathrm{d}(\mathrm{bg}) = 0.0232 + 0.074 \cdot [\mathrm{chl}]^{0.674}, \tag{2.3}$$

$$k_\mathrm{d}(r) = 0.225 + 0.037 \cdot [\mathrm{chl}]^{0.629}. \tag{2.4}$$

Studies that applied this k_d parameterization in ESMs were uniquely able to assess how changes in oceanic shortwave absorption can affect atmospheric and oceanic circulation via changes in SST. Gnanadesikan and Anderson (2009) observed changes in strength of the Hadley and Walker circulations when applying a spatially varying k_d using chlorophyll concentrations from the SeaWiFS (Sea-viewing Wide Field-of-view Sensor) ocean color satellite relative to a clear ocean with no chlorophyll. Alternatively, Manizza et al. (2005)

17

267 applied this parameterization to an OGCM with a biogeochemical model to calculate k_d

268 using modeled chlorophyll concentrations instead of surface chlorophyll estimates from

269 satellite. The main advantage of the latter model configuration is that phytoplankton can

270 respond to changes in environmental variables. They found that adding phytoplankton

271 amplified the seasonal cycles of SST, mixed layer depth and sea ice cover, which in turn

272 created environmental conditions that were favorable to additional phytoplankton growth.

273   Variations in light attenuation in ESMs were previously attributed to chlorophyll and

274 implicitly to aquatic constituents assumed to vary in proportion to chlorophyll. Other opti-

275 cally significant aquatic constituents can now be explicitly incorporated into models. This

276 paper is concerned with the omission of colored detrital material (CDM) in approximations

277 of light decay in the current generation of ESMs. CDM consists of chromophoric dissolved

278 organic matter (CDOM) and non-algal detrital particles (NAP). It is operationally defined

279 by its spectrally dependent absorption coefficient of light, a_dg (units of m^{-1}), which rep-

280 resents the fraction of incident power that is absorbed by detrital matter in a water sample

281 over a given pathlength. The absorption coefficient is given the subscript "dg" to repre-

282 sent the sum of the two component absorption coefficients; (1) non-algal detrital particles,

283 a_NAP, and (2) light-absorbing dissolved organic matter which passes through a 0.2–0.4 μm

284 filter, a_CDOM, (called "gelbstoff" by early researchers in optical oceanography, hence the

285 "g" in "dg"): $a_\mathrm{dg} = a_\mathrm{NAP} + a_\mathrm{CDOM}$. Measurements suggest CDOM accounts for a large

286 fraction of non-water absorption in the open ocean in the UV and blue wavelengths (Siegel

287 et al., 2005a; Nelson and Siegel, 2013). The attenuation of light by this strongly absorb-

ing component should be included in Earth system models. Although light absorption by NAP is a small fraction of CDM absorption (see Fig. 2.1), the sum of NAP and CDOM is considered because existing satellite algorithms cannot separate the contribution of each component.

Parameterizing k_d using Eq. (2.2) relies on the validity of the bio-optical assumption, which states that all light-attenuating constituents covary with chlorophyll concentration. However, processes that influence CDM abundance, such as freshwater delivery of terrestrial organic matter and photobleaching, can behave independently of chlorophyll a concentration, rendering the bio-optical assumption inappropriate for some aquatic environments. In an analysis of satellite ocean color data products, Siegel et al. (2005a) show correlation between chlorophyll and CDM distributions in subtropical gyres and upwelling regions. These variables are found to be independent in subarctic gyres, the Southern Ocean and coastal regions influenced by land processes such as coastal and river runoff. In this paper, we will consider the impact of decoupling the optical influence of chlorophyll a and CDM in Earth system models. Recent studies have incorporated the optical properties of additional in-water constituents into global ocean biogeochemical simulations. Gregg and Casey (2007) calculate in-water radiative properties using the absorption and scattering of water, phytoplankton groups and CDOM in a coupled ocean circulation-biogeochemical-radiative model. Dutkiewicz et al. (2015) assess the bio-optical feedbacks of detrital matter, CDOM and phytoplankton by explicitly representing these components in their ocean biogeochemistry–ecosystem model. In this paper we use a fully coupled Earth system
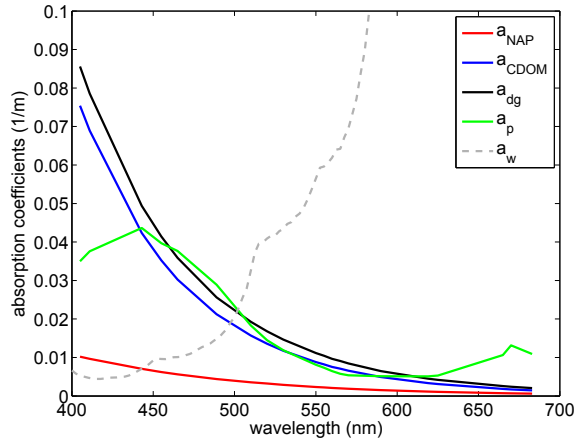
Figure 2.1: Median inherent optical property (IOP) spectra from NOMAD data set and absorption spectrum of pure water in gray. In the visible spectrum, CDOM absorption is strongest in the blue and decreases exponentially with increasing wavelength. The absorption spectrum of pure water is 0.0434 m^{-1} at 530nm and increases to 0.6m^{-1} at 700nm, exceeding the axis limits shown here (Pope and Fry, 1997). The absorption spectrum of particles (including phytoplankton), a_{p}, absorbs strongly in the red wavelengths compared to NAP and CDOM.

309 model to better understand how changes in light attenuation from including CDM affect

310 ocean ecosystems.

311   In Sect. 2, we introduce the global ocean color data set for the absorption coefficient

312 of detritus and CDOM, and discuss its incorporation into the Geophysical Fluid Dynamics

313 Laboratory (GFDL) Coupled Model 2 at Coarse resolution (CM2Mc) ESM with the Bio-

314 geochemistry with Light, Iron, Nutrients and Gases (BLING) model. This is accomplished

315 using a newly developed parameterization for $k_{\mathrm{d}}(\lambda)$, which aims to represent light attenu-

316 ation by chlorophyll a and CDM as independently varying phenomena. (For the remainder

317 of this paper, we will refer to chlorophyll a concentration simply as chlorophyll.) Section 3

318 details the model runs and the results, with a focus on how changes in light affect chloro-

319 phyll, biomass and nutrient concentrations. The paper concludes with Sect. 4, discussing

20

320 the implications of our findings and suggestions for future work.

2.2 METHODOLOGY

2.2.1 LIGHT PENETRATION PARAMETERIZATION

323 A new k_d parameterization was developed for implementation in the GFDL CM2Mc

324 ESM (Galbraith et al., 2011) with BLING ocean biogeochemistry (Galbraith et al., 2010).

325 In its current configuration, the CM2Mc–BLING system uses the Manizza et al. (2005)

326 optics model and k_d parameterization as shown in Eqs. (2.3) and (2.4). The new parame-

327 terization was developed from this optics model, revising the $k_d(bg)$ parameterization only

328 (Eq. 2.3). The $k_d(r)$ parameterization was unchanged because light absorption by CDOM

329 is very small compared to absorption by seawater and chlorophyll in the red wavelengths.

330 This is apparent upon examination of the spectral shapes of these constituents in Fig. 2.1.

331 The new $k_d(bg)$ parameterization incorporates the absorption coefficient of detritus and

332 CDOM at wavelength 443nm, $a_{dg}(443)$, because existing satellite data products of a_{dg} are

333 readily available for this wavelength only.

334 In the new parameterization, the dependence of $k_d(bg)$ on both chlorophyll concentra-

335 tion and $a_{dg}(443)$ is the best fit function between concurrent in situ measurements of these

336 variables from the NASA bio-Optical Marine Algorithm Dataset (NOMAD; Werdell and

337 Bailey, 2005). Measurements of k_d from 400 to 530nm were energy-weighted and averaged

338 to get a single value for the attenuation coefficient in the blue–green wavelengths. There

339 were 244 concurrent measurements of $k_d(bg)$, chlorophyll concentration and $a_{dg}(443)$ from

340 the NOMAD data set, representing both coastal and open ocean waters. The locations of

341 these measurements are shown in Fig. 2.2. The stations were arbitrarily grouped by re-

342 gion and color coded: (1) western Atlantic, northern cluster in black; (2) western Atlantic,

343 Amazon river outflow and offshore stations in green; (3) Antarctic peninsula in orange;

344 (4) Southern Ocean in blue; (5) western Pacific in magenta; (6) stations across the Pa-

345 cific Ocean in red and (7) eastern Pacific in cyan. We found poor correlation between

346 chlorophyll concentration and $a_{\mathrm{dg}}(443)$ at these stations, as shown in Fig. 2.3. The best fit

347 surface for $k_{\mathrm{d}}(\mathrm{bg})$, chlorophyll concentration and $a_{\mathrm{dg}}(443)$ was found using a least-squares

348 polynomial regression model using the Levenberg–Marquardt algorithm, resulting in the

349 following parameterization:

$$k_{\mathrm{d}}(\mathrm{bg}) = 0.0232 + 0.0513 \cdot [\mathrm{chl}]^{0.668} + 0.710 \cdot a_{\mathrm{dg}}(443)^{1.13}. \tag{2.5}$$

350 We conducted a sensitivity analysis to assess the importance of each region for obtaining

351 the parameters by removing one regional cluster from the regression fitting at a time. The

352 parameters were mostly stable. The exponent to the chlorophyll term was the only term

353 that changed by an amount that well exceeded the fitting uncertainty, increasing by 0.23

354 when the eastern Pacific stations were omitted. Figure 2.4a and b show an improved fit be-

355 tween modeled and measured $k_{\mathrm{d}}(\mathrm{bg})$ when using Eq. (3.4). Equation (3.4) is qualitatively

356 different from the previous parameterization, Eq. (2.3), in several ways. The attenuation

357 coefficient is less dependent on chlorophyll concentration, with a smaller coefficient and
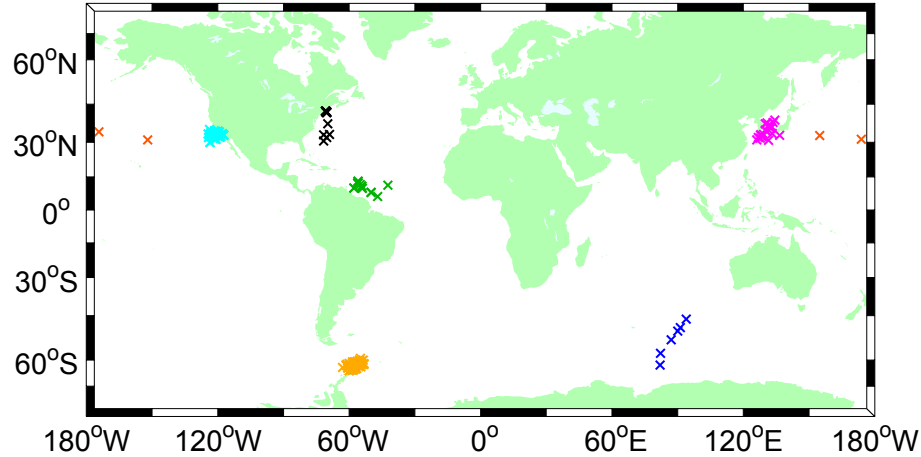
Figure 2.2: Map of stations with locations of the 244 in situ measurements used to develop
the k_d(bg) parameterization with CDM, Eq. (3.4), color coded by arbitrarily grouped by
region: (1) western Atlantic, northern cluster in black; (2) western Atlantic, Amazon river
outflow and offshore stations in green; (3) Antarctic peninsula in orange; (4) Southern
Ocean in blue; (5) western Pacific in magenta; (6) stations across the Pacific Ocean in red
and (7) eastern Pacific in cyan.

358 exponent on the chlorophyll term in Eq. (3.4) compared to Eq. (2.3). Additionally, the addi-

359 tional $a_{dg}(443)$ term makes the water more opaque in locations where CDM and chlorophyll

360 concentration are not well correlated, such as coastal zones that are strongly influenced by

361 the terrestrial delivery of CDOM. The k_d dependence on $a_{dg}(443)$ is superlinear, which at

362 first glance seems to suggest an unexpectedly strong dependence on CDOM and detrital

363 particles. We suggest this superlinear relationship is justified because the parameterization

364 is fitting for spatial variations in CDOM quality and quantity. Measurements of a_{dg} across

365 the ultraviolet to visible spectrum suggest the spectral dependence of light absorption by

366 CDOM is regionally specific (Nelson and Siegel, 2013).

2.2.2 IMPLEMENTATION IN ESM

This parameterization was implemented in the GFDL CM2Mc ESM, a coarse-resolution coupled global climate model with land, ice, atmosphere and ocean components (Galbraith et al., 2011). The Modular Ocean Model version 4p1 code is used to simulate the ocean. The model has a varying horizontal resolution from 1.01 to 3.39° and 28 vertical levels of increasing thickness with depth. Ocean biogeochemistry is represented by BLING, which is embedded in the ocean component of the physical model (Galbraith et al., 2010). The coupling between the biogeochemical model and physical model allows changes in chlorophyll concentration to produce changes in shortwave radiation absorption and vice versa. Since the same optical model is used for calculating light attenuation for physics and biology in our ESM configuration, the same attenuation depth is used in simulating physical processes and biological productivity. For example, the optical model calculates light attenuation using model-derived chlorophyll concentration. Increases in chlorophyll concentration reduce the attenuation depth, reducing total light available for biological processes such as photosynthesis and physical processes such as the total shortwave heating of the ocean. However, by utilizing one optical parameterization for the entire ocean, regionally specific variations of the functional dependence of light attenuation on chlorophyll and CDM are not represented in this model setup.

In the BLING biogeochemical model, the phytoplankton growth rate is calculated implicitly as a function of temperature, macronutrient concentration, iron concentration and
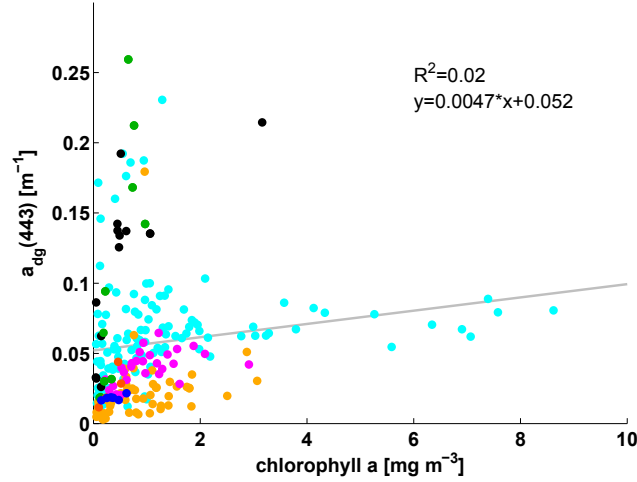
Figure 2.3: Scatterplot of 244 in situ chlorophyll a concentration and $a_{\mathrm{dg}}(443)$ concurrent measurements from the NOMAD data set used to develop the $k_{\mathrm{d}}(\mathrm{bg})$ parameterization with CDM, Eq. (3.4). Color coding corresponds to regional groupings from Fig. 2.2.

387   light.

$$\mu = P_0^{\mathrm{C}} \times \exp(kT) \times \mathrm{nlim} \times \mathrm{llim} \qquad (2.6)$$

388   where μ is a carbon-specific growth rate, P_0^{C} is a maximum growth rate at $0°$ C, $\exp(kT)$

389   is a temperature-dependent term based on Eppley (1972), $\mathrm{nlim} = \min\left(\mathrm{Fe_D}, \frac{\mathrm{PO_4}}{k_{\mathrm{PO_4}}+\mathrm{PO_4}}\right)$ is

390   a nutrient limitation term following a Liebig's law of the minimum and $\mathrm{llim} = \left(1 - \exp\left(\frac{-I}{I_k}\right)\right)$

391   is a light limitation term. These nutrient and light limitation factors, nlim and llim, repre-

392   sent the extent to which the optimal photosynthetic growth rate is scaled down by nutrient

393   and light availability. Mathematically, nlim and llim have values between 0 and 1 that scale

394   down the optimal photosynthetic rate as they are multiplied by P_0^{C}. Furthermore, these

395   are the only two variables that determine biomass in the BLING model. Total biomass is

396   a sum of large and small phytoplankton groups, which are related to growth rate μ by the

25

³⁹⁷ following equation

$$B = B_{\text{large}} + B_{\text{small}} = P^* \left(\left(\frac{\mu}{\lambda}\right)^3 + \left(\frac{\mu}{\lambda}\right) \right), \tag{2.7}$$

³⁹⁸ where B is biomass, P^* is a scale factor for phytoplankton concentration and λ is a temperature-

³⁹⁹ dependent mortality rate

$$\lambda = \lambda_0 \times \exp(kT). \tag{2.8}$$

⁴⁰⁰ Substituting Eqs. (2.6) and (2.8) for μ and λ into Eq. (2.7) gives us

$$B = P^* \left(\left(\frac{P_0^{\text{C}} \times \exp(kT) \times \text{nlim} \times \text{llim}}{\lambda_0 \times \exp(kT)} \right)^3 + \left(\frac{P_0^{\text{C}} \times \exp(kT) \times \text{nlim} \times \text{llim}}{\lambda_0 \times \exp(kT)} \right) \right).$$

⁴⁰¹ Following Dunne et al. (2005), the temperature dependence of the mortality rate is set

⁴⁰² identical to that of the growth rate such that the $\exp(kT)$ term in both μ and λ expressions

⁴⁰³ are identical, Eq. (2.9) reduces to the following relationship between biomass, nutrient

⁴⁰⁴ limitation and light limitation

$$B \propto (C(\text{nlim} \times \text{llim})^3 + (\text{nlim} \times \text{llim})), \tag{2.9}$$

⁴⁰⁵ where C is a constant. Dunne et al. (2005) found that such a formulation was able to

⁴⁰⁶ reproduce the observed phytoplankton size structure across 40 sites. This allows us to

⁴⁰⁷ separately evaluate the contributions of nutrient and light limitation to changes in biomass

⁴⁰⁸ in our biogeochemical model. This relationship will be utilized in the results section of our

₄₀₉ paper.

₄₁₀   Chlorophyll concentration is calculated from biomass using a varying chl : C ratio to

₄₁₁ account for photoadaptation. Large-scale patterns and features of chlorophyll concentra-

₄₁₂ tion are qualitatively represented, with lower chlorophyll concentration in the gyres and

₄₁₃ higher concentrations in northern mid- to high latitudes and equatorial upwelling zones

₄₁₄ (see Fig. 2.5). In general, the modeled annual average chlorophyll exceeds the satellite

₄₁₅ observed chlorophyll concentration in the open ocean. The seasonal cycle is also well-

₄₁₆ represented, but with a northern latitude spring bloom onset earlier than appears in satellite

₄₁₇ data. There is good spatial agreement between the modeled and observed spatial distri-

₄₁₈ bution of macronutrients, which is shown in Fig. 2.6. BLING models only phosphate

₄₁₉ concentration, which is comparable to an "average macronutrient" that represents the aver-

₄₂₀ age concentrations of phosphate and nitrate scaled to phosphate by the N : P Redfield ratio,

₄₂₁ $\frac{1}{2}(\text{PO}_4 + \frac{\text{NO}_3}{16}$; Galbraith et al., 2010). The error in chlorophyll and nutrient concentrations

₄₂₂ in this implementation of BLING are worse than in Galbraith et al. (2010) because the

₄₂₃ model parameters were originally tuned to a data-driven ocean model. As a result, errors

₄₂₄ that appear in the physical circulation will also appear in the biological solution.

₄₂₅   The ocean optical model receives incoming shortwave radiation from the atmospheric

₄₂₆ component. Visible light is divided and then averaged into two spectral bands, blue–green

₄₂₇ and red, which are then attenuated by $k_\text{d}(\text{bg})$ and $k_\text{d}(r)$ respectively. In its previous con-

₄₂₈ figuration, BLING calculated $k_\text{d}(\text{bg})$ as a function of chlorophyll concentration as shown

₄₂₉ in Eq. (2.3). For this study, $k_\text{d}(\text{bg})$ is calculated using Eq. (3.4) with model-predicted
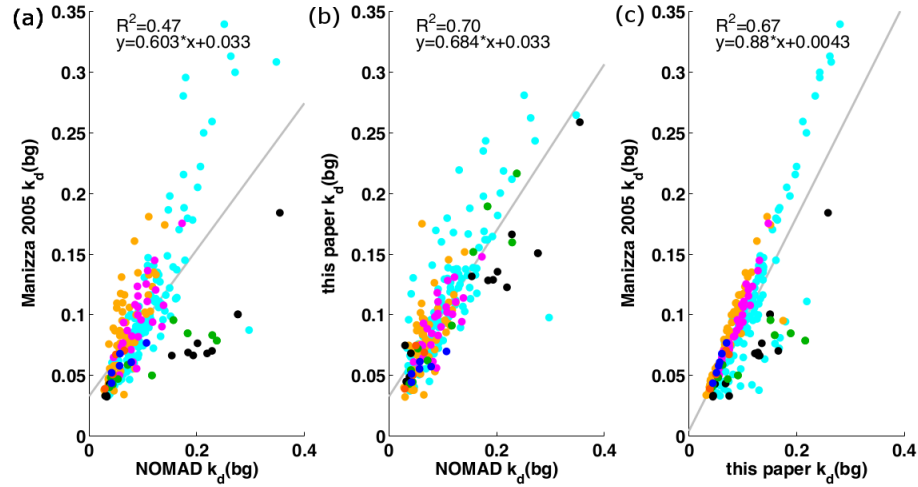
Figure 2.4: **(a)** and **(b)** Scatterplots comparing observed $k_{\mathrm{d}}(\mathrm{bg})$ from the NOMAD data set and modeled $k_{\mathrm{d}}(\mathrm{bg})$ using two different parameterizations, Eqs. (2.3) and (3.4). The modeled $k_{\mathrm{d}}(\mathrm{bg})$ values are calculated from in situ chlorophyll a and $a_{\mathrm{dg}}(443)$ measurements corresponding to the observed $k_{\mathrm{d}}(\mathrm{bg})$ values on the x axis. **(c)** Comparison of Eqs. (2.3) and (3.4) applied to NOMAD in situ chlorophyll concentrations and $a_{\mathrm{dg}}(443)$ measurements to calculate $k_{\mathrm{d}}(\mathrm{bg})$. The 0.88 slope on the regression line indicates that when CDM is included, $k_{\mathrm{d}}(\mathrm{bg})$ increases more rapidly than when it depends on chlorophyll concentration alone. Color coding corresponds to regional groupings from Fig. 2.2.

430 chlorophyll concentration and fixed $a_{\mathrm{dg}}(443)$ from satellite climatology. The $a_{\mathrm{dg}}(443)$

431 data set used in this study is the average of the 2002 to 2013 Aqua MODIS Garver–

432 Siegel–Maritorena (GSM; Maritorena et al., 2002) $a_{\mathrm{dg}}(443)$ Level 3 annual composites

433 from `http://oceancolor.gsfc.nasa.gov`. Annual average data were used in-

434 stead of monthly data to maximize the number of grid cells with unimpeded satellite ob-

435 servations. Consequently the seasonal variability of CDM is not represented in our model

436 runs. By fixing $a_{\mathrm{dg}}(443)$ as a constant value throughout the year, light absorption by CDM

437 is underestimated in months where riverine and coastal runoff deliver additional CDOM to

438 the ocean. The averaged satellite data were re-gridded to the ocean model's spatial reso-

439 lution and missing values were filled in by equal weight averaging over the pixel's eight

Figure 2.5: Comparison of **(b, d)** chlorophyll concentration in mg m^{-3} from SeaW-iFS satellite observation (Yoder and Kennelly, 2003) used in earlier similar studies and **(a, c)** modeled using GFDL ESM CM2Mc with BLING biogeochemistry. Data shown are from the chl&CDM model run described in Sect. 4 of this paper. Annual average surface distributions are shown in **(a, b)** and monthly average surface concentrations by latitude are shown in **(c, d)**.

440   neighbors using Ferret, a data visualization and analysis tool for gridded data sets (see

441   Fig. 2.7). Satellite-estimated values of surface $a_{\mathrm{dg}}(443)$ were held constant with increasing

442   depth.

2.3   MODEL RUNS: SETUP, RESULTS AND DISCUSSION

2.3.1   MODEL SETUP

The GFDL CM2Mc ESM with BLING ocean biogeochemistry was spun up for 1500

years with the Manizza et al. (2005) ocean optics model, allowing dynamical processes

to reach equilibrium. New model runs were initialized from this spun-up state and were

completed for an additional 300 years. We analyzed the final 100 years of the model runs

to average over interannual variability and to eliminate the influence from spin-up, which

we consider to be the period of time it takes for a distinct signal to develop. For the model

experiments discussed in this paper the spin-up time was less than 50 years. The data

presented in this section are average results from the final 100 years of the two model

runs: the (1) "chl&CDM" run utilizes the full $k_{\mathrm{d}}(\mathrm{bg})$ parameterization, Eq. (3.4), while

the (2) "chl-only" run calculates light attenuation with the chlorophyll-dependent term

only: $k_{\mathrm{d}}(\mathrm{bg}) = 0.0232 + 0.0513 \cdot [\mathrm{chl}]^{0.668}$. The difference between the two model runs

(chl&CDM minus chl-only) shows the impact of added shortwave attenuation by CDM.

For the remainder of this paper we will refer to $k_{\mathrm{d}}(\mathrm{bg})$ as k_{d} for simplicity.

The SST contour plot in Fig. 2.8a shows modeled (chl&CDM) minus observed us-

ing NOAA_OI_SST_V2 data provided by the NOAA/OAR/ESRL PSD, Boulder, Colorado,

USA, from their web site at `http://www.esrl.noaa.gov/psd/` (Reynolds et al.,

2002). The RMS error between annually averaged modeled and observed SST is 1.5°C.

Additional validation details for the physical ocean model can be found in Galbraith et al.
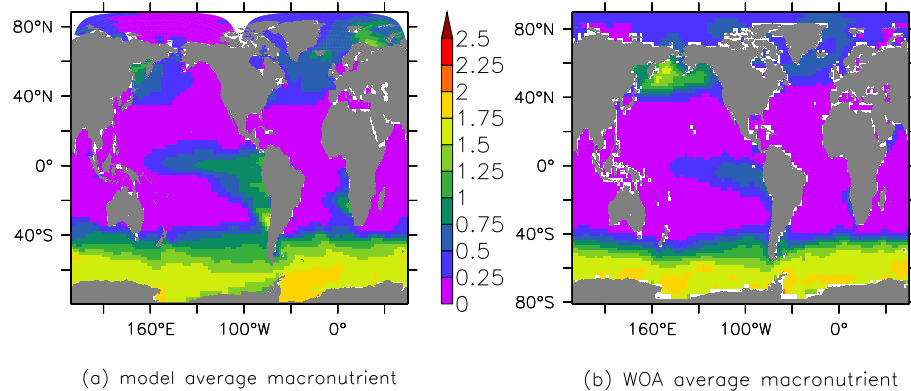
(a) model average macronutrient   (b) WOA average macronutrient

Figure 2.6: Comparison of macronutrient concentrations $\frac{1}{2}\left(PO_4 + \frac{NO_3}{16}\right)$, **(a)** modeled using GFDL CM2Mc with BLING biogeochemistry and **(b)** observed annual mean field, from World Ocean Atlas 2013 nitrate and phosphate data sets (Garcia et al., 2014). Concentration in μ M.

463 (2011). The chl-only model run minus observed is not shown because the differences

464 are qualitatively similar to those shown in Fig. 2.8a. The differences in SST between the

465 chl&CDM and chl-only model runs (in Fig. 2.8b) are generally small in the annual mean

466 and do not cause a significant change in the RMS error.

467 2.3.2 MODEL RESULTS: GLOBAL TRENDS

468   Adding CDM to the k_d parameterization shoaled the attenuation depth (k_d^{-1}, in m) in

469 most places. This change in the light field was accompanied by a globally integrated 10%

470 increase in surface macronutrients, 11% increase in surface biomass and 16% increase

471 in surface chlorophyll. These changes reflect the total value from the surface grid boxes,

472 which represent the uppermost 10m. At first glance, this result was puzzling since increases

473 in chlorophyll and biomass are generally associated with increased nutrient consumption,

474 which is usually indicated by decreased nutrient concentration. Instead, all three variables
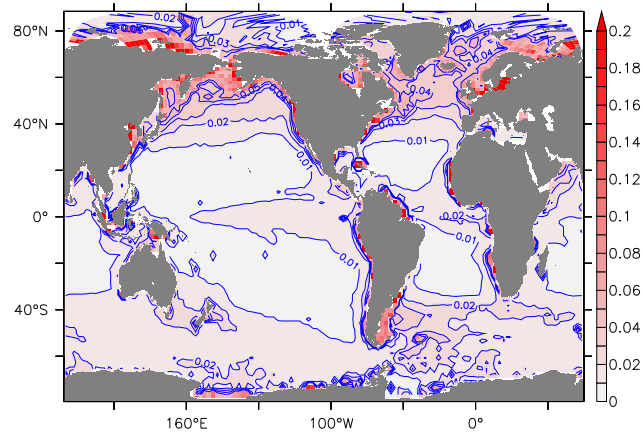
31

Figure 2.7: The spatial distribution of $a_{\mathrm{dg}}(443)$ as prescribed in the model runs for this paper, mapped onto the CM2Mc ESM tracer grid with data extrapolated into polar regions.

increased together. The spatial distributions of surface changes in macronutrients, chlorophyll concentration and biomass are shown in Fig. 2.9.

In order to understand these surface changes, it is necessary to evaluate changes in the biomass depth profile. Globally averaged biomass and particulate organic carbon (POC) export flux in the chl&CDM run are higher near the surface but diminished at depth, as shown in Fig. 2.10. Chlorophyll increases at the surface, but below 25m there is less biological productivity in the chl&CDM run. The depth-integrated result is a 9% decrease in total biomass. Furthermore, since biological productivity is occurring closer to the surface, particulate matter is remineralized in the water column and less is exported into the deep ocean. This can be seen in Fig. 2.10b. The cumulative effect is a 7% decrease in POC flux at 200m.

This upward shift in the vertical distribution of biomass was accompanied by increased macronutrients at all depths. Here, we will consider the distribution of macronutrients in

the top 200m as a measure of the biological activity in the mixed layer according to the bio-logical pump efficiency, E_{bp}, defined in Sarmiento and Gruber (2006) as $E_{bp} = \frac{C_{deep} - C_{surface}}{C_{deep}}$. This metric provides a indication of the extent to which phytoplankton are able to draw down nutrients delivered to the surface from the deep ocean. Here, $C_{surface}$ is the integrated nutrient concentration between 0 and 100m and C_{deep} is the integrated nutrient concentration between 100 and 200m. The difference in E_{bp} between the two model runs shows a widespread decrease in biological pump efficiency when CDM is included (see Fig. 2.11). In a global average sense, increased light limitation by CDM diminishes total biomass, leaving excess nutrients in the water column. Nutrients are more abundant and phytoplankton are less effective at utilizing them when the ocean is more light limited. The spatial correlation between the difference in E_{bp} and a_{dg} is -0.26, indicating a general negative relationship between the two variables. However, regions of greatest light absorption by CDM are not always the same regions of greatest decrease in E_{bp} for reasons that will be discussed in the following subsections.

2.3.3   OCEAN BIOMES

The analysis in this section will address changes in nutrient concentration and bio-logical productivity by ocean biome. Following Sarmiento et al. (2004), we use average vertical velocity, maximum wintertime mixed layer depth and sea ice cover to define six biomes that are differentiated based on physical circulation features. They are (1) equatorially influenced, between 5° S and 5° N, divided into upwelling and downwelling regions,

33
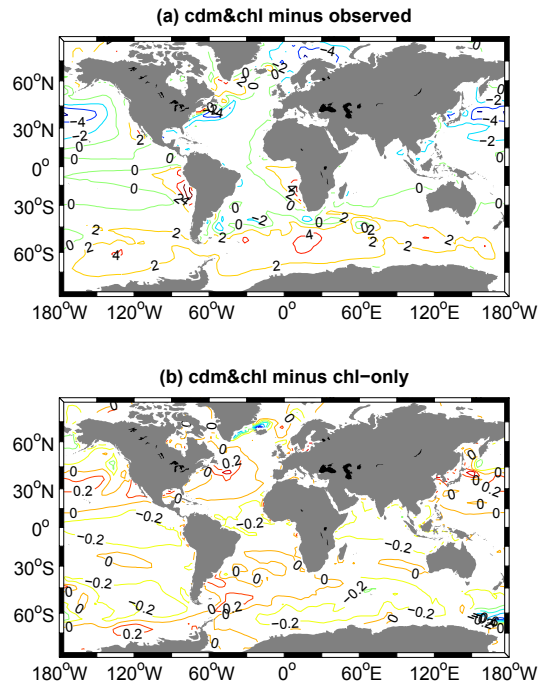
Figure 2.8: Difference in annual average SST in °C for **(a)** chl&CDM minus observed
using the NOAA_OI_SST_V2 data set (Reynolds et al., 2002) and **(b)** chl&CDM minus
chl-only.

508 (2) marginal sea ice zones that are covered by sea ice at least once during the year, (3)

509 permanently stratified subtropical biomes where downwelling occurs and maximum mixed

510 layer depth is ≤150m, (4) seasonally stratified subtropical biomes where downwelling oc-

511 curs and maximum mixed layer depth >150m, (5) low-latitude upwelling regions between

512 35° S and 30° N, and (6) all subpolar upwelling regions north of 30° N and south of 25° S.

513 Boundaries were determined based on circulation features from the respective model runs

514 for consistency. See Fig. 2.12 for a visual representation of biome extent for the chl&CDM

515 model run.

516   The largest changes in biome areal extent include a 19% increase in the Northern Hemi-

517 sphere marginal ice zone and −9% change in the extent of the neighboring subpolar North-

(a) attenuation depth   (b) macronutrient

(c) ln(chl&CDM/chl−only)   (d) biomass
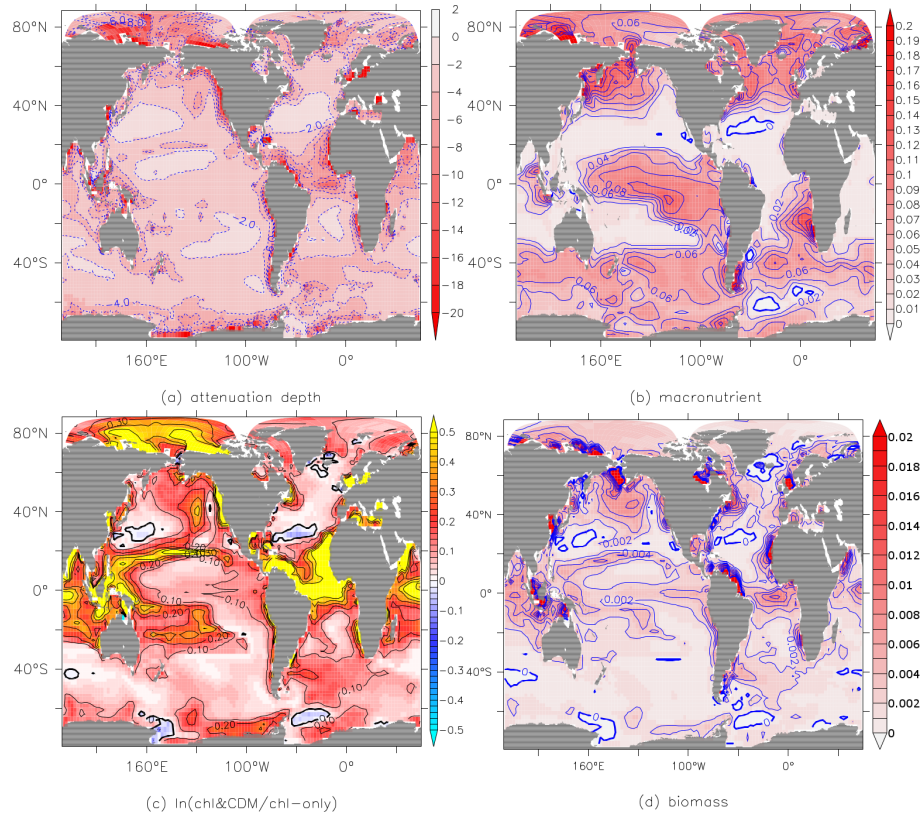
Figure 2.9: Difference **(a)** attenuation depth in m, **(b)** surface macronutrient concentration in μ M, **(c)** surface chlorophyll concentration and **(d)** surface biomass concentration in $g\,C\,m^{-3}$; chl&CDM minus chl-only. Surface values represent the average over the top 10m. Panel **(c)** shows natural log ratio of chlorophyll concentration from the chl&CDM run over chl-only run, so positive values indicate an increase in chlorophyll in the chl&CDM run.

518   ern Hemisphere biome, as shown in Table 2.1. The biome area changes between the two

519   model runs because the biological and physical models are coupled. The added light at-

520   tenuation by CDM in the optical model affects both biological production and physical

521   variables such as SST in our ESM configuration. Furthermore, the changes in chlorophyll

522   concentration from the increased light attenuation change the attenuation depth in the phys-

523   ical model.

(a) Biomass

(b) Carbon Export Flux

Figure 2.10: Globally averaged profile of **(a)** biomass in $g\,C\,m^{-3}$ and **(b)** carbon export flux in $g\,C\,m^{-2}\,yr^{-1}$. Black line shows data from the chl-only run, red line represents chl&CDM run.

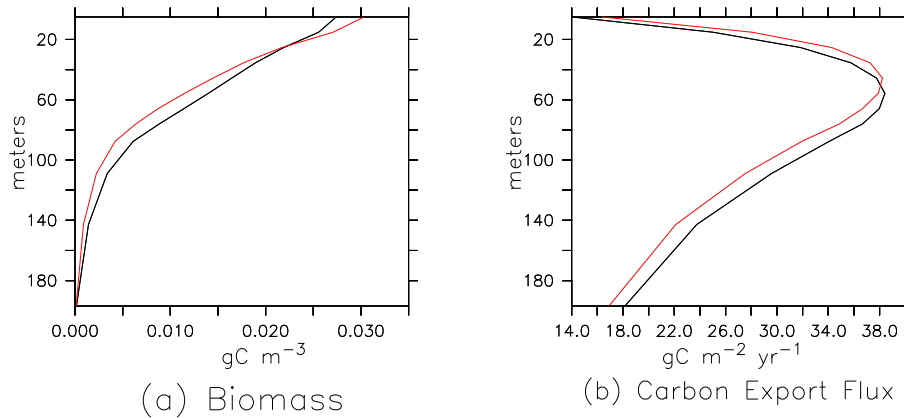Differences in surface chlorophyll, biomass and macronutrients between the two model runs (see Table 2.2) show that the addition of CDM results in several important qualitative and regionally specific changes. For example, the greatest relative change in chlorophyll and biomass over the upper 10m are found in equatorial and low-latitude biomes, with 15–17% increases in biomass and 21–24% increases in chlorophyll. Additionally, the greatest changes in depth-integrated chlorophyll and biomass are found in high-latitude regions. In the Northern Hemisphere subpolar biome, chlorophyll decreased by 14% and biomass decreased by 15%. Chlorophyll and biomass decreased by 9 and 10% respectively in the Southern Hemisphere marginal ice zone. The following analysis seeks to understand this mismatch between surface and subsurface trends between biomes. In particular, why are the largest changes in surface chlorophyll near the equator and largest changes in depth-integrated chlorophyll at higher latitudes?

As shown in previous sections, phytoplankton increase at the surface and decrease be-

36

Table 2.1: Surface area by biome, in km^2 with percentage change in area between the two model runs (chl&CDM minus chl-only).

Biome	chl&CDM	% age of total	chl-only	% age of total	% change
Equatorial Upwell	1.86×10^7	6%	1.86×10^7	6%	0%
Equatorial Downwell	8.34×10^6	3%	8.07×10^6	3%	3%
Low Latitude Upwell	6.32×10^7	21%	6.32×10^7	21%	0%
Permanently Stratified	1.01×10^8	34%	9.89×10^7	33%	2%
Seasonally Stratified	3.93×10^7	13%	4.11×10^7	14%	-4%
Subpolar NH	1.22×10^7	4%	1.35×10^7	4%	-9%
Ice NH	1.17×10^7	4%	9.81×10^6	3%	19%
Subpolar SH	2.33×10^7	8%	2.43×10^7	8%	-4%
Ice SH	2.37×10^7	8%	2.27×10^7	8%	4%

537 low when CDM is included. The resulting vertical profile of chlorophyll is altered in differ-

538 ent ways depending on the biome. To illustrate, we choose three representative biomes from

539 various latitudes, for which chlorophyll profiles are shown in Fig. 2.13. In the equatorial

540 upwelling and seasonally stratified biomes, the deep chlorophyll maximum is increased.

541 In the ice NH region, where light delivery is seasonally dependent, chlorophyll is found in

542 highest concentrations near the surface and is diminished at depth. In every biome, there is

543 more chlorophyll near the surface but less chlorophyll beyond some depth. These changes

544 can be attributed to a combination of diminished light availability and increased nutrient

545 availability.

546 Over the upper 200m, there are more nutrients and less irradiance at all depths. Re-

547 ferring back to Fig. 2.10a, there is more biomass near the surface, but diminished biomass

548 at depth. These plots show that as we move down the water column, there is a changing

549 balance of nutrient and light availability affecting phytoplankton growth. The increased

550 abundance of nutrients fuels the growth of phytoplankton near the surface. At depth, light
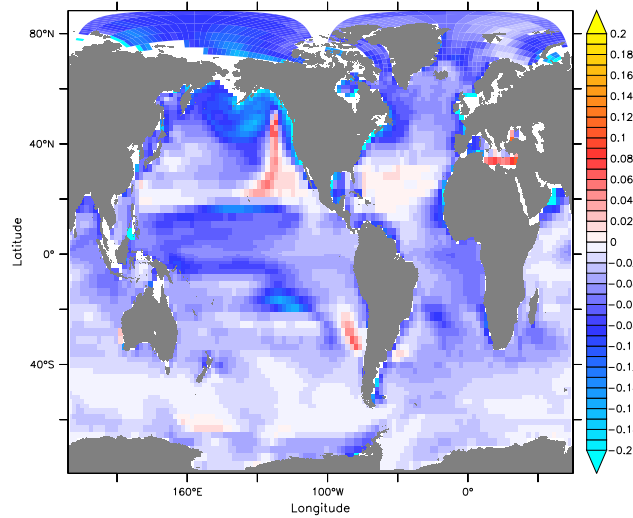
Figure 2.11: Difference in E_{bp}, chl&CDM model run minus chl-only model run.

limitation is increased to a level that results in diminished phytoplankton productivity.

We analyze the competition of light and nutrient availability on biomass using the light
and nutrient limitation factors previously discussed in the Methodology section. The aver-
age light and nutrient limitation scaling factors over the surface 10m of each open ocean
biome and the coastal region for the chl-only run are shown in Fig. 2.14a. The coastal
region was defined as grid cells adjacent to land. Consider the placement of the vari-
ous biomes on this plot for the model run where light attenuation depends on chlorophyll
alone. The equatorial regions are least light limited, so they lie to the right on the x axis.
The marginal ice zones and subpolar regions are most light limited and lie to the left on the
x axis. The Southern Hemisphere biomes are in general more nutrient limited than their
Northern Hemisphere counterparts, due to modeled iron limitation. They are found lower
on the y axis.

As additional light limitation is introduced by the inclusion of light absorption by CDM
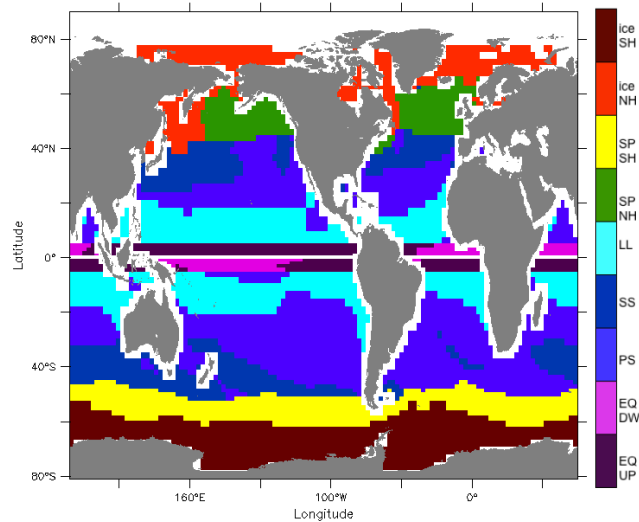
Figure 2.12: Biomes as defined by Sarmiento et al. (2004) applied to GFDL CM2Mc with chl&CDM k_{d} parameterization, Eq. (3.4). Legend abbreviations: ice is marginal ice zone, SP is subpolar, LL is lower latitude, SS is seasonally stratified, PS is permanently stratified, EQ DW is equatorial downwelling, EQ UP is equatorial upwelling. Suffixes NH and SH stand for Northern Hemisphere and Southern Hemisphere.

in the k_{d} parameterization, these markers shift. Fig. 2.14b shows nlim and llim averaged

over the surface 10m for the chl&CDM model run. The displacement of each point from

panel a to its new coordinates in panel b are shown in vector form in panel c. The vector

begins at its coordinates from panel a, i.e., values from the chl-only run, and terminates

with an "x" at the new coordinates from the chl&CDM model run. This vector indicates

the change in nutrient and light limitation between the two model experiments.

The impact of these changes in light and nutrients on biomass can be seen by overlaying

lines of constant biomass onto these plots. Using Eq. (2.9), we utilize the fact that in the

BLING model, biomass scales as $(C(\mathrm{nlim} \times \mathrm{llim})^3 + (\mathrm{nlim} \times \mathrm{llim}))$. In panel c, all biome

vectors point in the left and upward direction, indicating more nutrient availability and

less light availability. The vectors cross contours of constant biomass in the direction of

Table 2.2: Difference in surface chlorophyll $mg\,m^{-3}$, biomass $mg\,C\,m^{-3}$ and macronutrient μM concentrations, chl&CDM minus chl-only. Surface values are the average over the top 10m. All surface changes are statistically significant to three standard deviations. Statistical significance tests were performed on decadally smoothed data from the final 100 years of the two model runs.

Biome	Δ chl	% Δ	Δ biomass	% Δ	Δ nutrient	% Δ
Equatorial Upwell	0.28	22%	4.5	16%	0.053	14%
Equatorial Downwell	0.23	24%	4.2	17%	0.052	24%
Low Latitude Upwell	0.21	21%	3.1	15%	0.038	20%
Permanently Stratified	0.18	15%	2.0	10%	0.036	13%
Seasonally Stratified	0.52	7%	2.2	5%	0.066	15%
Subpolar NH	0.83	9%	4.2	7%	0.071	19%
Ice NH	0.90	18%	7.7	14%	0.10	23%
Subpolar SH	0.29	7%	0.97	3%	0.041	3%
Ice SH	0.18	11%	1.3	6%	0.038	2%

increasing biomass. Additional nutrient availability fuels increases in biomass in the upper

10m of the ocean in almost every ocean biome, which is in agreement with the results

reported in Table 2.2. Panel d is similar to panel c, but with nlim, llim values averaged

over the upper 200m of the ocean. Here, the vectors are moving in a direction that crosses

lines of decreasing biomass. This is consistent with results shown in Table 2.3. In this

case, the decrease in light availability drives the decrease in biomass, despite the increase

in nutrients.

The two clusters of vectors, i.e., nlim and llim averaged over (1) 0 to 10m constituting

a "euphotic regime" and (2) 0 to 200m constituting a "subsurface regime", are shown on

the same plot for comparison in Fig. 2.15. To first order, we think of the euphotic regime as

the depth range that dominates the signal seen by satellite observations and the subsurface

regime as the integrated impact over the entire ecosystem. The key difference between the
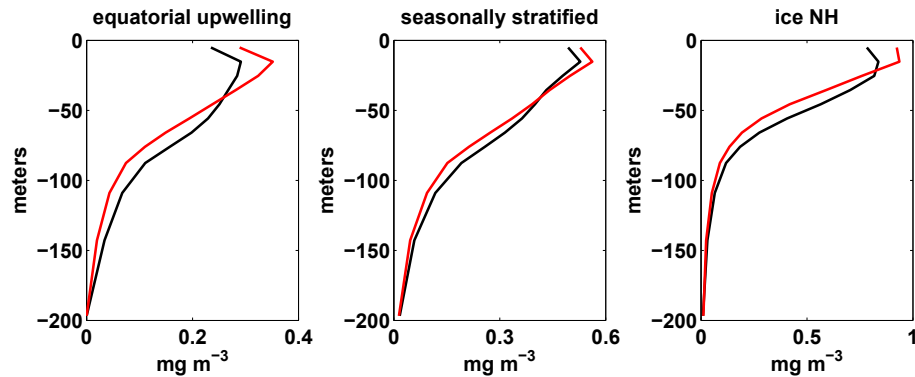
Figure 2.13: The depth profile of chlorophyll concentration $mg\,m^{-3}$ in three biomes. The black line indicates the chl-only run, red line represents chl&CDM run. The equatorial upwelling and seasonally stratified biomes show increased peaks in the deep chlorophyll maximum (DCM) when CDM is included. All three biomes show increased chlorophyll near the surface, but diminished chlorophyll at depth.

587 two regimes is the vectors in the surface regime are crossing lines of constant biomass in

588 the increasing biomass direction, while the vectors in the subsurface regime are crossing

589 lines of constant biomass in the decreasing biomass direction. While there is a noticeable

590 difference in the magnitude and angle of the vectors between these two regimes, these

591 differences are only meaningful in the context of the vector's placement in the domain. For

592 example, the greatest decreases in depth-integrated biomass from the inclusion of CDM

593 were found in high-latitude biomes and coastal region. This is most pronounced in the

594 coastal region, where biomass diminished by 18%. The corresponding magenta vector

595 in this plot noticeably spans the greatest distance in the direction of decreasing biomass

596 contour lines. Although the vector for the Northern Hemisphere marginal ice zone (ice

597 nh) is smaller, it is placed in the upper left hand corner where the contour lines are closer

598 together. It crosses the appropriate number of lines of constant biomass to produce the

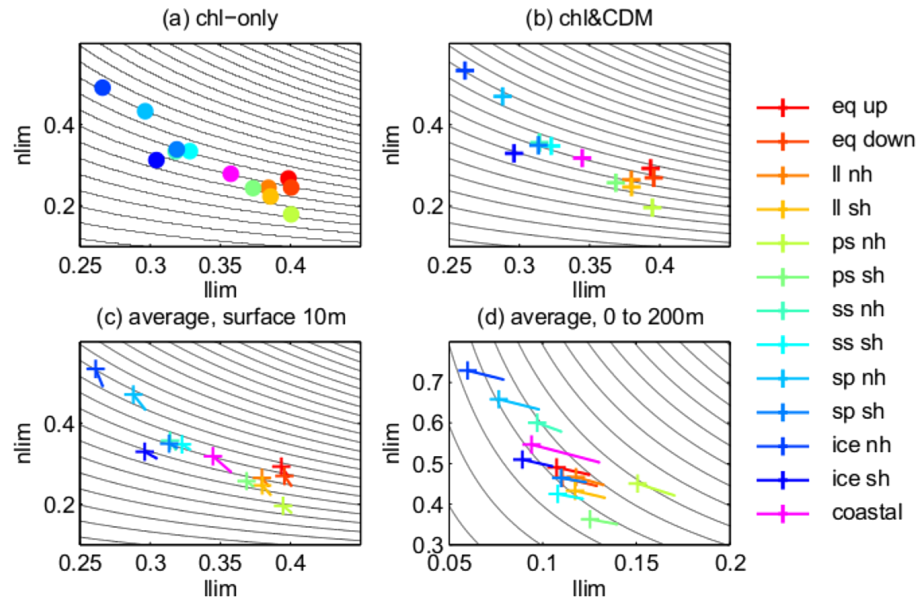599 10% drop in biomass in this region when CDM is included. In the surface regime, the

Figure 2.14: Light and nutrient limitation scaling factors for open ocean biomes and coastal regions. **(a)** Average nlim, llim for chl-only model run, from 0 to 10m **(b)** average nlim, llim for chl&CDM model run, from 0 to 10m **(c)** vectors connecting coordinates from panels **(a, b)**, average from 0 to 10m. **(d)** Vectors starting at coordinates from chl-only model run and terminating with an "x" at values from chl&CDM model run, average from 0 to 200m. Legend abbreviations: ice is marginal ice zone, sp is subpolar, ss is seasonally stratified, ps is permanently stratified, ll is lower latitude, eq up is equatorial upwelling, eq down is equatorial downwelling, coastal is coastal regions, defined as the grid cells adjacent to land. Suffixes nh and sh stand for Northern Hemisphere and Southern Hemisphere.

600 greatest increases in biomass are in the equatorial biomes. While the "eq up" and "eq

601 down" vectors are short, shown in Fig. 2.14c, the slope of the vector results in sufficient

602 positive displacement in the y direction to produce increasing biomass. The slope of some

603 of the higher latitude vectors, such as the seasonal stratified biomes are more parallel to the

604 lines of constant biomass, which accounts for the smaller changes in surface biomass.

605   Increases in surface chlorophyll ranged from 15 to 24% in the equatorial, low-latitude

606 and permanently stratified biomes. In these areas, depth-integrated biomass decreased by

607 $\leq 6\%$. These biomes comprise the cluster of vectors on the bottom right hand side of the
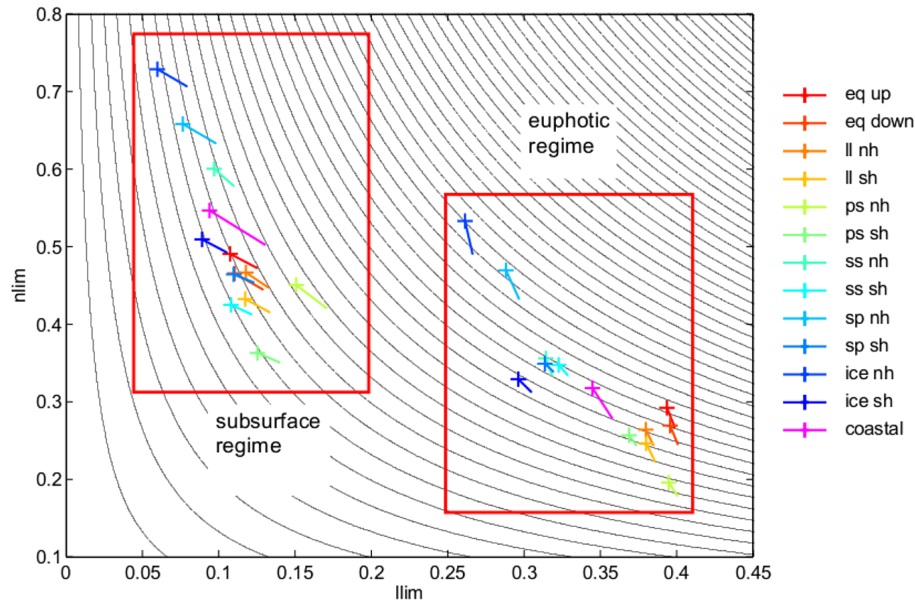
Figure 2.15: All vectors from Fig. 2.14c and d, on the same plot. Vectors for nlim, llim values averaged over the upper 10m occupy the "euphotic regime" and values averaged over the upper 200m occupy the "subsurface regime".

plot in Fig. 2.15. The variation in surface chlorophyll appears to depend on the seasonal availability of light, since the biomes are similarly nutrient limited. In these biomes, shoaling the euphotic zone concentrates phytoplankton closer to the surface. In equatorial and low-latitude regions, the steady supply of light and upwelling currents keep phytoplankton near the surface mostly year-round. Here, surface chlorophyll increased by 21–24%. In the permanently stratified biome, there are intermittent mixing events and, on average, downwelling currents. Mixing the phytoplankton throughout the water column has the effect of reducing the concentration of phytoplankton near the surface. Any increases in surface chlorophyll in the stratified regions will be intermittent and when annually averaged smaller than the changes found near the equator, which explains why surface chlorophyll increased by 15% in the permanently stratified biome.

Table 2.3: Difference in chlorophyll $mg\,m^{-2}$, biomass $mg\,C\,m^{-2}$ and macronutrients $mmol\,m^{-2}$ between the two model runs (chl&CDM minus chl-only), integrated over the upper 200m.

Biome	Δ chl	% Δ	Δ biomass	% Δ	Δ nutrient	% Δ
Equatorial Upwell	-1.7	-7%	-87	-6%	15	8%
Equatorial Downwell	-1.2	-5%	-67	-5%	17	11%
Low Latitude Upwell	-0.74	-4%	-38	-3%	13	9%
Permanently Stratified	-0.77	-4%	-61	-4%	11	11%
Seasonally Stratified	-2.2	-5%	-127	-5%	16	13%
Subpolar NH	-8.8	-14%	-482	-15%	15	11%
Ice NH	-2.2	-5%	-179	-8%	22	16%
Subpolar SH	-1.6	-5%	-139	-6%	7.4	2%
Ice SH	-2.1	-9%	-165	-10%	5.3	1%

2.3.4 COASTAL REGIONS AND MODEL ERROR

The spatial distribution of light absorption by CDM in Fig. 2.7 and diminished attenuation depth in Fig. 2.9 suggest the addition of CDM to the optical model would have a significant impact on ocean productivity in coastal regions. For the following analysis, the coastal region was defined as grid cells adjacent to land.

In coastal regions, surface nutrients increased by 16%, surface biomass by 22% and surface chlorophyll by 35%. Depth-integrated trends were of the opposite sign compared to surface trends. Total biomass decreased by 18% and total chlorophyll decreased by 17% when CDM was included. The largest percentage change in integrated biomass was found in the equatorial latitudes, where there was up to a 38% drop in coastal biomass. High northern latitudes north of 60°N experienced decreases of 17–36% in coastal biomass. These results are reported with the understanding that the coastal circulation is likely to be poorly resolved in our coarse model. Nonetheless, they highlight the potential impact of
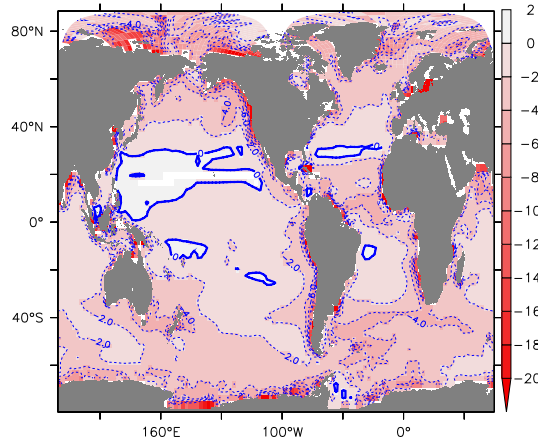
Figure 2.16: Difference in attenuation depth in m; chl&CDM minus model run using Eq. (2.3).

including the optical impact of CDM in coastal regions.

The results shown in this paper compare the chl&CDM and chl-only model runs. A comparison of the output of the chl&CDM model run and a model run with the original k_d parameterization, Eq. (2.3), show qualitatively similar trends in coastal regions. Surface nutrients increased by 1%, surface biomass by 3% and surface chlorophyll by 6%, while depth-integrated biomass and chlorophyll decreased by 9% (chl&CDM minus model run using Eq. 2.3). It will be important for models to include the optical impact of CDM to avoid the potential error of misrepresenting light attenuation as models with finer grid resolution are developed, especially in coastal regions.

A similar comparison of the model runs using the chl&CDM and the original k_d parameterization, Eq. (2.3), for the entire ocean shows small changes in globally averaged surface and total nutrients, biomass and chlorophyll. Surface nutrients decreased by 3%, surface biomass decreased by 2% and surface chlorophyll decreased by 3%. Total biomass

645 increased by 1% and total chlorophyll increased by less than 1% when CDM was included.

646 The differences in attenuation depth between chl&CDM and the original k_d parameteriza-

647 tion are between 0 and 2m for large areas of the ocean, as shown in Fig. 2.16. As mentioned

648 in the Methodology section, the chlorophyll term has a smaller coefficient and exponent in

649 Eq. (3.4) compared to Eq. (2.3). Separating the optical contribution of chlorophyll and

650 CDM into two terms gave less weight to the chlorophyll term. In some regions with little

651 attenuation by CDM, there was decreased surface attenuation in the model run that included

652 CDM due to the decreased attenuation by the chlorophyll term. As a result, there are more

653 areas where the difference in attenuation is equal to or greater than 0, which can be seen in

654 a comparison of Fig. 2.16 and Fig. 2.9a. The attenuation depth increased by an average of

655 0.9m in locations where the difference in attenuation depth was positive. Based on these

656 results, we find that the biological model error from explicitly excluding the optical impact

657 of CDM by using Eq. (2.3) to be small for the open ocean. The biological implication for

658 ESMs using Eq. (2.3) is most profound for coastal regions, as described in the previous

659 paragraph.

660 2.4 CONCLUSIONS

661 This paper addressed the impact of colored detrital matter on biological production

662 by altering the attenuation of the in-water light field in the GFDL CM2Mc Earth system

663 model with BLING biogeochemistry. Light absorption by detrital matter and CDOM, a_{dg},

664 was prescribed using a satellite data set with near-complete global surface ocean coverage.

The results show that increasing light limitation can decouple surface trends in modeled biomass and macronutrients. Although increased biomass is usually associated with high productivity and decreased nutrients, this was not the case in our light-limited model runs. Surface chlorophyll, biomass and nutrients all increased together. These changes can be attributed to increased biological productivity in the upper water column and a decrease below, which increased surface chlorophyll and biomass while simultaneously decreasing depth-integrated biomass. The diminished total biomass left excess nutrients in the water column that were eventually delivered to the surface, elevating surface macronutrient concentrations. While absolute changes in chlorophyll and macronutrient concentrations were small, one key implication of this model experiment is that surface biomass trends may not reflect how light limitation is reducing ecosystem productivity. Understanding changes in ecosystem productivity requires both surface and depth-resolved information.

Adding the optical impact of CDM decreased integrated coastal biomass and chlorophyll concentrations by 18%. Additionally, surface chlorophyll concentrations in coastal regions increased by 35%. The open ocean biome analysis showed how, in the BLING model, changes in surface chlorophyll and biomass over the upper 200m in various biomes depend on a combination of light and nutrient availability. In the high latitudes, adding CDM to the light-only limited Northern Hemisphere vs. the iron–light co-limited Southern Hemisphere seemed to have different impacts on biomass decline. In the low to mid-latitudes, the impact of circulation on light availability for phytoplankton determined the structure of the chlorophyll profile and the response of that biome to a shrinking euphotic

686 zone. These results highlight the biomes that may be most vulnerable to changes in biomass

687 and chlorophyll if met with changes in light availability. For example high-latitude biomes

688 that were already light limited experienced the greatest drop in biomass from additional

689 light limitation.

690 In this study, the k_{d} parameterization was developed with measurements from several

691 major regions of the global oceans but did not comprehensively represent the entire ocean's

692 optical properties. The model results showed the greatest changes in biomass in the North-

693 ern Hemisphere polar and subpolar regions, but our parameterization did not include in situ

694 data from these regions. The spatial distribution of a_{dg} was fixed, so it could not respond to

695 changes in the light field as chlorophyll concentration is able to do in the CM2Mc–BLING

696 coupled physical–biogeochemical model configuration. The a_{dg} values were constant with

697 time so the seasonal cycle was not represented. An analysis of satellite monthly climatol-

698 ogy data shows there is more variability near river mouths and equatorial upwelling zones

699 (not shown), indicating these areas would be most affected by including annual cycles.

700 Furthermore, surface values were held constant throughout the water column.

701 Resolving these simplifications may have important impacts. An interactive CDOM

702 tracer would be best suited for such a task, once the mechanisms that control the production

703 and degradation of CDM are better understood. Previous work has elucidated some poten-

704 tial sources and sinks of CDOM to the ocean, including in situ production by heterotrophic

705 microbial activity (Nelson et al., 2004), delivery by freshwater input from terrestrial sources

706 and degradation by photobleaching when exposed to intense light conditions (Blough and

Vecchio, 2002). Recently, Nelson et al. (2010) showed the depth-resolved cross sections of a_{CDOM} through the major ocean basins approximately follow apparent oxygen utilization contours. This suggests that oxygen might be used to improve modeling depth-dependent CDOM distributions in the future. Dutkiewicz et al. (2015) demonstrate a method for modeling an interactive CDOM tracer as a fraction of dissolved organic material production. Similar to the work presented in our paper, Dutkiewicz et al. (2015) compared model runs with and without the optical impact of CDOM and detrital matter. They found greater productivity and nutrient utilization at higher latitudes when CDOM and detrital matter were omitted, resulting in less nutrient delivery and consequently less biomass in lower latitudes. Their more sophisticated biogeochemical model was also able to evaluate changes in the prevalence of phytoplankton types associated with changes in the in-water light spectrum from including and removing CDOM and detrital matter. This particular method does not include the key process of terrestrial CDOM delivery. Modeling land sources of CDOM would be of particular importance to regions where CDOM abundance is in flux due to changes in the volume and composition freshwater runoff. In the Arctic Ocean, CDOM is of primary importance in determining the non-water absorption coefficient of light and its relatively concentrated presence increases energy absorbed in the mixed layer by trapping incoming shortwave radiation (Pegau, 2002). Hill (2008) used a radiative transfer model to find the absorption of shortwave radiation by CDOM can increase energy absorbed by the mixed layer by 40% over pure seawater and this additional energy accounts for 48% of springtime ice melt by water column heating. These impacts should be incorporated into

728 future Earth system models and existing higher-resolution regional models to more accu-

729 rately simulate the ocean heat budget and marine biogeochemistry.

730

731 **Acknowledgements**

Chapter 3

Increased surface ocean heating by colored detrital matter (CDM) linked to greater Northern Hemisphere ice formation in the GFDL CM2Mc ESM

Abstract

Recent observations of Arctic Ocean optical properties have found that colored dissolved organic matter (CDOM) is of primary importance in determining the non-water absorption coefficient of light in this region. Although CDOM is an important optical constituent in the Arctic Ocean, it is not included in most of the current generation of Earth System Models (ESMs). In this study, model runs were conducted with and without light attenuation by colored detrital matter (CDM), the combined optical contribution of CDOM and non-algal particles, in the fully-coupled GFDL CM2Mc ESM to examine the differences in heating and ice formation in the high northern latitudes. The annual cycle of sea surface temperature (SST) is amplified in the model run where the optical attenuation by CDM is included. Annually-averaged integrated ice mass is 5% greater and total ice extent is 6% greater due to colder wintertime SSTs. Differences in ocean heating (i.e. temperature tendency) between the two model runs are well represented by the combined changes in heating by penetrating shortwave radiation, mixing and surface heat fluxes in the upper 100m. Shortwave radiation is attenuated closer to the surface, which reduces heating below 10m during summer months. Mixing entrains colder waters into the mixed layer during the autumn and winter months. Increased cloudiness and ice thickness in the model run with CDM reduces incoming shortwave radiation.

3.1 INTRODUCTION

Decreasing snow cover, melting glaciers, increasing precipitation and increasing river discharge have been observed in the Arctic in the last century (Serreze et al., 2000; Peterson et al., 2002). It is expected that as temperatures continue to rise, river input to the Arctic Ocean will continue to increase. Rivers are a major source of chromophoric dissolved organic matter (CDOM), the optically significant component of the dissolved organic material pool, to the oceans (Blough and Vecchio, 2002). The potential for increasing CDOM abundance accompanying increasing river discharge has motivated optical oceanographers to characterize the optical properties of the Arctic Ocean in recent decades (Mitchell, 1992; Pegau, 2002; Matsuoka et al., 2007; Hill, 2008).

The optical properties of a water body can be characterized in terms of its inherent optical properties (IOPs). The spectral absorption coefficient of light, $a(\lambda)$ [m^{-1}], is an IOP that represents the fraction of an incident beam of light on a small volume of water that is absorbed over a given distance. As IOPs are additive, the total spectral absorption coefficient of light (a_{tot}) for an oceanic water sample can be separated into the absorption coefficient by each aquatic constituent such that:

$$a_{tot}(\lambda) = a_w(\lambda) + a_{phyt}(\lambda) + a_{CDOM}(\lambda) + a_{NAP}(\lambda), \tag{3.1}$$

where a_w is the spectrally dependent absorption coefficient of light by pure seawater, a_{phyt} for phytoplankton, a_{CDOM} for chromophoric dissolved organic matter and a_{NAP} for non-

algal particles. The absorption coefficient for colored detrital matter (CDM), a_{dg}, is the sum of the last two terms, a_{CDOM} and a_{NAP}. Given that the absorption spectrum for pure seawater is the same everywhere, spatial variations in oceanic optical properties largely depend on the relative abundance of phytoplankton, CDOM and non-algal particles (NAP).

Observations of Arctic Ocean optical properties have shown that CDOM is of primary importance in determining the non-water absorption coefficient of light. Pegau (2002) and Matsuoka et al. (2007) found that the diffuse attenuation coefficient and non-water absorption coefficient was largely determined by light absorption by CDOM in the Chukchi and Beaufort Seas. Although CDOM is an important optical constituent in the Arctic Ocean, it is not included in most of the current generation of Earth System Models (ESMs).

Previous studies including the optical contribution of key aquatic constituents in coupled climate models have mostly examined the impact of including solar attenuation by chlorophyll, the light-harvesting pigment in phytoplankton. Patara et al. (2012) and Wetzel et al. (2006) found Arctic sea ice generally decreased when chlorophyll was included in a fully coupled ocean-atmosphere-biogeochemistry model. The presence of phytoplankton in the upper ocean increased solar radiative heating and sea surface temperatures (SSTs) compared to the control run with fixed attenuation depth. In another study, including chlorophyll decreased ice thickness year-round but wintertime SSTs and ice extent were the same (Lengaigne et al., 2009). These results seem to suggest that including the optical attenuation by an additional optical constituent may warm Arctic Ocean SSTs and further decrease ice extent in a fully coupled climate model. However, including phytoplankton

increased wintertime Arctic sea ice extent by 2% (Manizza et al., 2005) in a global ocean general circulation model with forced atmosphere. In a study of the North Atlantic Ocean, including phytoplankton in a coupled ecosystem-circulation model resulted in net oceanic heat loss and small changes in SST (Oschlies, 2004). Given the lack of agreement in the literature, further investigation is warranted.

One possible reason for the discrepancy between studies is that the inclusion of chlorophyll in ESMs has been shown to change the strength and location of oceanic and atmospheric circulation patterns outside the Arctic Ocean (Gnanadesikan and Anderson, 2009; Patara et al., 2012). It is unclear whether changes in heating and sea ice previously reported for the Arctic Ocean originated from changes in heating within the Arctic Ocean, or were transported from lower latitudes via global-scale atmospheric and ocean circulation. Anderson et al. (2007) found that adding chlorophyll-dependent absorption to an ocean with only absorption by pure seawater induced annual-mean patterns of temperature change with cooling in the equatorial Pacific and warming in the Atlantic, with similarities to La Nina or a negative phase of the PDO. Both of these climate modes are thought to affect sea ice thickness and concentration in the Arctic Ocean (Lindsay and Zhang, 2005; Liu et al., 2004).

In this study, we examine the impact of additional light attenuation by CDM on short-wave heating and ice formation in the high northern latitudes. The spatial distribution of light absorption by CDM is prescribed using a satellite data product, which by definition includes the light absorption by CDOM and NAP. In our model setup, the GFDL CM2Mc

ESM (Galbraith et al., 2011) includes a coupled ocean-atmosphere system with BLING ocean biogeochemical model (Galbraith et al., 2010). Section 2 further details the ESM model setup and the optical parameterization used to include light attenuation by aquatic constituents.

In section 3, we compare the results from a model run with light attenuation by both chlorophyll and CDM to a model run where light attenuation depends on chlorophyll concentration only. One key difference between our study and those mentioned earlier is that both our model runs include the optical attenuation by chlorophyll predicted by a biogeochemical model. Most previous studies have compared model runs with a fixed attenuation depth to attenuation that depends on chlorophyll concentration. Our study allows changes in light attenuation to feed back onto chlorophyll concentrations in ways generally not captured in previous work. The results in this study highlight changes in ocean hydrodynamics and relevant connections to the ice and atmosphere components. We conclude with a discussion of our results in the context of modeling efforts in this field in section 4.

3.2 METHODS: MODEL DESCRIPTION AND SETUP

The GFDL CM2Mc ESM is a fully-coupled global climate model with land, ice, atmosphere and ocean components (Galbraith et al., 2011). In this section, we highlight key components of the ocean, ice and biogeochemical models that are relevant to this study. The Modular Ocean Model version 4p1 (MOM4p1) code is used to simulate ocean dynamics. We refer the reader to Griffies et al. (2005) for a complete description of the model

842 advection and diffusion schemes. The model has varying latitudinal resolution from 2/3°

843 near the equator to 3° in the mid-latitudes and 3° meridional resolution. Over the Arctic a

844 tripolar grid with a nominal resolution of 3° is used. There are 28 vertical levels of increas-

845 ing thickness with depth in the ocean. Ocean biogeochemistry is evaluated according to the

846 BLING model (Galbraith et al., 2010) and is fully coupled with the hydrodynamic model.

847　　　Heating in the vertical direction is determined by vertical diffusion, non-local mixing,

848 and shortwave penetration. Vertical diffusion acts to redistribute heat through a transport

849 that flows down (and is proportional to) the local gradient of temperature. The column sum

850 of in-water heating by vertical diffusion approximately equals the sum of modeled surface

851 and bottom fluxes:

$$\sum_{z=0}^{bottom} \rho c_p \left(\frac{\partial T}{\partial t} \right)_{vdiff} \approx \text{Surface Heat Fluxes} + \text{Geothermal Heating}. \qquad (3.2)$$

852 The constants ρ [kg m^{-3}] and c_p [J kg^{-1} °C^{-1}] designate the density and heat capacity

853 of seawater. Major modeled ocean surface heat fluxes include shortwave radiation, long-

854 wave radiation, sensible and latent heating and cooling. Non-local mixing parameterizes

855 the effect of eddies which span the mixed layer, stirring up dense water from the pycno-

856 cline and transporting heat downwards (Troen and Mahrt (1986) as implemented by Large

857 et al. (1994)). In regions where there is a net heat flux to or from the ocean, the resulting

858 imbalance can either be supplied by horizontal mixing or by the advection of heat.

859　　　In-water shortwave heating is calculated from the penetrating solar radiation at each

depth. An ocean optical model embedded in the biogeochemical model controls upper

ocean shortwave attenuation. The biogeochemical model is coupled to the hydrodynamic

model, which allows changes in chlorophyll concentration to produce changes in shortwave

radiation absorption and vice versa. This feature incorporates the bio-optical feedback of

chlorophyll on light attenuation, which is important for the realistic representation of the

annual cycle of sea ice in the Arctic Ocean (Lengaigne et al., 2009). However, our model

does not include phytoplankton within the ice sheet, as in the ice-algal ecosystem model of

Jin et al. (2012).

The decay of incident spectral irradiance $I_d(0, \lambda)$ [W m^{-2}] with increasing depth z [m]

in the ocean is approximated and modeled according to an exponential function:

$$I_d(z, \lambda) = I_d(0, \lambda) \, exp[-\int_0^z k_d(z', \lambda)dz'], \qquad (3.3)$$

where k_d [m^{-1}] is the attenuation coefficient for downwelling irradiance and λ [m] indi-

cates the wavelength dependence of the incident irradiance, downwelling irradiance and

attenuation coefficient. The attenuation depth is the reciprocal of k_d, i.e. the first e-folding

depth of the incident light on the surface of the ocean. Incident visible light at each depth

is divided and averaged into two spectral bands, blue-green and red, which are attenuated

by k_d(bg) and k_d(r) respectively.

The attenuation coefficient varies as a function of aquatic constituents in the model. As

presented in Kim et al. (2015), this relationship was derived from a best-fit analysis of 244

878 concurrent in situ bio-optical measurements of k_d(bg), chlorophyll concentration and light

879 absorption by CDM:

$$k_d(bg) = 0.0232 + 0.0513 \cdot chl^{0.668} + 0.710 \cdot a_{dg}(443)^{1.13}, \qquad (3.4)$$

880

881 where chl is the BLING model-predicted chlorophyll concentration and $a_{dg}(443)$ is a satellite-

882 estimated light absorption coefficient for colored detrital material (CDM) at 443nm. The

883 constant 0.0232 is the band-averaged attenuation coefficient for pure seawater. The spec-

884 tral absorption coefficient for CDM, a_{dg} [m^{-1}], is operationally defined as the sum of the

885 absorption coefficients for (1) non-algal particles (NAP), a_{NAP}, and (2) light-absorbing dis-

886 solved organic matter which passes through a 0.2–0.4 μm filter, a_{CDOM} (i.e. $a_{dg} = a_{NAP} +$

887 a_{CDOM}). The satellite dataset used to prescribe $a_{dg}(443)$ is the average of the 2002 to 2013

888 Aqua MODIS GSM $a_{dg}(443)$ Level 3 annual composites from http://oceancolor.gsfc.nasa.gov.

889 These values are fixed throughout the year and do not vary seasonally. The data was

890 re-gridded to the ocean model's spatial resolution and missing values were filled in by

891 equal weight averaging over the pixel's 8 neighbors. The satellite dataset used to prescribe

892 $a_{dg}(443)$ in this study is shown in Fig. 3.1a. For simplicity, we will refer to k_d(bg) as k_d

893 for the remainder of this paper. We do not change the attenuation coefficient for red wave-

894 lengths, k_d(r), in this study because CDOM absorption is small compared to absorption by

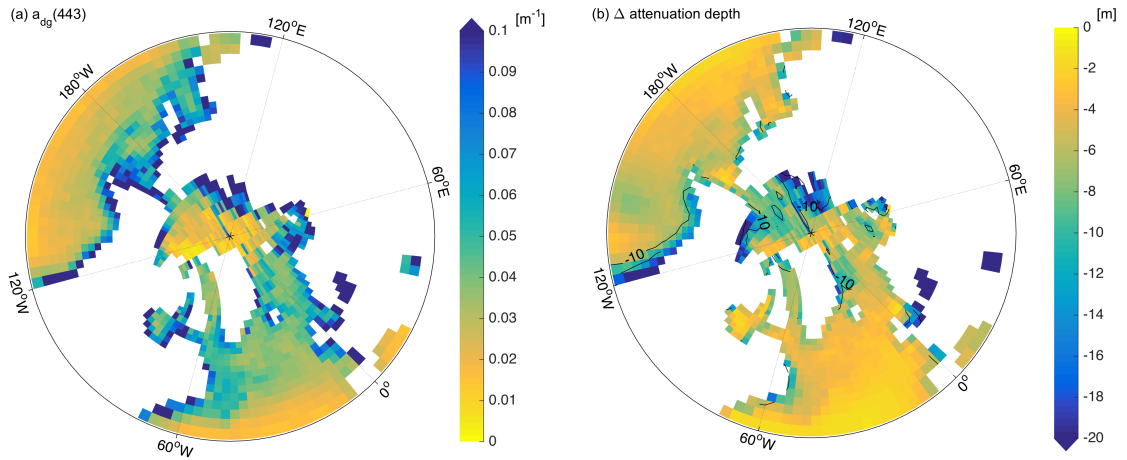895 seawater and chlorophyll for these wavelengths.

59

Figure 3.1: (a) The prescribed spatial distribution of the absorption coefficient of light for colored detrital matter, $a_{\mathrm{dg}}(443)$ [m^{-1}], for the model runs in this study on the CM2Mc ESM tracer grid. (b) Change in attenuation depth [m], chl&CDM minus chl-only, north of 40°N. The attenuation depth is the reciprocal of the attenuation coefficient, k_{d}^{-1}. Calculated by averaging monthly k_{d}^{-1} values, using the monthly climatology chlorophyll concentration from the final 100 years of the biogeochemical model output and satellite-derived $a_{\mathrm{dg}}(443)$, panel (a). Negative values indicate a shallower attenuation depth. Contour interval is 10m. Adapted from Kim et al. (2015).

The ocean model is coupled to the GFDL thermodynamic-hydrodynamic sea ice simulator (SIS) (Winton, 2000). The SIS calculates the mass, movement and thermodynamic properties of one snow layer and two ice layers. Ice is added to the bottom layer in the form of congelation ice from freezing at the ice-ocean interface and frazil ice formed in the ocean mixed layer. Congelation ice is formed when the latent heat flux at the bottom of the ice pack, M_b [W m^{-2}], is less than zero. Changes in modeled latent heat depend on changes in sea surface temperature T_o [°C], lower layer ice temperature T_2 [°C] and thickness of the ice layer h_i [m]. This energy flux is calculated as the difference between the ocean-to-ice

904 bottom heat flux and the conductive flux of heat upward from the ice bottom:

$$M_b = F_b - \left[\frac{4K_i(T_f - T_2)}{h_i} \right],$$ (3.5)

905 where F_b [W m^{-2}] is the oceanic heat flux to the ice bottom, K_i [W m^{-1} $^\circ$C^{-1}] is the ther-

906 mal conductivity of the ice layer, and T_f [$^\circ$C] is the temperature of the ice-ocean interface

907 (fixed at the salinity-dependent freezing temperature of water). The ocean-to-ice heat flux,

908 F_b, is a linear function of the ocean-ice temperature difference:

$$F_b = K_o(T_o - T_f),$$ (3.6)

909 where K_o [W m^{-2} $^\circ$C^{-1}] is the thermal conductivity of the boundary layer at the ice-ocean

910 interface. Frazil ice is formed in the uppermost grid cell of the ocean when the temperature

911 of that box drops below freezing, supplying the required energy flux to return water in the

912 grid cell to the freezing point. Additionally, snow below the water line is converted to snow

913 ice. Solar radiation penetrates through sea ice and is attenuated with an optical depth of

914 0.67m.

915   For this study, model runs were conducted with and without light attenuation by CDM.

916 The GFDL CM2Mc ESM with BLING ocean biogeochemistry was spun up for 1500 years

917 with the Manizza et al. (2005) k_d parameterization. Two model runs were initialized from

918 this spun up state and were integrated for an additional 300 years: (1) the "chl&CDM"

919 model run utilizes the full k_d(bg) parameterization, Eq. 3.4 and (2) the "chl-only" run

920 which calculates the light attenuation coefficient with the chlorophyll-dependent term only:

921 $k_\mathrm{d}(\mathrm{bg}) = 0.0232 + 0.0513 \cdot \mathrm{chl}^{0.668}$.

922 ## 3.3 RESULTS

923 We analyze the final 100 years of the two model runs. The difference between the two

924 model runs (chl&CDM minus chl-only) shows the impact of added shortwave attenuation

925 by CDM. We present average results over the final 100 years of the 300-year model runs

926 to average over the interannual variability and so that our data does not include influences

927 from the spinup period. The model output has a monthly resolution.

928 A comparison of ice extent from the final 100 years of this study's control run (chl-

929 only) and satellite-derived monthly climatological values of ice extent from 1979 to 2007

930 (Comiso et al., 2008) shows good agreement (<5% error) from March to May with larger

931 discrepancies (up to 68%) from June to September. Our model slightly overestimates ice

932 extent during the winter months and significantly underestimates ice extent during the warm

933 summer months (see Table 3.1). The geographic extent of ice coverage in our model runs

934 (illustrated by the ice thickness in Fig. 3.2a) mostly aligns with observations from Laxon

935 et al. (2003) and Comiso et al. (2008), except in the Pacific sector where modeled ice

936 coverage extends throughout and south of the Sea of Okhotsk. Laxon et al. (2003) observed

937 thickest ice adjacent to the Canadian Archipelago. In our model run, thickest ice is found

938 in the East Siberian Sea.

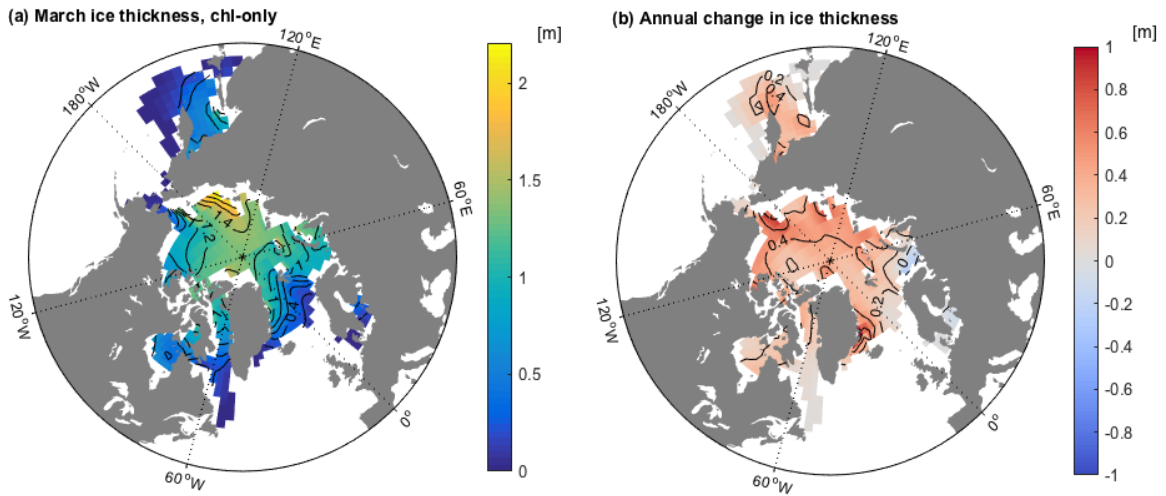939 Northern hemisphere (NH) ice thickness is greater when light attenuation by CDM is

Figure 3.2: (a) Modeled ice thickness [m] for March, averaged over the final 100 years of the chl-only model run. (b) Annual change in ice thickness [m], chl&CDM minus chl-only. Calculated by adding the monthly change in ice thickness at each grid cell over the 100-year monthly climatology. Countour interval is 0.2m for both panels.

included (Fig. 3.2b). Fig. 3.3a shows the total ice extent for the two model runs on the

model grid. The annually averaged total NH ice extent, which we consider to be the area

where ice is present at least one month during the year, is 6% larger when CDM is included,

whereas the annually averaged total NH ice mass is 5% greater in the chl&CDM model run.

In the following analysis, we compare all ice-covered regions against permanently ice-

covered regions to show how surface ocean heating is affected by permanent ice cover. We

define the "total ice domain" as grid cells where sea ice is present at least one month during

the year from both model runs and the "permanent ice domain" as grid cells where modeled

sea ice is present during all months of the year in both runs. The extent of these domains

are shown in Fig. 3.3. Using an arbitrary latitude boundary to define the domain, such as

the Arctic Circle, does not capture the entire ice extent and thus would be inadequate for a

study comparing the hydrodynamics under the modeled ice.

Table 3.1: Ice extent from this study's control run, in which light attenuation is a function of chlorophyll only, and satellite monthly climatology from Comiso et al. (2008) from 1979-2007, in 10^6 km^2. Data shown for March to September. Percent error calculated as ($\frac{\text{modeled - observed}}{\text{observed}}$).

Month	chl-only	Comiso et al. (2008)	Difference	% error
March	15.57	15.19	0.38	3 %
April	15.09	14.47	0.62	4 %
May	13.44	13.11	0.33	3 %
June	10.35	11.78	-1.43	-12 %
July	6.19	9.70	-3.51	-36 %
August	2.61	7.50	-4.89	-65 %
September	2.21	6.83	-4.62	-68 %

As the near-surface heating is proportional to the coefficient k_d (Eq. 3.4), the decrease in attenuation depth seen in Fig. 3.1b results in increased near-surface heating. Changes in light attenuation from including CDM are strongly concentrated in the northern hemisphere high latitude region, suggesting locally driven impacts. Three key heating mechanisms link the optical forcing (adding CDM) to increased ice extent: penetrating shortwave radiation, vertical diffusion of surface heat fluxes and vertical mixing. In-water shortwave radiation is attenuated at shallower depths, trapping heat near the surface. In the month of July, there is generally more shortwave heating in the upper 10m (Fig. 3.4a) and less shortwave heating from 20m to 30m (Fig 3.4b). In the 20m to 30m range, temperature changes are generally of the same sign as shortwave heating (Fig. 3.4d). However, in the upper 10m, there are regions with cooler temperatures coincident with increased shortwave heating (compare panels a and c of Fig. 3.4). As it will be shown later on, differences in surface heat fluxes and vertical mixing generally act to cool surface waters during summer months when CDM

(a) Total Ice Domain
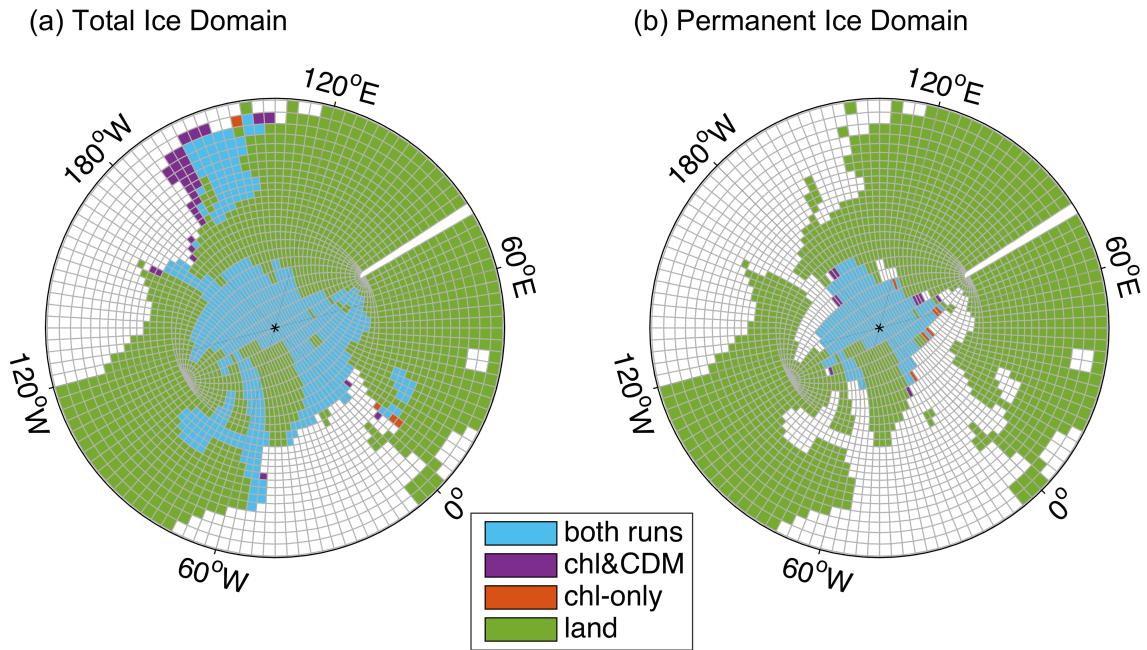
(b) Permanent Ice Domain

Figure 3.3: Light blue areas indicate regions where ice is present in both model runs. Purple and orange regions are areas where ice is present for either the chl&CDM or chl-only model runs, respectively. Land is designated by green grid cells. In this paper, we define the "total ice domain" as areas where ice is present at least one month during the year for the chl&CDM and chl-only model runs (light blue, orange and purple areas in panel a). The "permanent ice domain" includes areas where ice is present throughout all months of the year in both model runs (light blue areas in panel b). The CM2Mc model grid is overlaid in gray.

965   is included.

966   Here we describe the mechanism by which the inclusion of CDM alters the heat budget

967   of the upper 100m of the water column throughout the year in the high latitude northern

968   hemisphere. A summary of the argument is as follows: (1) penetrative shortwave radiation

969   is absorbed closer to the surface during the summer, which increases SSTs but reduces

970   heating below 20m, (2) increased summertime SSTs lead to more surface ocean heat losses

971   (3) colder deep water is entrained into the mixed layer in the autumn and winter months,

which (4) cools SSTs. The increase in ice mass and extent in the chl&CDM run are directly

linked to colder autumn and winter SSTs. Additional atmospheric effects reduce ocean

surface radiative fluxes, which further reduce upper ocean heating. We do not include

heating by vertical and horizontal advection in our analysis because the change in total

heat transport in the high latitude northern hemisphere is close to zero. The change in

vertical advective heat flux almost exactly cancels the change in horizontal advective heat

flux into the Arctic (as calculated at 65°N), producing an annually and regionally averaged

change in advective heat flux of 0.05 W m^{-2}.

3.3.1 TEMPERATURE TENDENCY

The temperature tendency, or the time derivative of local temperature changes, is the

sum of all modeled in-water heating sources. The differences in the annual cycle of tem-

perature (Fig. 3.5a) and temperature tendency (Fig. 3.6a) for the total ice domain shows

how including CDM changes the vertical structure of temperature and heating in the upper

100m. During the summer months, there is more heating in the upper 10m in the chl&CDM

model run and less heating below 10m. This pattern is widespread throughout the region

for shortwave heating during the month of July, as shown previously in Fig. 3.4a&b. Dur-

ing the autumn and early winter months, there is cooling near the surface and warming

below (Fig. 3.6a). As a result, SSTs are warmer from June to September and colder during

the rest of the year (Fig. 3.5a).

Changes in the annual cycle of the temperature tendency are well represented by the

sum of changes in the vertical heating terms between the two model runs. The sum of changes in shortwave heating, vertical diffusion and non-local mixing is shown in Fig. 3.6b, and bears close resemblance to the temperature tendency annual cycle shown in panel a.

For the permanent ice domain, changes in the annual cycle of temperature tendency are also largely accounted for by the sum of changes in the three major vertical heating terms. There is again a close resemblance between the differences in temperature tendency (Fig. 3.6c) and the sum of differences in heating by shortwave heating, vertical diffusion and non-local mixing (Fig. 3.6d). In the absence of open water, temperatures in the upper 100m are colder during the spring to summer months when CDM is included (Fig. 3.5b).

In the following subsections, the contribution by the three vertical heating terms to changes in total water column heating (i.e. temperature tendency) are analyzed individually. Fig. 3.7 shows the difference between the two model runs for the annual cycles of shortwave heating, vertical diffusion and vertical mixing.

3.3.2   SHORTWAVE HEATING

Of the three vertical heating processes, shortwave heating is the most directly linked to the optical forcing. Heating by penetrating shortwave radiation is concentrated near the surface when CDM is included (Fig. 3.7a, d). Since solar radiation is attenuated closer to the surface, there is less warming below the first vertical layer. This effect is most pronounced during the northern hemisphere summer months. For the total ice domain, shortwave heating integrated over the upper 10m and averaged from June to August increases by 6.17 W

Table 3.2: Heating term closure for the total and permanent ice domains. Vertical heating terms were integrated over the upper 10m and from 10m to 100m, then averaged over the months shown. Units are W m^{-2}. "Net" heating column is the sum of shortwave heating (swheat), vertical diffusion (vdiff) and non-local mixing (non-local) columns. "Temp Tend" is the integrated temperature tendency for the months and depths shown. "Residual" is calculated by subtracting the net heating column from the temperature tendency column. This shows the heating that is not accounted for by the three vertical heating terms.

Domain	Depth	Months	swheat	non-local	vdiff	Net	Temp Tend	Residual
Total	0m-10m	Jun to Aug	6.17	-0.139	-5.35	0.684	0.612	-0.0720
Total	10m-100m	Jun to Aug	-6.33	0.140	1.74	-4.44	-4.42	0.0254
Total	0m-10m	Sept to Dec	1.39	-3.84	1.70	-0.756	-0.770	-0.0143
Total	10m-100m	Sept to Dec	-1.41	3.50	1.16	3.24	3.12	-0.125
Permanent	0m-10m	Jun to Aug	3.24	-0.0571	-3.18	0.00291	-0.0814	-0.0843
Permanent	10m-100m	Jun to Aug	-3.33	0.0572	-0.0335	-3.31	-3.60	-0.296
Permanent	0m-10m	Sept to Dec	0.503	-2.56	2.18	0.127	0.0630	-0.0641
Permanent	10m-100m	Sept to Dec	-0.514	2.58	0.0661	2.13	1.97	-0.170

1012 m^{-2}, while shortwave heating decreases by 6.33 W m^{-2} from 10m to 100m (Table 3.2).

1013 For the permanent ice domain, shortwave heating increases by 3.24 W m^{-2} integrated over

1014 the upper 10m and decreases by 3.33 W m^{-2} integrated from 10m to 100m and averaged

1015 from June to August (Table 3.2).

1016 ### 3.3.3 VERTICAL MIXING

1017   As previously noted, the non-local mixing term represents mixing due to eddies that

1018 span the mixed layer. This process vertically redistributes heat mostly during autumn and

1019 winter months, when the mixed layer deepens and cold water is entrained from below the

1020 mixed layer. There is cooling within the mixed layer and warming below the mixed layer by

1021 the non-local mixing term during these months, as shown in Fig. 3.7b, e. In the chl&CDM

1022 run, this change in vertical mixing cools surface waters relative to the chl-only run. As

discussed in the previous section, including CDM inhibits heating by penetrating short-wave radiation below 10m during summer months. Non-local mixing delivers these colder deep waters to the surface while mixing down warmer surface waters from September to December.

There is more near-surface cooling by non-local mixing in the total ice domain than in the permanent ice domain. The average change in heating by non-local mixing from September to December is -3.84 W m^{-2} integrated over the upper 10m of the total ice domain, compared to -2.56 W m^{-2} in the permanent ice domain. From 10m to 100m, the change in heating by non-local mixing is also greater in the total ice domain than in the permanent ice domain during these months (Table 3.2). Since the total ice domain has a stronger temperature gradient at the end of the summer, more heat is vertically redistributed by non-local mixing in the autumn and winter months.

3.3.4 VERTICAL DIFFUSION (SURFACE HEAT FLUXES)

Including CDM has indirect effects on the atmosphere and ice which contribute to water column heating and cooling. Changes in sea surface temperature are accompanied by increased ice and clouds in the chl&CDM model run. The in-water vertical distribution of surface heat fluxes is included in the vertical diffusion term (Eq. 3.2). Differences in the vertical diffusion term between the two model runs are mostly due to changes in shortwave, longwave, evaporative and sensible surface heat fluxes. Surface fluxes are ocean relative. Shortwave surface heat flux is positive because it warms the ocean. When net longwave,

evaporative and sensible heat fluxes are negative, they cool the ocean.

When CDM is included, summertime SSTs increase over the total ice domain (Fig. 3.5a). This layer of warm water is cooled by additional evaporative and sensible cooling over the summer months. There is also less shortwave surface heat flux for most of the year (Fig. 3.8a,b). This is due to the increased clouds and ice in the chl&CDM model run. The decrease in heating by vertical diffusion during the summer months (Fig. 3.7c) is due to the negative total change in heat fluxes (Fig. 3.8a). The average change in heating by vertical diffusion from June to August integrated over the upper 10m is -5.35 W m^{-2} (Table 3.2).

The increase in ice also acts to insulate the water during autumn and winter months, resulting in less evaporative, longwave and sensible cooling at the ocean surface. Reduced cooling gives an overall positive sign change in surface heat fluxes from September to March (Fig. 3.8a). This coincides with the positive sign change in heating by vertical diffusion during these months (Fig. 3.7c). The average increase in heating by vertical diffusion from September to December integrated over the upper 10m is 1.70 W m^{-2} (Table 3.2). This increase in heating by vertical diffusion should be interpreted as reduced atmospheric cooling.

Monthly differences in radiative surface heat fluxes at the top of the ocean include the combined effect of atmosphere and ice changes, since radiative fluxes must penetrate both the atmosphere and ice before reaching the ocean surface (solid lines, Fig. 3.8b,e). Differences in net radiative surface heat fluxes at the top of the ice (dashed lines, Fig. 3.8b,e) are indicative of atmospheric changes only, such as cloud cover. We can calculate the

contribution to changes in radiative surface heat fluxes due to ice by taking the difference

between these two (Fig. 3.8c,f). Over the total ice domain, the annually-averaged change

in shortwave heat flux is -1.3 W m^{-2}. Increased cloud coverage accounts for 64% of the

decrease, while increased ice extent and thickness accounts for 36%. The average net

longwave cooling is reduced by 0.89 W m^{-2}, of which 48% is due to cloud effects and

52% is due to ice effects.

In the permanent ice domain, greater cloud coverage decreases surface shortwave heat

flux and greater ice thickness decreases sensible heat flux from May to August (Fig. 3.8d).

These changes coincide with decreases in heating by vertical diffusion in the upper 10m

(Fig. 3.7f). From September to December, there is less surface evaporative, longwave and

sensible cooling which results in increases in heating by vertical diffusion in the upper 10m

(Fig. 3.8d, Fig. 3.7f). The average surface shortwave heat flux decreases by 0.87 W m^{-2}, of

which 61% can be attributed to increased cloudiness and 39% can be attributed to increased

ice thickness. Average longwave heat flux increases (i.e. there is less net longwave cooling)

by 0.54 W m^{-2}, of which 46% is due to increased cloudiness and 54% is due to increased

ice thickness.

3.3.5 ROLE OF SST IN THE ICE AND ATMOSPHERIC MODELS

The optical attenuation by CDM has a direct impact on penetrating shortwave radiation

and indirect impacts on heating by vertical diffusion and non-local mixing. From June to

August, the direct effect of heating by penetrating shortwave radiation warms the upper

10m. From September to December, the indirect effect of cooling by non-local mixing cools the upper 10m. The net balance of heating and cooling for the upper 10m and from 10m to 100m (Table 3.2) shows that changes in these vertical heating terms mostly account for the changes in temperature tendency. These changes result in warmer SSTs from June to September and colder SSTs for the rest of the year in the chl&CDM run (Fig. 3.5).

Ice formation in the model depends on SST. The Sea Ice Simulator calculates the energy flux for forming congelation ice at the bottom of the ice pack according to Eq. 3.5. When the latent heat at the bottom of the ice is negative ($M_b < 0$), sea ice is added to the bottom ice layer. Since there is more ice in the chl&CDM model run, we expect to see more latent heat loss in this run than in the chl-only run. This can be achieved by decreasing the lower layer ice temperature T_2 in Eq. 3.5 and by decreasing the sea surface temperature (SST) T_o in Eq. 3.6. As shown in Table 3.3, SSTs are colder from October to May and lower layer ice temperatures are colder throughout the year in the chl&CDM model run. For a given freezing temperature and lower layer ice thickness, decreases in SST and lower layer ice temperature give a more negative M_b and thus more modeled sea ice. We also present the change in M_b only over areas where $M_b < 0$ to examine the change in energy balance responsible for freezing ice in Table 3.3. The largest changes in SST, lower layer ice temperature, and latent heat loss ($M_b < 0$) occur in January, where -0.11°C and -0.15°C changes in SST and lower layer ice temperature correspond to a -1.1 W m^{-2} change in latent heat. Although frazil formation is another mechanism that adds to bottom ice formation in the sea ice model, the difference in energy that goes into frazil formation between

Table 3.3: Difference (chl&CDM minus chl-only) in monthly ice thickness h_i [cm], sea surface temperature (SST) T_o [°C], lower layer ice temperature T_2 [°C], ocean to ice heat flux F_b [W m^{-2}] (from Eq. 3.6) and ice bottom melting & freezing energy flux M_b [W m^{-2}] averaged over the total ice domain. The final column is the difference in M_b only in areas where $M_b<0$ for a given month. This isolates areas where energy is going toward freezing ice.

Month	Δh_i	ΔT_o	ΔT_2	ΔF_b	ΔM_b	$\Delta (M_b<0)$
January	2.6	-0.11	-0.15	-2.5	-3.6	-1.1
February	3.2	-0.098	-0.11	-3.9	-4.0	-0.50
March	3.6	-0.096	-0.13	-4.7	-5.2	-0.56
April	3.8	-0.095	-0.086	-3.3	-3.5	-0.30
May	3.7	-0.081	-0.063	-2.0	-2.3	-0.15
June	3.7	0.011	-0.021	1.2	1.0	–
July	2.4	0.11	-0.016	4.7	4.6	–
August	1.0	0.14	-0.0091	4.2	4.7	–
September	0.52	0.094	-0.011	1.7	1.9	0.089
October	0.53	-0.035	-0.024	-1.0	-1.1	-0.18
November	1.0	-0.11	-0.054	-2.6	-3.0	-0.70
December	1.6	-0.12	-0.073	-2.9	-3.4	-0.84

the two model runs is less than 0.01 W m^{-2} for any given month. The resulting changes

in monthly sea ice thickness are listed in Table 3.3 alongside the changes in corresponding

monthly temperatures and heat fluxes.

In the permanent ice domain, the same physical mechanisms for summertime warming

and wintertime cooling are also at work but they are weaker because of the ice coverage.

In addition, the indirect atmosphere and ice effects from including CDM have a bigger

impact in this domain. As mentioned in the previous section, decreases in summertime

surface shortwave and sensible heat fluxes contribute to cooling in the vertical diffusion

term (Fig. 3.8d, Fig. 3.7f). The net effect is colder temperatures (Fig. 3.5b) and decreased

summertime temperature tendency (Fig. 3.6c) over the upper 100m. Colder SSTs increase

ice mass by 6% and ice extent by 2% in the permanent ice domain.

Areas with increased cloud coverage in the high latitude northern hemisphere generally overlap with areas where downward shortwave radiative flux through the atmosphere at the surface are diminished (not shown). We hypothesize that the increase in clouds is due to the decrease in SSTs throughout much of the year, which stabilizes the atmospheric boundary layer resulting in more low-level clouds. This is consistent with observations for the Northeast Pacific Ocean that suggest a negative correlation between SSTs and low-level clouds (Clement et al., 2009). Broccoli and Klein (2010) found this relationship to hold for simulations in the GFDL CM2.1 ESM.

3.4 Discussion and Conclusions

In this study, we reported results pertaining to ocean heating and ice formation associated with including an optically significant constituent in an ESM. Adding CDM attenuated light at shallower depths, preventing penetrative shortwave heating of deeper waters. Recent in-situ observations from an ice-tethered profiler by Jackson et al. (2010) highlight the role of subsurface summertime radiative heat storage in determining the annual cycle of ice formation and melt in the Arctic Ocean. A combination of salinity and temperature stratification from freshwater formed by ice melt was found to isolate warm waters below the mixed layer throughout the summer in the Canada Basin. Subsurface waters continued to warm via penetrating solar radiation until the autumn months when ice stopped melting and the salinity stratification broke down. Our modeling study suggests that if subsurface

summertime radiative heat storage were diminished in the Arctic Ocean, colder waters would be mixed up to the surface during the autumn and winter months, aiding ice formation in the wintertime. This physical mechanism should be further investigated in higher resolution regional models and verified by additional in situ observations.

Variations in the seasonal cycle of ice extent between ESMs can change the net effect of heating terms on SST and subsequently ice formation. In this study, increased summertime penetrative shortwave heating resulted in warmer SSTs over the total ice domain. Over the permanent ice domain, summertime SSTs were colder due to increased cloudiness and sensible cooling. The difference between these two domains is the seasonal ice extent, or areas where ice is present during some (but not all) months of the year. The proportional areal extent of this seasonally varying ice region will largely determine the relative contribution of the vertical heating terms to domain-averaged heating and temperature in a given ESM.

Including CDM in an ESM affects key heating processes that are responsible for variations in ice growth and decay across coupled global climate models. In a comparison of 14 coupled global climate models, Holland et al. (2010) found that models with larger annual Arctic ice melt were generally those with stronger absorption of shortwave radiation in the summer. Models with thicker ice simulated less net surface longwave heat loss during the winter months. The results in this study also show that summertime shortwave radiation and wintertime net longwave cooling are key processes that contribute to ice melt and formation. The chl&CDM run showed greater penetrative shortwave heating near the surface during the summer months and less longwave cooling throughout the year. These changes

resulted in a larger amplitude of annual ice growth and melt (based on ice thickness) and overall thicker ice when CDM was included. Studies predicting the future of Arctic sea ice should consider the sensitivity of their results to the optics in the model configuration.

The optical model used in this study, as reported in Kim et al. (2015), improves upon an existing parameterization for the light attenuation coefficient, k_d, by adding a term to include light attenuation by CDM. This study demonstrates one method of incorporating key optical constituents into global climate models. While computationally efficient and easy to implement in existing ESM and OGCM optical models, this method assumes a fixed optical relationship between k_d, chlorophyll concentration and $a_{dg}(443)$. Other optical modeling approaches involve calculating the in-water irradiance based on the modeled inherent optical properties (IOPs) of aquatic constituents (Dutkiewicz et al., 2015) and radiative transfer modeling (Mobley, 2011; Mobley et al., 2015). These approaches more accurately represent the underwater light field and similar approaches should be used in future studies to investigate connections between ocean optics, heating and ice.

Our finding that including CDM results in greater ice mass generally seems to contradict previous studies that modeled less ice with the inclusion of chlorophyll (Wetzel et al., 2006; Lengaigne et al., 2009; Patara et al., 2012). These studies compared a base case scenario with fixed attenuation depth to a model run that included chlorophyll predicted by a biogeochemical model. One key difference between the current study and previous ones is that we predict chlorophyll concentration with a biogeochemical model in both our base case (i.e. "chl-only") and experimental (i.e. "chl&CDM") model runs. By comparing two

model runs with model-predicted chlorophyll, we capture differences in the annual cycle of phytoplankton bloom and decay unlike the previous studies with a fixed attenuation depth in the base case model run. Including CDM shoals the attenuation depth, which concentrates chlorophyll closer to the surface (Kim et al., 2015). Seasonal changes in biota in both model runs further attenuate light and affect ocean physics in our fully-coupled model setup. This biophysical feedback possibly contributes to the discrepancies between this and previous studies.

Another major difference between this and previous studies is the geographic distribution of changes in ocean color. Changes in light attenuation were concentrated in coastal regions and the Arctic based on our satellite data product. This is likely due to the fact that riverine discharge during the spring freshet is one major source of CDOM to the Arctic Ocean. Stedmon et al. (2011) found greatest absorption by CDOM associated with peak discharge rates in all major Arctic river basins.

Future studies can improve upon our simulations by interactively modeling CDOM instead of prescribing its optical attenuation based on a satellite dataset. Riverine discharge is one known source of CDOM. It has also been known to degrade under prolonged exposure to sunlight. Photobleaching was found to diminish the light absorption coefficient for CDOM at 440nm by 34% from spring to summer in the western Arctic Ocean surface waters (Matsuoka et al., 2011). These major sources and sinks could be incorporated into an optical model for predicting CDOM absorption, which would be a powerful tool for predicting the future of ocean color in the Arctic Ocean. As shown in this study, the asso-

ciated changes in optical properties could have important consequences for Arctic sea ice
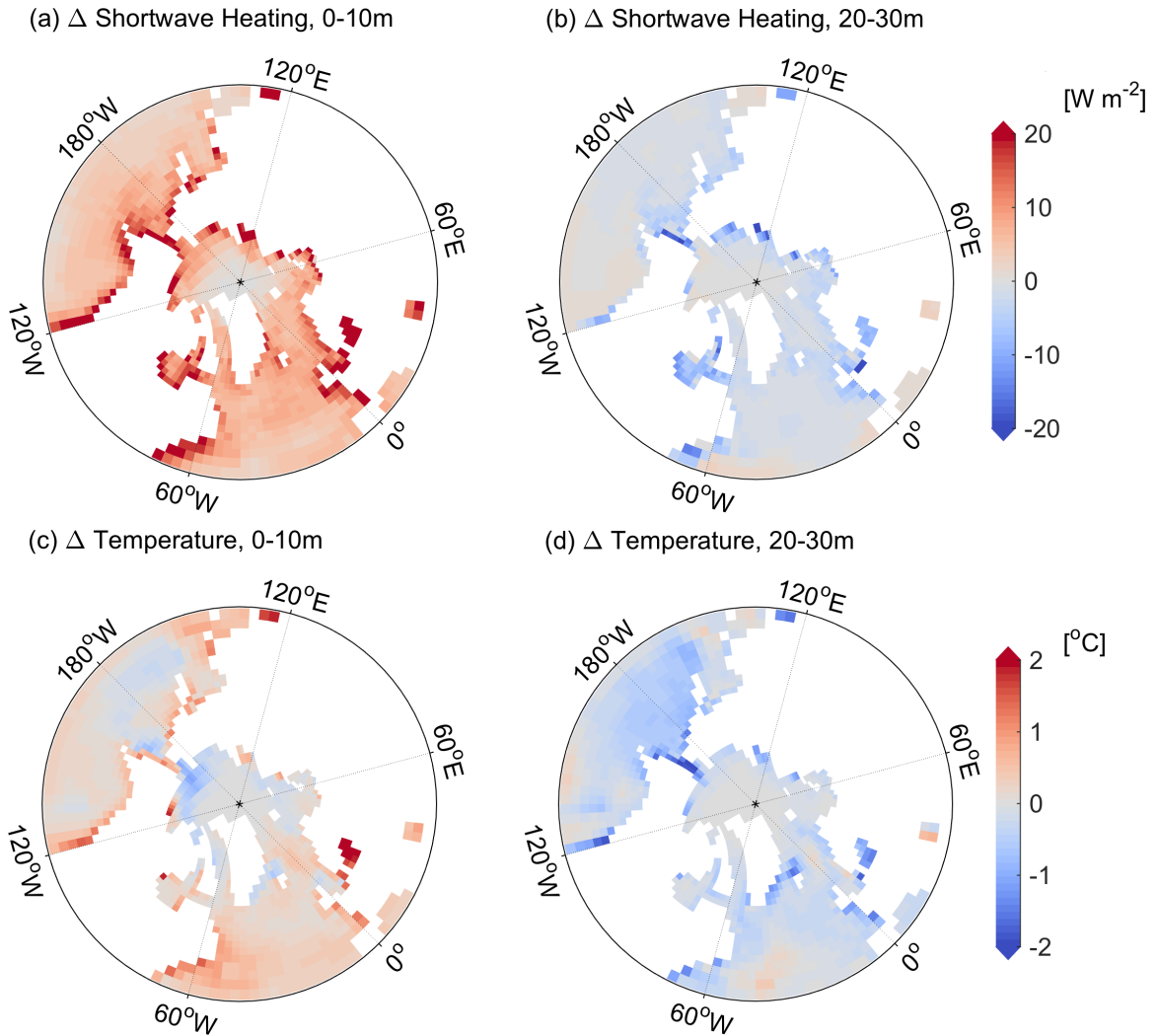
thickness and extent.

Figure 3.4: Difference (chl&CDM minus chl-only) in in-water (a)&(b) shortwave heating [W m^{-2}] and (c)&(d) temperature [°C] for July, averaged over the final 100 years of the two model runs. Panels (a)&(c) show the differences in shortwave heating and temperature for the surface layer, which includes the upper 10m, (b)&(d) show the differences from 20m to 30m depth.
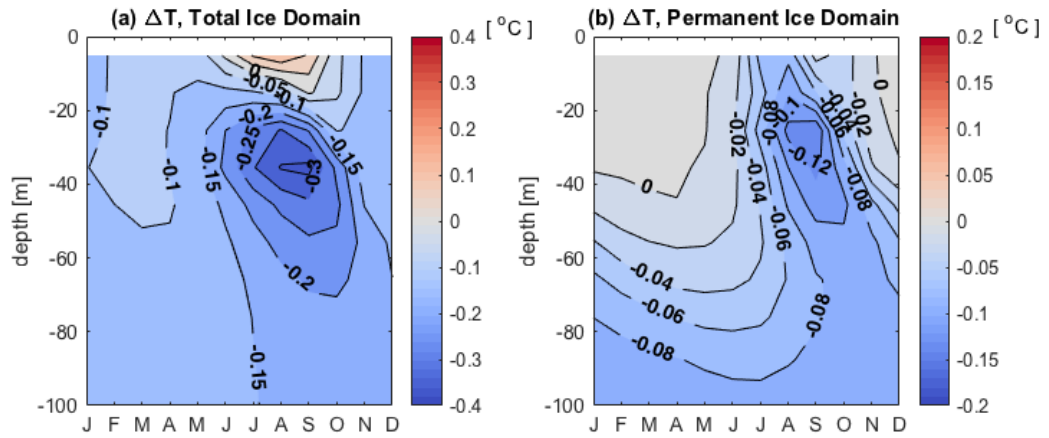
Figure 3.5: Monthly difference (chl&CDM minus chl-only) in ocean temperature [°C] for the upper 100m, averaged over (a) the total ice domain and (b) the permanent ice domain.
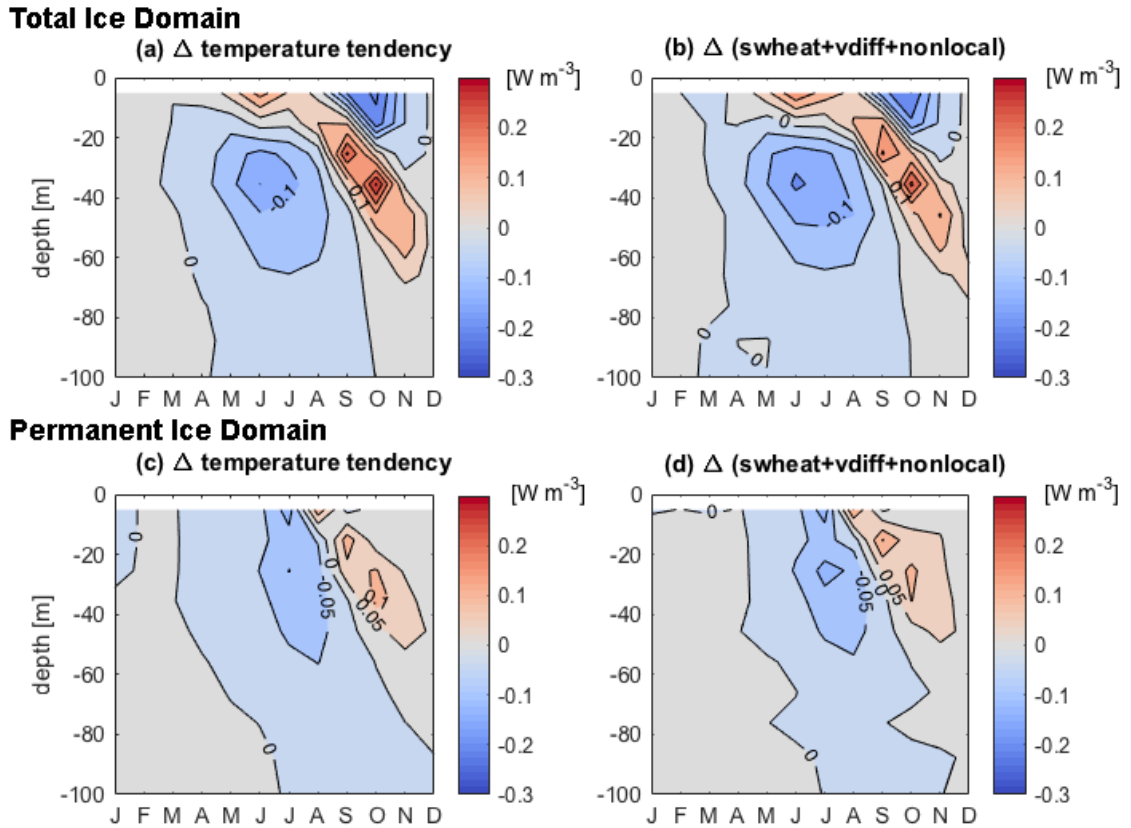
Figure 3.6: Monthly difference (chl&CDM minus chl-only) in temperature tendency and sum of major vertical heating terms for the upper 100m, horizontally averaged over the total ice domain in [W m^{-3}]. Panels (a) & (b) are for the total ice domain; (c) & (d) for the permanent ice domain. Major vertical heating terms include shortwave heating, vertical diffusion and non-local mixing.
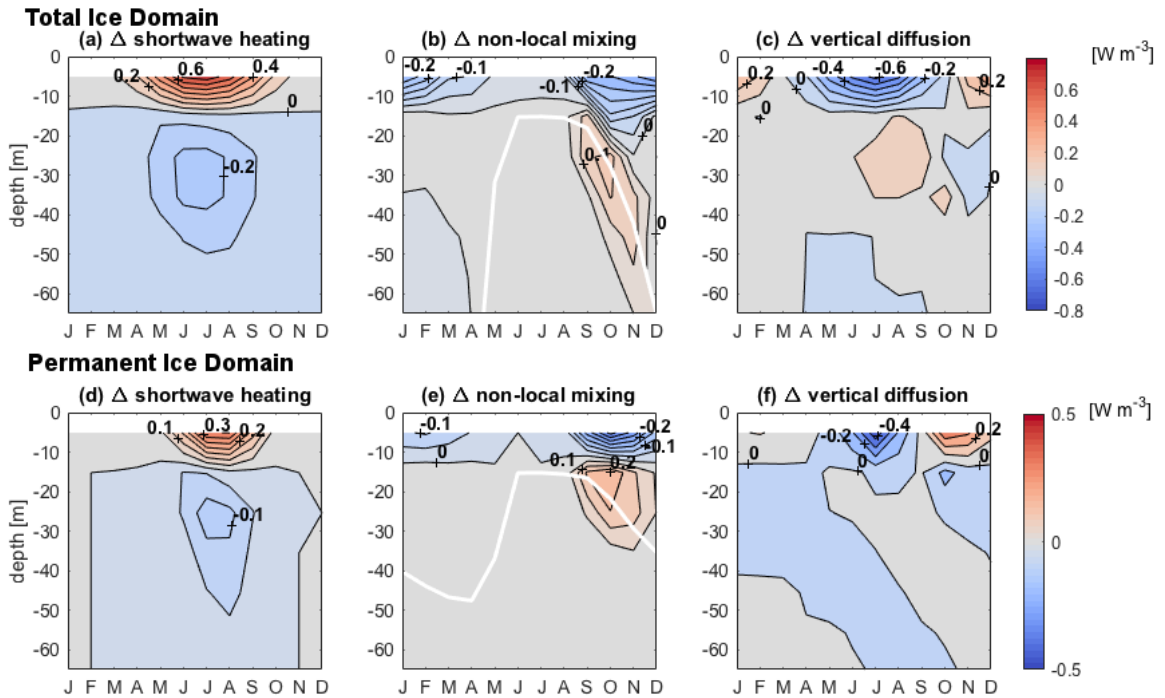
Figure 3.7: Monthly difference (chl&CDM minus chl-only) in shortwave heating, non-local mixing and vertical diffusion for the upper 65m over the total ice domain (panels a, b, c) and the permanent ice domain (panels d, e, f), in [W m^{-3}]. The sum of (a), (b) and (c) gives Fig. 3.6b; sum of (d), (e) and (f) gives Fig. 3.6d. Bold white line in (b) and (e) indicates mixed layer depth for the chl&CDM model run. Mixed layer depths for the total ice domain are between 101m to 164m from January to April.
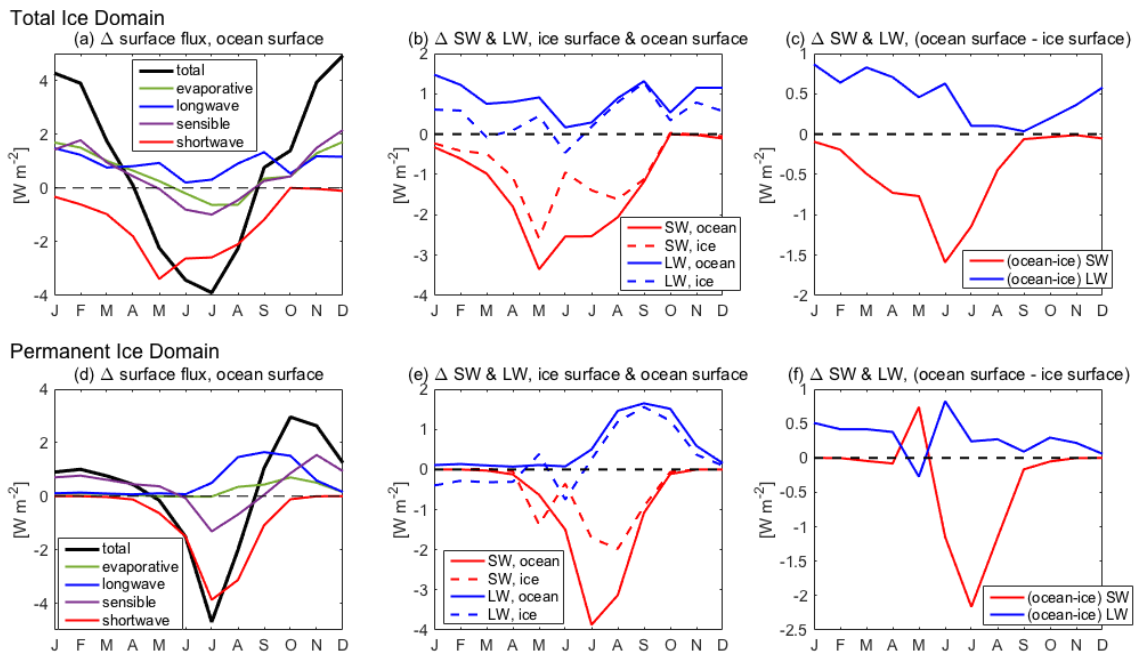
Figure 3.8: Difference (chl&CDM minus chl-only) in monthly surface heat fluxes [W m^{-2}] for the total and permanent ice domains. Panels (a) & (d) show the changes in major surface heat fluxes at the ocean surface. Net shortwave (SW) and longwave (LW) surface heat fluxes at the ocean surface and ice surface shown in (b) & (e). Panels (c) & (f) are the change in ocean surface heat fluxes that can be attributed to increased ice in the chl&CDM model run. This is calculated by taking the difference in the net radiative fluxes at the ocean and ice surfaces (i.e. solid minus dashed lines from panels b & e). Surface fluxes are ocean relative. Positive changes indicate increased ocean heat gain or reduced ocean heat loss. Negative changes indicate reduced ocean heat gain or increased ocean heat loss.

Chapter 4

Ocean yellowing increases sea surface temperature extremes

4.1 INTRODUCTION

Coastal waters are known to contain colored organic materials, often associated with the breakdown of terrestrial organic material. These materials tend to absorb most strongly at shorter wavelengths associated with blue-green and ultraviolet (UV) light. One result of this absorption is to make the water look more yellow. This effect arises from the fact that these colored materials absorb most strongly in the blue wavelengths where pure water is most transparent to light, and so acts to confine solar heating near the ocean surface.

Almost all Earth System Models operationally run for climate projection assume that the attenuation of sunlight in the ocean depends only on the concentration of chlorophyll-a, the primary photosynthetic pigment in phytoplankton (Morel, 1988). In doing so, light attenuation by all aquatic materials is presumed to vary in proportion to phytoplankton abundance. This so-called bio-optical approximation often does not apply in coastal regions and for large expanses of the ocean poleward of 40° (Siegel et al., 2005a). As suggested by work from lakes and estuaries, terrestrial processes largely control the abundance of optically active organic matter. In oceanic environments, colored dissolved organic matter (CDOM) is produced as a by-product of microbial metabolism (Nelson et al., 2004). Neither of these processes mechanistically vary proportionally with phytoplankton growth. Therefore, light attenuation by CDM should be modeled independently of chlorophyll concentration.

In this work we show that the light attenuation by CDM in the ocean systematically increases the range of sea surface temperatures (SSTs). The similar impact of chlorophyll in trapping heat near the surface has been examined in a number of recent studies (Manizza

et al., 2005; Gnanadesikan and Anderson, 2009; Patara et al., 2012). While one might naively expect that trapping heat near the surface would produce warming everywhere, the concomitant cooling of the deeper ocean has been found to be important as well. In the tropics this cooling was found to sharpen the thermocline, with the cold signal upwelling along the equator and enhancing the cold tongue (Anderson et al., 2007).

To date, studies of the role of solar absorption on climate have focused on impacts on the mean state or on long-period variability such as the El Nino Southern Oscillation (Murtugudde et al., 2002; Ballabrera-Poy et al., 2007; Anderson et al., 2007, 2009). Little attention has been paid to the impact of ocean color on the range of temperatures seen at individual sites. From an ecological standpoint, many organisms exist within a preferred temperature range and prolonged conditions outside of this range can result in significant mortality. Extended periods of time where temperatures exceed climatological values have been implicated in coral bleaching (Strong et al., 2006), while cold winters have been shown to kill larval fish such as the Atlantic Croaker (Lankford Jr and Targett, 2001).

The in-water attenuation of solar radiation due to CDM can be parameterized in terms of aquatic constituents. The absorption coefficient of light from detrital particles and dissolved colored materials, $a_{\mathrm{dg}}\,[m^{-1}]$, can be measured in situ and can also be estimated from satellite-derived ocean color data products. Recent work has combined these techniques to develop a parameterization of the attenuation depth of blue-green light in terms of chlorophyll concentration and satellite-estimated a_{dg} at a wavelength of 443nm (Kim et al., 2015). Using this parameterization, we have performed simulations with an Earth System Model

1253 in which we let (1) $a_{\mathrm{dg}}(443) = 0$ everywhere but retain the impact of model-predicted

1254 chlorophyll and (2) allow $a_{\mathrm{dg}}(443)$ to take the value found by the satellite ocean color data

1255 product. The difference between these two simulations isolates the impact of optical atten-

1256 uation by CDM in the Earth System. The following results show the impact of widespread

1257 ocean yellowing, since CDM preferentially absorbs blue light.

1258 ## 4.2   METHODS

1259   The model experimental setup and configuration summarized here are identical to that

1260 of Kim et al. (2015, 2016). The GFDL CM2Mc (Galbraith et al., 2011) with BLING

1261 biogeochemistry (Galbraith et al., 2010) is an IPCC-class Earth System Model (ESM)

1262 with fully coupled land-ocean-atmosphere-ice components. In-water spectral irradiance,

1263 $I_d(z, \lambda)$ $[W\ m^{-2}]$, is calculated according to the assumption that light diminishes approxi-

1264 mately exponentially with depth: $I_d(z, \lambda) = I_d(0, \lambda)e^{\int_0^z k_d(z', \lambda)dz'}$, where $I_d(0, \lambda)$ $[W\ m^{-2}]$

1265 is the incident light at the surface of a layer and $k_{\mathrm{d}}(\lambda)$ $[m^{-1}]$ is the light attenuation coef-

1266 ficient for that layer. Higher abundances of aquatic constituents, such as phytoplankton or

1267 dissolved materials, diminish the fraction of light that passes through the water. The light

1268 attenuation coefficient is calculated at every depth as a function of the chlorophyll-a con-

1269 centration and the light absorption coefficient by colored detrital matter (CDM) at 443nm,

1270 $a_{\mathrm{dg}}(443)$ $[m^{-1}]$.

1271   In most other Earth System Model simulations, the light attenuation coefficient is cal-

1272 culated as a function of chlorophyll only. This employs the bio-optical assumption, which

states that the optical attenuation by all aquatic constituents co-vary with chlorophyll-a, the primary photosynthetic pigment in marine algae. In our simulations, we separate the optical attenuation by colored detrital matter (CDM) by using a parameterization for light attenuation that decouples the contribution by chlorophyll-a and CDM: $k_{\mathrm{d}}(z, bg) = 0.0232 + 0.0513 \cdot [chl]^{0.668} + 0.710 \cdot a_{dg}(443)^{1.13}$. Here, the light attenuation coefficient for the blue-green wavelengths, $k_{\mathrm{d}}(bg)$, is a function of both chlorophyll-a concentration, $[chl]$, and light absorption by CDM at 443nm, $a_{\mathrm{dg}}(443)$. The chlorophyll-a concentration used in calculating k_{d}(bg)is predicted by the biogeochemical model. Light absorption by CDM takes the value of the satellite-derived MODIS Aqua annual composite data product for $a_{\mathrm{dg}}(443)$ processed by the GSM algorithm (Maritorena et al., 2002) averaged from 2002 to 2013. We ran two model simulations for 300 years: (1) the control run, in which we let $a_{\mathrm{dg}} = 0$ and (2) the CDM run, in which we let a_{dg} take the satellite-prescribed value.

4.3   RESULTS

4.3.1   EXTREME SEA SURFACE TEMPERATURES

SSTs in the CDM run are both warmer and colder than the maximum and minimum temperatures from the control run globally. There is a widespread increase in the standard deviation of SST (Fig. 4.1b). Largest increases in maximum temperature are broadly distributed poleward of 35°(Fig. 4.1c). There are small changes in the annual mean SST, which are generally on the order of a few tenths of a degree (Fig. 4.1a).

Since repeat occurrences of extreme temperatures are important for marine ecosystems,

(A) ΔT_{mean}

(B) $\Delta \sigma T$

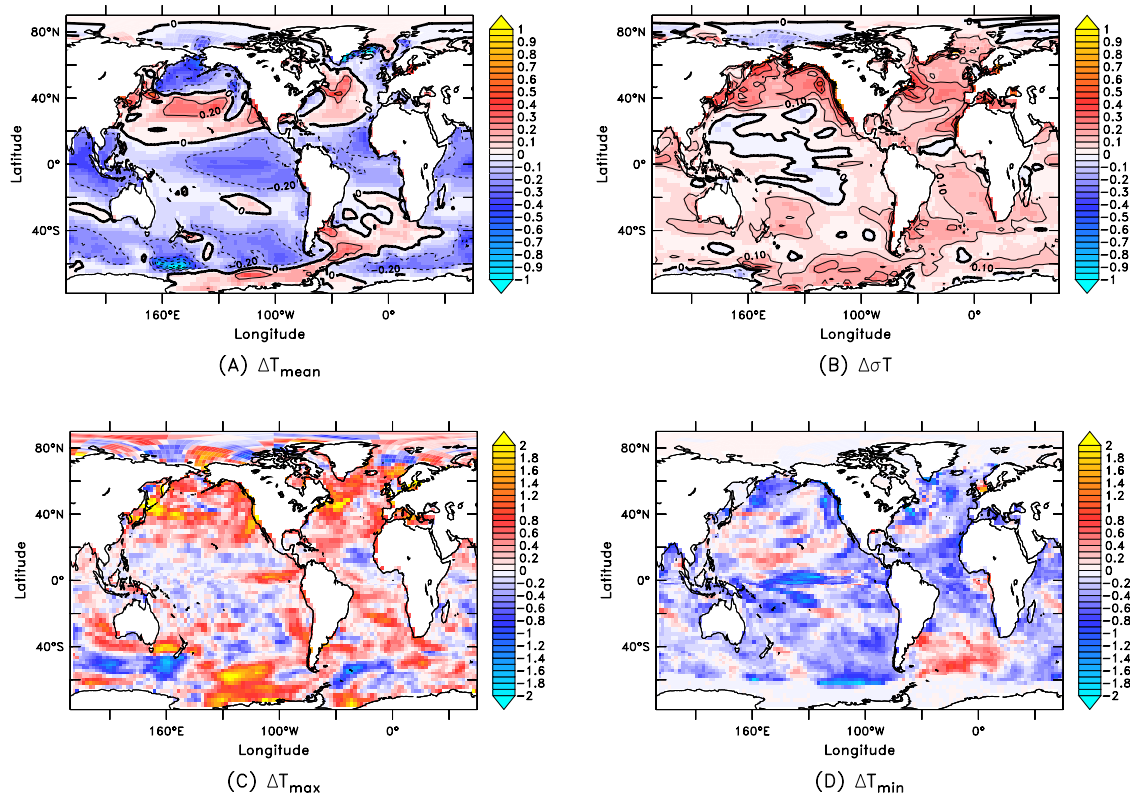(C) ΔT_{max}

(D) ΔT_{min}

Figure 4.1: Difference in (a) mean sea surface temperature, (b) standard deviation of temperature, (c) maximum temperature and (d) minimum temperature between the two model runs, all in $^{\circ}C$. CDM minus control for the final 100 years of the model simulations.

1293 we evaluate the number of times that the control run maximum and minimum temperatures

1294 are exceeded when CDM is included (Fig. 4.2). Two notable regions where minimum and

1295 maximum temperatures are exceeded span large sections of the North Pacific and North At-

1296 lantic Oceans. Maximum temperatures in the CDM model run exceed those of the control

1297 run along the U.S. West Coast, the East Coast of Canada and coastal Europe. In the North

1298 Pacific, colder minimum temperatures are widespread throughout and south of the Bering

1299 Sea and along the U.S. and Canadian West Coast. In the North Atlantic, minimum temper-

1300 atures are colder in the Irminger and Iceland Basins, as well as along coastal Europe. Some

89

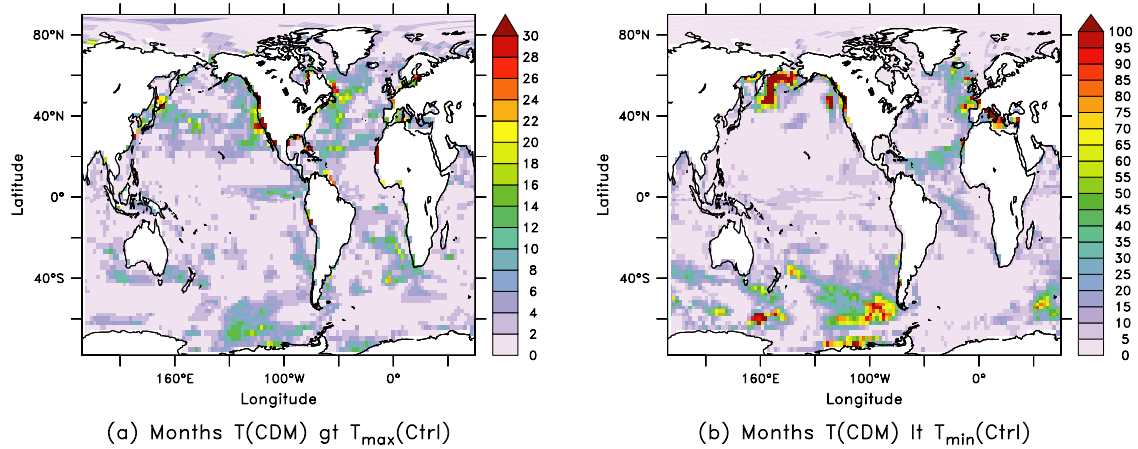(a) Months T(CDM) gt T$_{max}$(Ctrl)   (b) Months T(CDM) lt T$_{min}$(Ctrl)

Figure 4.2: The number of months where the SST [$°C$] in the CDM run exceeds the (a) maximum or (b) minimum SST of the control run during the last 100 years (1200 months). Note the difference in color bar axes.

regions with colder minimum temperatures overlap regions with warmer maximum temperatures, such as stretches of the U.S. West Coast. Overall, there are more occurrences of extreme cold temperatures than warm temperatures (note the difference in color bar scales in Fig. 4.2).

4.3.2   SHORTWAVE HEATING AND SST

Optical attenuation directly controls in-water heating by shortwave radiation. In this section, we investigate the relationship between shortwave heating anomaly from 0-10m and SST anomaly for the final 100 years of the CDM run only. A least squares regression on the time series of these two variables using model output from the CDM run shows variations in SST anomaly are well-predicted by variations in surface shortwave heating anomaly in select polar regions only. The coefficient of determination (R^2) is highest

(A) regression coefficient
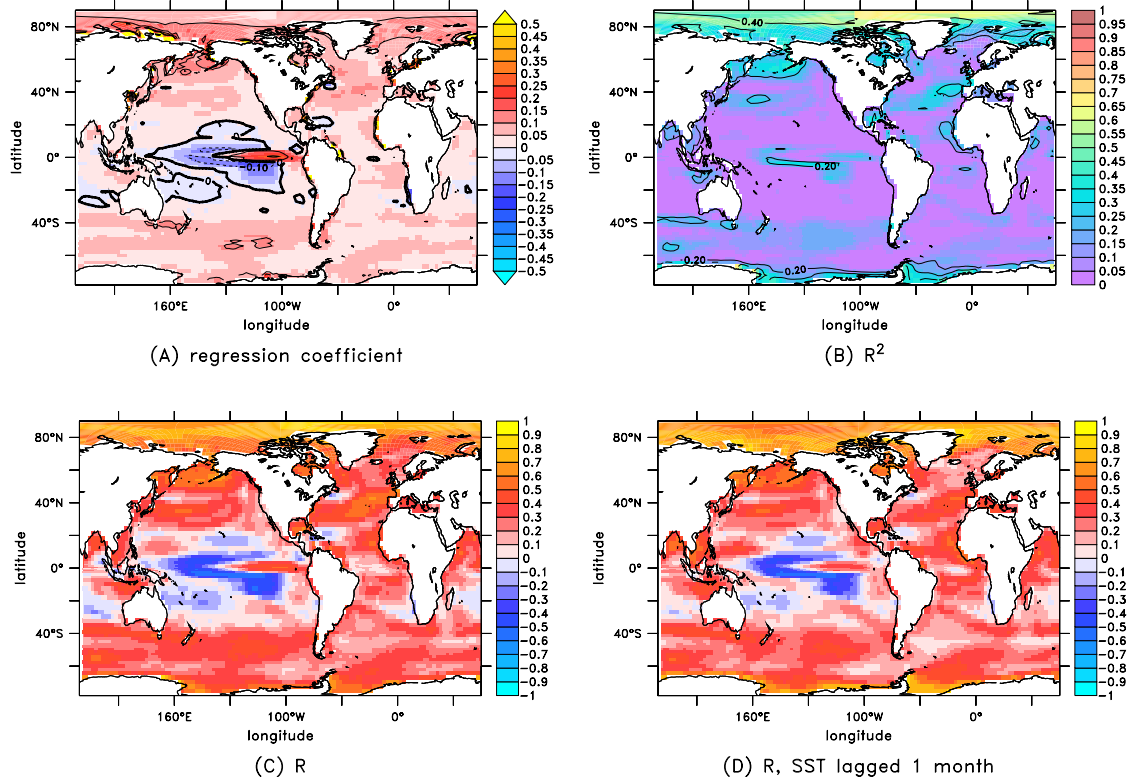
(B) R^2

(C) R

(D) R, SST lagged 1 month

Figure 4.3: Linear regression analysis on time series of anomalous penetrative shortwave heating in the upper 10m and anomalous SST: (a) regression coefficient [$°C/W\ m^{-2}$] (b) coefficient of determination, R^2 (c) correlation coefficient, R and (d) correlation coefficient, R, with SST anomaly lagging penetrative shortwave heating anomaly by 1 month. Contour interval for (a) is 0.1 $°C/W\ m^{-2}$, for (b) is 0.2.

throughout the Arctic Ocean and in coastal areas around Antarctica (Fig. 4.3b). In general, the two variables are positively correlated for most of the ocean (Fig. 4.3a, c). This correlation improves in some polar coastal regions when SST anomaly lags shortwave heating anomaly by one month (compare Fig. 4.3 c and d). SST anomaly in a given month is better predicted by shortwave heating anomaly in the prior month in these locations. The slope and correlation between shortwave heating and SST are negative in the Equatorial Pacific, but the coefficient of determination is small.

This analysis shows that surface shortwave heating anomaly is a poor predictor of SST anomaly for most of the ocean (Fig. 4.3b). Changing the light attenuation in the surface ocean directly affects the surface shortwave heating, but its effect on SST is complicated by air-sea fluxes and ocean circulation. In the following analysis, we analyze SST changes in the North Pacific and North Atlantic basins because these locations show a high occurrence of more extreme temperatures in the CDM run (Fig. 4.2) and larger changes in penetrative shortwave heating than in other locations. While there are other large regions with more extreme SSTs, there are small changes in the penetrative shortwave heating which suggests that the changes in SST may not be related to the difference in light attenuation between the two model runs.

4.3.3 Seasonal changes in heating and temperature: Northern Pacific Ocean

Summertime SSTs are generally warmer throughout the northern Pacific Ocean in the CDM run (Fig. 4.4a). On a basin scale, this can likely be attributed to the shallower attenuation depths in the CDM run, which increases heating by penetrative shortwave radiation in the upper 10m (Fig. 4.4c). Shoaling the attenuation depth also decreases penetrative shortwave heating below the surface layer, which contributes to colder subsurface temperatures (Fig. 4.4b, d). Upon closer examination, we find that areas with the largest increases in surface heating do not overlap with areas where largest increases in SST are found. This spatial mismatch can be explained by the average surface ocean circulation in the region.

(A) △ SST

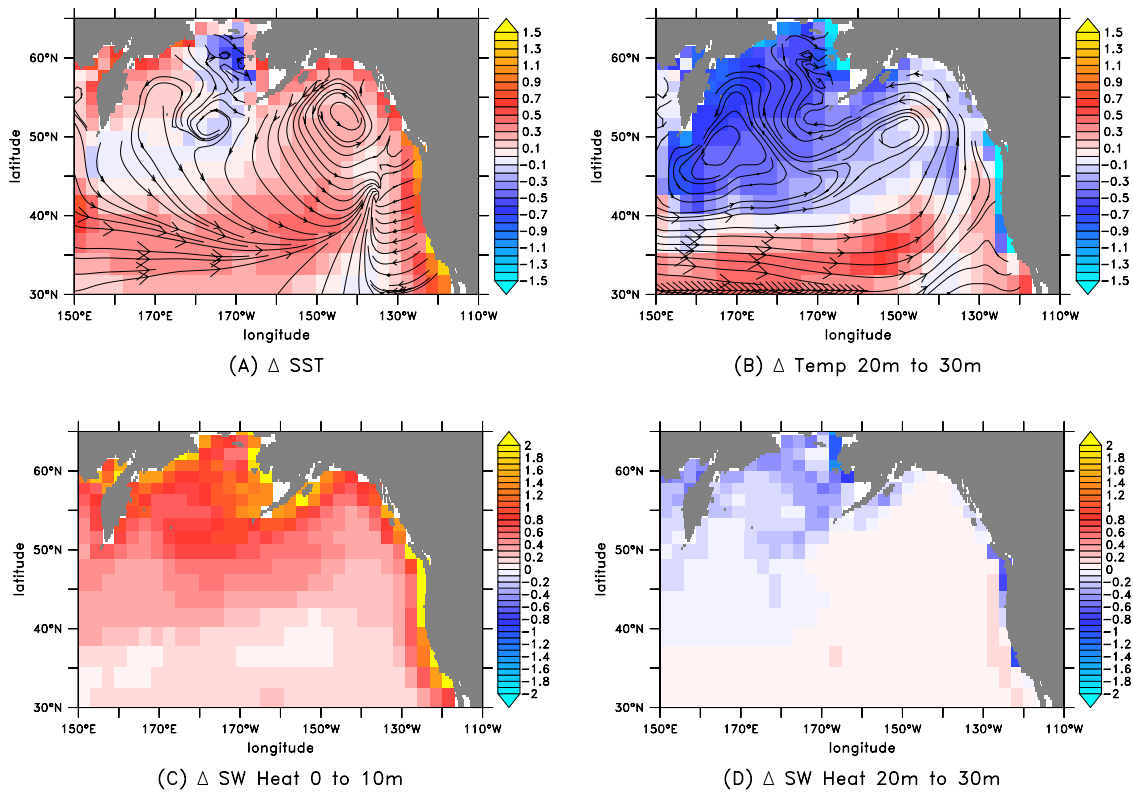(B) △ Temp 20m to 30m

(C) △ SW Heat 0 to 10m

(D) △ SW Heat 20m to 30m

Figure 4.4: North Pacific Ocean difference in July to September averaged (A) sea surface temperature $[°C]$, (B) temperature from 20m to 30m $[°C]$, (C) penetrative shortwave heating for the upper 10m $[W\ m^{-3}]$ and (D) penetrative shortwave heating from 20m to 30m $[W\ m^{-3}]$. CDM minus control run. Overlay: (A) 0 to 10m and (B) 20m to 30m average July to September ocean currents for the control run. Larger arrows on flowlines indicate faster currents.

In the northeastern Pacific Ocean, the eastward flow of the North Pacific Current forks northward into the Alaska Current and southward to join the California Current. July to September SSTs in are generally warmer in the CDM run along the North Pacific Current, throughout the California Current System and in the Alaska Gyre (Fig. 4.4a). The westerly winds throughout the region results in southward Ekman transport of the surface layer, which is apparent in average surface ocean circulation (Fig. 4.4a). These displaced waters

(A) △ SST

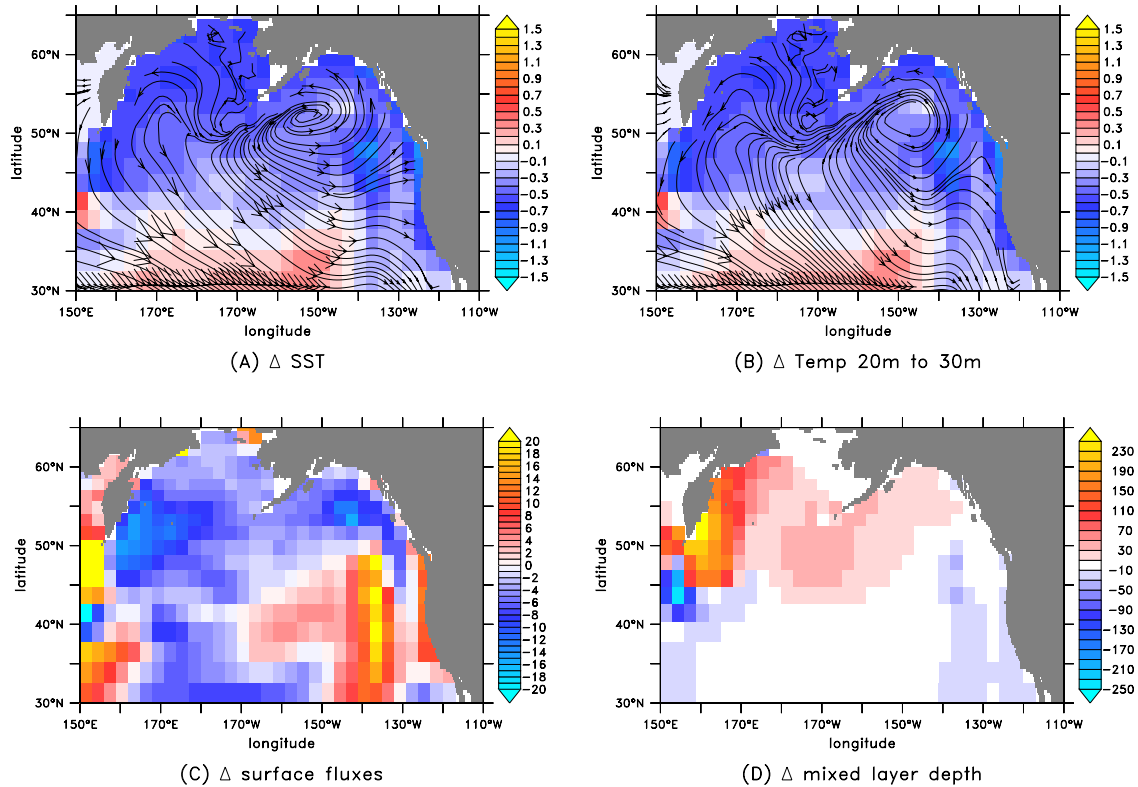(B) △ Temp 20m to 30m

(C) △ surface fluxes

(D) △ mixed layer depth

Figure 4.5: North Pacific Ocean difference in January to March averaged (A) sea surface temperature $[°C]$, (B) temperature from 20m to 30m $[°C]$, (C) net surface heat fluxes $[W\ m^{-2}]$ and (D) mixed layer depth $[m]$. Overlay: (A) 0 to 10m and (B) 20m to 30m average January to March ocean currents for the control run. Larger arrows on flowlines indicate faster currents. Difference in surface heat fluxes shown in (C) includes the net surface shortwave, longwave, evaporative, sensible, precipitation minus evaporation, and frazil fluxes at the top of the ocean.

1345   are replaced by water upwelling from below the Ekman layer.

1346   Although there are small increases in summertime shortwave heating from 0m to 10m

1347   along the North Pacific Current, SSTs along this current are generally warmer due to the

1348   southward Ekman transport of warm surface waters throughout the subpolar region (see

1349   35°N-40°N in Fig. 4.4a and c). The largest increases in summertime shortwave heating

1350   from 0m to 10m are found along the coasts and in the Bering Sea (Fig. 4.4c), but there are

colder SSTs in the Bering Sea. This is likely due to a combination of upwelling of colder subsurface water below the Ekman layer and delivery of colder waters from the Arctic Ocean through the Bering Strait. As shown in Kim et al. (2016), July SSTs are colder on both the Arctic Ocean and Pacific Ocean sides of the Bering Strait in the CDM run.

Wintertime SSTs and temperatures between 20m to 30m are generally colder throughout northern Pacific Ocean in the CDM run (Fig. 4.5a, b). SSTs in the CDM run are colder in part due to the upwelling of colder subsurface waters, as stronger winds intensify the Ekman transport and upwelling within the region during the winter months. Additionally, the mixed layer deepens in the wintertime, bringing colder deep waters to the surface.

The mixed layer is a layer of the ocean near the surface where properties such as temperature and salinity are well mixed vertically. It is generally shallower during summer months when solar radiation warms the surface ocean. A layer of warm water forms above the cooler water underneath and the water column is stably stratified. The mixed layer deepens in the fall and winter months, when strong winds across the ocean surface mix water below. Additionally, surface waters can become denser due to net atmospheric cooling and evaporation resulting in a situation where a layer of cold and salty dense water sits above warmer, fresher light water. In these situations the water column is unstable which can result in deep convective mixing.

The subpolar oceans are areas of significant ocean surface heat loss to the atmosphere, especially during the winter months. In the model run with CDM, air-sea heat loss intensifies in the Alaska Gyre and East Kamchatka Currrent/Oyashio Current regions (Fig. 4.5c).

(A) △ SST

(B) △ Temp 20m to 30m

(C) △ SW Heat 0 to 10m

(D) △ SW Heat 20m to 30m

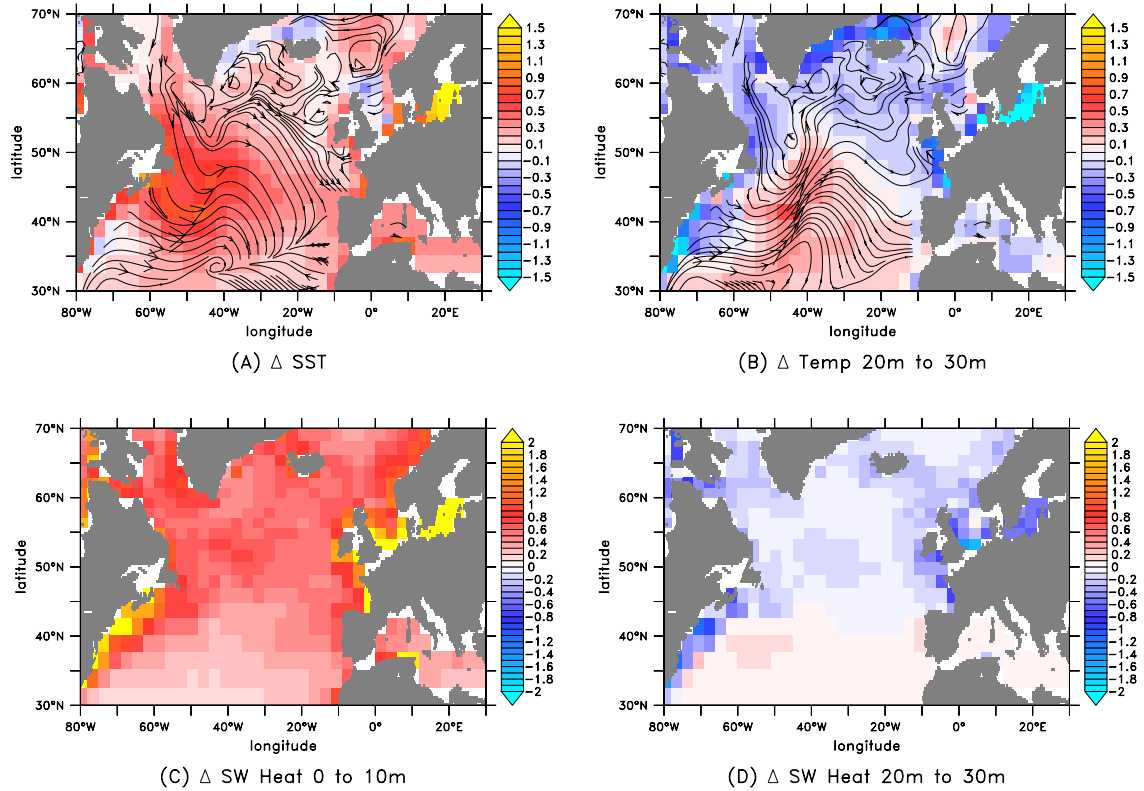**Figure 4.6:** North Atlantic Ocean difference in July to September averaged (A) sea surface temperature [$°C$], (B) temperature from 20m to 30m [$°C$], (C) penetrative shortwave heating for the upper 10m [$W\ m^{-3}$] and (D) penetrative shortwave heating from 20m to 30m [$W\ m^{-3}$]. CDM minus control run. Overlay: (A) 0 to 10m and (B) 20m to 30m average July to September ocean currents for the control run. Larger arrows on flowlines indicate faster currents.

1372   These regions are also places where the mixed layer depth increases by up to hundreds of

1373   meters (Fig. 4.5d). In the California Current System, there is less air-sea heat loss accom-

1374   panied by shallower mixed layer depths.

(A) △ SST

(B) △ Temp 20m to 30m
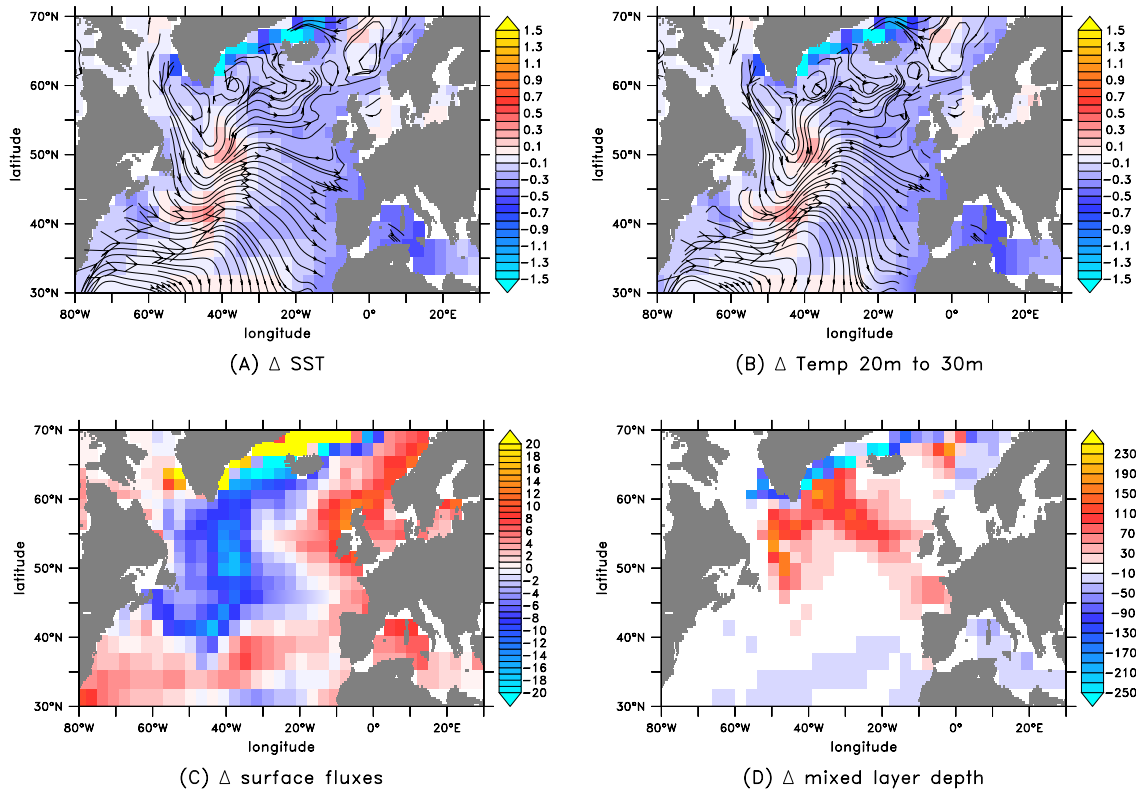
(C) △ surface fluxes

(D) △ mixed layer depth

Figure 4.7: North Atlantic Ocean difference in January to March averaged (A) sea surface temperature $[^\circ C]$, (B) temperature from 20m to 30m $[^\circ C]$, (C) net surface heat fluxes $[W\ m^{-2}]$ and (D) mixed layer depth $[m]$. Overlay: (A) 0 to 10m and (B) 20m to 30m average January to March ocean currents for the control run. Larger arrows on flowlines indicate faster currents. Difference in surface heat fluxes shown in (C) includes the net surface shortwave, longwave, evaporative, sensible, precipitation minus evaporation, and frazil fluxes at the top of the ocean.

1375 ### 4.3.4 SEASONAL CHANGES IN HEATING AND TEMPERATURE: NORTHERN ATLANTIC

1376 OCEAN

1377   In the northern Atlantic Ocean, increases in summertime shortwave heating in the upper

1378 10m are greatest near the coast (Fig. 4.6c), while the largest increases in SST are clustered

1379 around the region where the northward North Atlantic Current and southward Labrador

1380 Current converge on the western side of the basin (Fig. 4.6a). This is likely due to a com-

97

bination of warm surface waters being advected into the region as well as increased local surface shortwave heating. Shallower attenuation depths reduce the solar radiation that penetrates the surface layer, which results in generally colder temperatures and less short-wave heating from 20m to 30m (Fig. 4.6b, d). Temperatures from 20m to 30m are colder in the Ekman upwelling region north of the North Atlantic Current and warmer in the Ekman downwelling region south of the current.

The North Atlantic Current meanders northward and eastward before splitting into a northern branch which flows into the Norwegian Sea and Irminger Basin and a southern branch which joins the North Atlantic Subtropical Gyre. This northward flow of the North Atlantic Current is associated with the greatest observed annual mean air-sea heat loss in the world (Large and Yeager, 2009). Ocean surface water becomes denser as SSTs become cooler and surface waters become saltier due to heat loss and evaporation into the atmosphere. Deep water is formed in the high latitude Atlantic Ocean leading to convective events that can deepen the mixed layer to more than 1000m.

Wintertime SSTs and temperatures between 20m to 30m are generally colder through-out the region, except in the region where the North Atlantic Current and the Greenland current meet (Fig. 4.7a, b). This area of warmer temperatures is associated with greater net air-sea heat loss, which cools the water mass as it moves eastward (Fig. 4.7c). Mixed layer depths are generally deeper in the path of the North Atlantic Current, where greater net air-sea heat loss leads to deeper mixing (Fig. 4.7d). Colder SSTs in this region are likely a result of the deeper mixed layers which mix cold deep waters to the surface. There is

also likely some contribution by the the upwelling of colder waters in this subpolar Ekman

upwelling region, as in the case of the northern Pacific Ocean.

4.4 SUMMARY AND CONCLUSION

Including the optical attenuation by CDM has the effect of trapping solar radiation near

the surface, which reduces the intensity of shortwave radiation that penetrates the surface

layer. There were more occurrences of colder SSTs than warmer SSTs when compared to

the control run. We focused our analysis on the North Pacific and North Atlantic ocean

basins, where additional light attenuation by CDM reduced overall penetrative shortwave

heating and resulted in more extreme SSTs.

The location of warmer SSTs is largely influenced by the surface ocean currents. While

the greatest changes in shortwave heating are usually near coastal regions, largest increases

in SSTs were simulated in areas where major surface currents converge. Colder SSTs were

shown to be linked to Ekman upwelling and mixed layer depth. In both basins, the vertical

changes in heating by shortwave radiation resulted in colder subsurface water. These colder

subsurface waters are upwelled by Ekman upwelling resulting in colder SSTs in the CDM

run. Additionally, changes in SST were associated with greater net air-sea heat loss, which

led to deeper convective mixing. Deeper mixed layer depths delivered deeper, colder waters

to the surface and decreased SSTs.

Modeled temperature extremes are found in regions where anomalous temperatures

have been shown to disrupt ecosystem dynamics. In the California Current System, warmer

ocean temperatures have been associated with increased energy demand and reduced growth in North Pacific salmon (Welch et al., 1998). McGowan et al. (1998) report the biological consequences of changes in the physical mechanisms controlling primary production during warm and cold episodes in the California Current and Gulf of Alaska Gyre system. Historical records dating back to the 1950s show declines in zooplankton biomass, larval fish and pelagic species associated with substantial changes in phytoplankton biomass. In the North Atlantic Ocean, cold winters have been shown to kill larval fish such as the Atlantic Croaker (Lankford Jr and Targett, 2001).

We also showed that near-surface shortwave heating anomalies are most closely linked to sea surface temperature anomalies in high latitude oceans. In polar regions, the effect of warming temperatures on ecosystems has been largely associated with the decline in sea ice and ice algae. These are thought to have caused the decline in Antarctic krill and subsequent changes in the pelagic food web in the Antarctic Ocean in the previous decades (Atkinson et al., 2004). High latitude warming and changes in global precipitation patterns have the potential to dramatically change the amount and quality of terrestrial organic material delivered to the oceans via river runoff. Accurately incorporating this key connection between terrestrial and oceanic systems will be critical for predicting the magnitude and range of oceanic temperature changes. Changing trends in CDM abundance have the potential to make SSTs more extreme in the worlds oceans.

Chapter 5

Conclusion

In a long-term study of two inland lakes, Williamson et al. (2015) found that increased browning from increases in terrestrially-derived dissolved organic matter (DOM) led to greater thermal stratification and oxygen depletion. Two key species of zooplankton grazers decreased in the lake that experienced a 10m decrease in the 1% UV attenuation depth. There was no significant trend in chlorophyll-a concentration with an increase in fish populations, suggesting food web re-structuring. Over a 27-year period, browning changed the ecosystem structure, biogeochemistry and hydrologic properties of the lake. While similar findings have been reported for the effects of browning in lakes, the potential impacts for large scale changes in ocean color remain largely unstudied.

In the Gulf of Maine, increased river discharge from 2006-2010 was associated with a large increase in CDOM (Balch et al., 2016). This study also suggests the Gulf of Maine has yellowed in the last century based on historic observations of ocean color. Rivers are a major source of CDOM to the oceans (Blough and Vecchio, 2002), but will greater freshwater flux deliver more *optically active* DOM to the ocean?

In the Arctic, decreasing snow cover, melting glaciers, increasing precipitation and increasing river discharge have been observed in the last century (Serreze et al., 2000; Peterson et al., 2002). While this trend is expected to continue as temperatures continue to rise, the quality and composition of the DOM as well as changes in freshwater fluxes will largely determine how ocean color will change in the future. Previous work has related seasonal variations in the spectral characteristics of CDOM to shifts in the dominant source of organic material in Arctic rivers (Stedmon et al., 2011). Researchers studying the Arctic

Ocean have attempted to link dissolved organic carbon (DOC) measurements to CDOM absorption to remotely sense the temporal and spatial variability of riverine carbon flux from the rivers to the ocean (Griffin et al., 2011).

Much of this work has been motivated by the concern that vast carbon reserves currently bound up in permafrost will be released into the Arctic riverine and oceanic environment. Recent work characterizing the chemical composition of permafrost dissolved organic carbon has found it to be mostly biolabile, exhibiting aliphatic and carbohydrate-like molecular formulas. Microbial incubation experiments suggest they are rapidly degraded and are therefore unlikely to be found in the major Arctic rivers and in the ocean (Mann et al., 2015; Spencer et al., 2015). Furthermore, these molecules do not exhibit the aromaticity of optically active dissolved carbon molecules. In a review of work characterizing the chemical composition of CDOM, Coble (2007) reports that CDOM is likely composed of aromatic carbon molecules such as lignin, polyphenols, tannins and melanins. Sharpless and Blough (2014) suggest that CDOM absorption and photochemical properties originate from aromatic chromophores. There is evidence of an increasing proportion of bioavailable carbon in the DOC pool with a decreasing aromaticity in Arctic streams and rivers (Mann et al., 2015).

Changing freshwater fluxes and molecular composition of DOM in the ocean are likely to have important impacts on the ocean productivity and circulation, since the light in the surface ocean is responsible for phytoplankton growth and solar heating. Yet, these impacts are poorly studied. Recent modeling efforts to understand the role of optical attenuation by

CDOM in the global oceans highlight the importance of capturing its spatial and temporal variability in model simulations. Dutkiewicz et al. (2015) found significant shifts in the microbial community structure shifts associated with parameterizations that employ different assumptions about optical attenuation by CDOM. These changes were linked to a phytoplankton groups preferred spectrum of light and the role of CDOM in strongly attenuating blue wavelengths.

The work in this dissertation demonstrates that light attenuation by CDOM and NAP directly affect biology and heating on a global scale. Model simulations with the fully-coupled GFDL CM2Mc show how global concentrations of phytoplankton biomass and nutrients are affected by adding light attenuation by CDM (Kim et al., 2015). Chapters 2 and 3 of this dissertation investigate the role of changes in the vertical distribution of shortwave heating on SSTs, mixed layer depths and ice formation.

These modeling studies do not fully capture the temporal and spatial variability of CDOM in the natural environment and do not include its role in marine biogeochemistry. One major barrier to including CDOM in coupled hydrodyanmic-optical-ecosystem models is there are many remaining unknowns about the processes that create and destroy CDOM. This optically active subset of the DOM pool has yet to be fully chemically characterized, so it is difficult to quantify its abundance.

Nonetheless, repeat observations and experiments have elucidated a number of key processes that could serve as a basis for the inclusion of CDOM in a tracer-like manner in future modeling efforts. Nelson and Siegel (2013) review work to-date on the distribution

of CDOM in the global ocean and its sources and sinks. CDOM is known to be produced in both terrestrial and aquatic environments and degraded by microbial activity and solar bleaching. Although the details of each of these processes are not well known, they may serve the basis for first attempts in modeling. The inclusion of CDOM in models may be most appropriate on a regional scale, since these processes are specific to the molecular composition of DOM, physical circulation and microbial composition of the aquatic environment.

Future investigations, whether they be model simulations or field observations, should aim to understand the consequences of changing aquatic optical properties in the oceanic environment. Spectrally dependent water clarity exerts a primary control on biology and heating in aquatic environments. Studies of biogeochemical and ecological shifts in lakes may provide insight into the effects of large-scale yellowing in estuaries and the oceans. Understanding the role of shortwave heating in the stability of the mixed layer has implications for the sequestration of atmospheric CO_2 in regions where deep water is formed. Accurately modeling the vertical structure of shortwave heating is essential for model simulations projecting the future of sea ice.

Bibliography

Anderson, W., A. Gnanadesikan, R. Hallberg, J. Dunne, and B. Samuels, 2007: Impact of ocean color on the maintenance of the pacific cold tongue. *Geophysical Research Letters*, **34 (11)**.

Anderson, W., A. Gnanadesikan, and A. Wittenberg, 2009: Regional impacts of ocean color on tropical pacific variability. *Ocean Science*, **5 (3)**, 313–327, doi:10.5194/os-5-313-2009, URL http://www.ocean-sci.net/5/313/2009/.

Atkinson, A., V. Siegel, E. Pakhomov, and P. Rothery, 2004: Long-term decline in krill stock and increase in salps within the southern ocean. *Nature*, **432 (7013)**, 100–103.

Balch, W., T. Huntington, G. Aiken, D. Drapeau, B. Bowler, L. Lubelczyk, and K. Butler, 2016: Toward a quantitative and empirical dissolved organic carbon budget for the gulf of maine, a semienclosed shelf sea. *Global Biogeochemical Cycles*, **30 (2)**, 268–292, doi:10.1002/2015GB005332, URL http://dx.doi.org/10.1002/2015GB005332, 2015GB005332.

Ballabrera-Poy, J., R. Murtugudde, R. Zhang, and A. Busalacchi, 2007: Coupled ocean-

atmosphere response to seasonal modulation of ocean color: Impact on interannual climate simulations in the tropical pacific. *Journal of climate*, **20 (2)**, 353–374.

Blough, N. V., and R. D. Vecchio, 2002: Chapter 10: Chromophoric DOM in the coastal environment. *Biogeochemistry of Marine Dissolved Organic Matter*, D. A. Hansell, and C. A. Carlson, Eds., Academic Press, San Diego, 509 – 546, doi:http://dx.doi.org/10.1016/B978-012323841-2/50012-9, URL http://www.sciencedirect.com/science/article/pii/B9780123238412500129.

Bricaud, A., A. Morel, and L. Prieur, 1981: Absorption by dissolved organic matter of the sea (yellow substance) in the uv and visible domains. *Limnology and oceanography*, **26 (1)**, 43–53.

Broccoli, A. J., and S. A. Klein, 2010: Comment on "observational and model evidence for positive low-level cloud feedback". *Science*, **329 (5989)**, 277–277, doi:10.1126/science.1186796, URL http://science.sciencemag.org/content/329/5989/277.1, http://science.sciencemag.org/content/329/5989/277.1.full.pdf.

Carder, K. L., S. K. Hawes, K. A. Baker, R. C. Smith, R. G. Steward, and B. G. Mitchell, 1991: Reflectance model for quantifying chlorophyll a in the presence of productivity degradation products. *Journal of Geophysical Research: Oceans*, **96 (C11)**, 20 599–20 611, doi:10.1029/91JC02117, URL http://dx.doi.org/10.1029/91JC02117.

Clarke, G. L., G. C. Ewing, and C. J. Lorenzen, 1970: Spectra of backscattered light from the sea obtained from aircraft as a measure of chlorophyll concentra-

tion. *Science*, **167 (3921)**, 1119–1121, doi:10.1126/science.167.3921.1119, URL http://science.sciencemag.org/content/167/3921/1119, http://science.sciencemag.org/content/167/3921/1119.full.pdf.

Clement, A. C., R. Burgman, and J. R. Norris, 2009: Observational and model evidence for positive low-level cloud feedback. *Science*, **325 (5939)**, 460–464, doi:10.1126/science.1171255, URL http://science.sciencemag.org/content/325/5939/460, http://science.sciencemag.org/content/325/5939/460.full.pdf.

Coble, P. G., 2007: Marine optical biogeochemistry: The chemistry of ocean color. *Chemical Reviews*, **107 (2)**, 402–418, doi:10.1021/cr050350, URL http://dx.doi.org/10.1021/cr050350, pMID: 17256912, http://dx.doi.org/10.1021/cr050350.

Comiso, J. C., C. L. Parkinson, R. Gersten, and L. Stock, 2008: Accelerated decline in the Arctic sea ice cover. *Geophys. Res. Lett.*, **35 (1)**, L01 703, doi:10.1029/2007GL031972.

Dunne, J. P., R. A. Armstrong, A. Gnanadesikan, and J. L. Sarmiento, 2005: Empirical and mechanistic models for the particle export ratio. *Global Biogeochemical Cycles*, **19 (4)**, n/a–n/a, doi:10.1029/2004GB002390, URL http://dx.doi.org/10.1029/2004GB002390.

Dutkiewicz, S., A. E. Hickman, O. Jahn, W. W. Gregg, C. B. Mouw, and M. J. Follows, 2015: Capturing optically important constituents and properties in a marine biogeochemical and ecosystem model. *Biogeosciences*, **12 (14)**, 4447–4481, doi:10.5194/bg-12-4447-2015.

BIBLIOGRAPHY

Eppley, R., 1972: Temperature and phytoplankton growth in the sea. *Fishery Bulletin*, **70**, 1063–1085.

Field, C. B., M. J. Behrenfeld, J. T. Randerson, and P. Falkowski, 1998: Primary production of the biosphere: Integrating terrestrial and oceanic components. *Science*, **281 (5374)**, 237–240, doi:10.1126/science.281.5374.237, URL http://science. sciencemag.org/content/281/5374/237, http://science.sciencemag.org/content/281/5374/ 237.full.pdf.

Forel, F. A., 1890: Une nouvelle forme de la gamme de couleur pour l'étude de l'eau des lacs. *Archives des sciences physiques et naturelles/Societe de physique et d'histoire naturelle de geneve*, **6**, 25.

Galbraith, E. D., A. Gnanadesikan, J. P. Dunne, and M. R. Hiscock, 2010: Regional impacts of iron-light colimitation in a global biogeochemical model. *Biogeosciences*, **7 (3)**, 1043–1064, doi:10.5194/bg-7-1043-2010.

Galbraith, E. D., and Coauthors, 2011: Climate variability and radiocarbon in the cm2mc earth system model. *Journal of Climate*, **24 (16)**, 4230–4254.

Garcia, H. E., R. A. Locarnini, T. P. Boyer, J. I. Antonov, O. Baranova, M. Zweng, J. Reagan, and D. Johnson, 2014: World ocean atlas 2013, volume 4: Dissolved inorganic nutrients (phosphate, nitrate, silicate). Tech. Rep. 76.

Gnanadesikan, A., and W. G. Anderson, 2009: Ocean Water Clarity and the Ocean General

Circulation in a Coupled Climate Model. *J. Phys. Oceanogr.*, **39 (2)**, 314–332, doi:10.1175/2008JPO3935.1.

Gregg, W. W., and N. W. Casey, 2007: Modeling coccolithophores in the global oceans. *Deep Sea Research Part II: Topical Studies in Oceanography*, **54 (5–7)**, 447 – 477, doi:http://dx.doi.org/10.1016/j.dsr2.2006.12.007, URL http://www.sciencedirect.com/science/article/pii/S0967064507000318, the Role of Marine Organic Carbon and Calcite Fluxes in Driving Global Climate Change, Past and Future.

Gregg, W. W., and C. S. Rousseaux, 2014: Decadal trends in global pelagic ocean chlorophyll: A new assessment integrating multiple satellites, in situ data, and models. *Journal of Geophysical Research: Oceans*, **119 (9)**, 5921–5933, doi:10.1002/2014JC010158, URL http://dx.doi.org/10.1002/2014JC010158.

Griffies, S. M., and Coauthors, 2005: Formulation of an ocean model for global climate simulations. *Ocean Sci.*, **1**, 45–79, doi:10.5194/os-1-45-2005.

Griffin, C. G., K. E. Frey, J. Rogan, and R. M. Holmes, 2011: Spatial and interannual variability of dissolved organic matter in the kolyma river, east siberia, observed using satellite imagery. *Journal of Geophysical Research: Biogeosciences*, **116 (G3)**, n/a–n/a, doi:10.1029/2010JG001634, URL http://dx.doi.org/10.1029/2010JG001634, g03018.

Hill, V. J., 2008: Impacts of chromophoric dissolved organic material on surface ocean heating in the Chukchi Sea. *J. Geophys. Res.: Oceans*, **113 (C07024)**, doi:10.1029/2007JC004119.

Holland, M. M., M. C. Serreze, and J. Stroeve, 2010: The sea ice mass budget of the Arctic and its future change as simulated by coupled climate models. *Climate Dyn.*, **34 (2–3)**, 185–200, doi:10.1007/s00382-008-0493-4.

Jackson, J. M., E. C. Carmack, F. A. McLaughlin, S. E. Allen, and R. G. Ingram, 2010: Identification, characterization, and change of the near-surface temperature maximum in the Canada Basin, 1993–2008. *J. Geophys. Res.: Oceans*, **115**, C05 021, doi:10.1029/2009JC005265.

Jin, M., C. Deal, S. H. Lee, S. Elliott, E. Hunke, M. Maltrud, and N. Jeffery, 2012: Investigation of Arctic sea ice and ocean primary production for the period 1992–2007 using a 3-D global ice–ocean ecosystem model. *Deep Sea Res., Part II*, **81–84**, 28–35, doi:10.1016/j.dsr2.2011.06.003.

Kalle, K., 1938: Zum problem der meereswasserfarbe. *Ann. Hydrol. Mar. Mitt*, **66**, 1–13.

Kim, G. E., A. Gnanadesikan, and M.-A. Pradal, 2016: Increased surface ocean heating by colored detrital matter (cdm) linked to greater northern hemisphere ice formation in the gfdl cm2mc esm. *Journal of Climate*.

Kim, G. E., M.-A. Pradal, and A. Gnanadesikan, 2015: Quantifying the biological impact of surface ocean light attenuation by colored detrital matter in an esm using a new optical parameterization. *Biogeosciences*, **12 (16)**, 5119–5132, doi:10.5194/bg-12-5119-2015, URL http://www.biogeosciences.net/12/5119/2015/.

Kirk, J. T., 1994: *Light and photosynthesis in aquatic ecosystems*. Cambridge university press.

Lankford Jr, T. E., and T. E. Targett, 2001: Low-temperature tolerance of age-0 atlantic croakers: recruitment implications for us mid-atlantic estuaries. *Transactions of the American Fisheries Society*, **130 (2)**, 236–249.

Large, W. G., J. C. McWilliams, and S. C. Doney, 1994: Oceanic vertical mixing: A review and a model with a nonlocal boundary layer parameterization. *Reviews of Geophysics*, **32 (4)**, 363–403, doi:10.1029/94RG01872, URL http://dx.doi.org/10.1029/94RG01872.

Large, W. G., and S. G. Yeager, 2009: The global climatology of an interannually varying air–sea flux data set. *Climate Dynamics*, **33 (2)**, 341–364, doi:10.1007/s00382-008-0441-3, URL http://dx.doi.org/10.1007/s00382-008-0441-3.

Laxon, S., N. Peacock, and D. Smith, 2003: High interannual variability of sea ice thickness in the Arctic region. *Nature*, **425**, 947–950, doi:10.1038/nature02050.

Le Quéré, C., and Coauthors, 2015: Global carbon budget 2015. *Earth System Science Data*, **7 (2)**, 349–396, doi:10.5194/essd-7-349-2015, URL http://www.earth-syst-sci-data.net/7/349/2015/.

Lengaigne, M., G. Madec, L. Bopp, C. Menkes, O. Aumont, and P. Cadule, 2009: Biophysical feedbacks in the Arctic Ocean using an Earth system model. *Geophys. Res. Lett.*, **36 (21)**, L21 602, doi:10.1029/2009GL040145.

Lindsay, R. W., and J. Zhang, 2005: The thinning of arctic sea ice, 1988–2003: Have we passed a tipping point? *Journal of Climate*, **18 (22)**, 4879–4894, doi:10.1175/JCLI3587. 1, URL http://dx.doi.org/10.1175/JCLI3587.1, http://dx.doi.org/10.1175/JCLI3587.1.

Liu, J., J. A. Curry, and Y. Hu, 2004: Recent arctic sea ice variability: Connections to the arctic oscillation and the enso. *Geophysical Research Letters*, **31 (9)**, doi:10.1029/ 2004GL019858, URL http://dx.doi.org/10.1029/2004GL019858, l09211.

Manizza, M., C. Le Quéré, A. J. Watson, and E. T. Buitenhuis, 2005: Bio-optical feedbacks among phytoplankton, upper ocean physics and sea-ice in a global model. *Geophys. Res. Lett.*, **32 (5)**, L05 603, doi:10.1029/2004GL020778.

Mann, P. J., T. I. Eglinton, C. P. McIntyre, N. Zimov, A. Davydova, J. E. Vonk, R. M. Holmes, and R. G. M. Spencer, 2015: Utilization of ancient permafrost carbon in headwaters of arctic fluvial networks. *Nat Commun*, **6**, URL http://dx.doi.org/10.1038/ ncomms8856.

Maritorena, S., D. A. Siegel, and A. R. Peterson, 2002: Optimization of a semianalytical ocean color model for global-scale applications. *Appl. Opt.*, **41 (15)**, 2705–2714, doi: 10.1364/AO.41.002705, URL http://ao.osa.org/abstract.cfm?URI=ao-41-15-2705.

Matsuoka, A., V. Hill, Y. Huot, M. Babin, and A. Bricaud, 2011: Seasonal variability in the light absorption properties of western arctic waters: Parameterization of the individual components of absorption for ocean color applications. *Journal of Geophysical Re-*

search: Oceans, **116 (C2)**, doi:10.1029/2009JC005594, URL http://dx.doi.org/10.1029/ 2009JC005594, c02007.

Matsuoka, A., Y. Huot, K. Shimada, S. I. Saitoh, and M. Babin, 2007: Bio-optical characteristics of the western Arctic Ocean: Implications for ocean color algorithms. *Can. J. Remote Sens.*, **33 (6)**, 503–518, doi:10.5589/m07-059.

McGowan, J. A., D. R. Cayan, and L. M. Dorman, 1998: Climate-ocean variability and ecosystem response in the northeast pacific. *Science*, **281 (5374)**, 210–217.

Mitchell, B. G., 1992: Predictive bio-optical relationships for polar oceans and marginal ice zones. *Journal of Marine Systems*, **3 (1–2)**, 91–105, doi:http://dx.doi.org/10.1016/ 0924-7963(92)90032-4.

Mobley, C. D., 1994: *Light and water: radiative transfer in natural waters*. Academic press.

Mobley, C. D., 2011: Fast light calculations for ocean ecosystem and inverse models. *Opt. Express*, **19 (20)**, 18 927–18 944, doi:10.1364/OE.19.018927.

Mobley, C. D., F. Chai, P. Xiu, and L. K. Sundman, 2015: Impact of improved light calculations on predicted phytoplankton growth and heating in an idealized upwelling-downwelling channel geometry. *J. Geophys. Res.: Oceans*, **120 (2)**, 875–892, doi: 10.1002/2014JC010588.

Morel, A., 1988: Optical modeling of the upper ocean in relation to its biogenous matter

content (case i waters). *Journal of Geophysical Research: Oceans*, **93 (C9)**, 10 749–10 768, doi:10.1029/JC093iC09p10749.

Murtugudde, R., J. Beauchamp, C. R. McClain, M. Lewis, and A. J. Busalacchi, 2002: Effects of Penetrative Radiation on the Upper Tropical Ocean Circulation. *J. Climate*, **15 (5)**, 470–486, doi:10.1175/1520-0442(2002)015⟨0470:EOPROT⟩2.0.CO;2.

Nelson, N. B., C. A. Carlson, and D. K. Steinberg, 2004: Production of chromophoric dissolved organic matter by sargasso sea microbes. *Marine Chemistry*, **89 (1–4)**, 273 – 287, doi:http://dx.doi.org/10.1016/j.marchem.2004.02.017, URL http://www.sciencedirect.com/science/article/pii/S0304420304000933, {CDOM} in the Ocean: Characterization, Distribution and Transformation.

Nelson, N. B., and D. A. Siegel, 2013: The global distribution and dynamics of chromophoric dissolved organic matter. *Annual Review of Marine Science*, **5 (1)**, 447–476, doi:10.1146/annurev-marine-120710-100751, URL http://www.annualreviews.org/doi/abs/10.1146/annurev-marine-120710-100751, pMID: 22809178, http://www.annualreviews.org/doi/pdf/10.1146/annurev-marine-120710-100751.

Nelson, N. B., D. A. Siegel, C. A. Carlson, and C. M. Swan, 2010: Tracing global biogeochemical cycles and meridional overturning circulation using chromophoric dissolved organic matter. *Geophysical Research Letters*, **37 (3)**, n/a–n/a, doi:10.1029/2009GL042325, URL http://dx.doi.org/10.1029/2009GL042325.

Ohlmann, J. C., and D. A. Siegel, 2000: Ocean radiant heating. part ii: Parameterizing

solar radiation transmission through the upper ocean. *Journal of Physical Oceanography*, **30 (8)**, 1849–1865, doi:10.1175/1520-0485(2000)030⟨1849:ORHPIP⟩2.0.CO;2.

Oschlies, A., 2004: Feedbacks of biotically induced radiative heating on upper-ocean heat budget, circulation, and biological production in a coupled ecosystem-circulation model. *Journal of Geophysical Research: Oceans*, **109 (C12)**, n/a–n/a, doi:10.1029/2004JC002430, URL http://dx.doi.org/10.1029/2004JC002430, c12031.

Patara, L., M. Vichi, S. Masina, P. Fogli, and E. Manzini, 2012: Global response to solar radiation absorbed by phytoplankton in a coupled climate model. *Climate Dynamics*, **39 (7/8)**, 1951 – 1968.

Pegau, W. S., 2002: Inherent optical properties of the central Arctic surface waters. *J. Geophys. Res.: Oceans*, **107 (C10)**, SHE 16–1–SHE 16–7, doi:10.1029/2000JC000382.

Peterson, B. J., R. M. Holmes, J. W. McClelland, C. J. Vörösmarty, R. B. Lammers, A. I. Shiklomanov, I. A. Shiklomanov, and S. Rahmstorf, 2002: Increasing river discharge to the Arctic Ocean. *Science*, **298 (5601)**, 2171–2173, doi:10.1126/science.1077445.

Pope, R. M., and E. S. Fry, 1997: Absorption spectrum (380–700 nm) of pure water. ii. integrating cavity measurements. *Appl. Opt.*, **36 (33)**, 8710–8723, doi:10.1364/AO.36.008710, URL http://ao.osa.org/abstract.cfm?URI=ao-36-33-8710.

Reynolds, R. W., N. A. Rayner, T. M. Smith, D. C. Stokes, and W. Wang, 2002: An improved in situ and satellite sst analysis for climate. *Journal of Climate*, **15 (13)**,

1609–1625, doi:10.1175/1520-0442(2002)015⟨1609:AIISAS⟩2.0.CO;2, URL http://dx.doi.org/10.1175/1520-0442(2002)015⟨1609:AIISAS⟩2.0.CO;2, http://dx.doi.org/10.1175/1520-0442(2002)015⟨1609:AIISAS⟩2.0.CO;2.

Sarmiento, J. L., and N. Gruber, 2006: *Ocean Biogeochemical Dynamics*. Princeton University Press.

Sarmiento, J. L., and Coauthors, 2004: Response of ocean ecosystems to climate warming. *Global Biogeochemical Cycles*, **18 (3)**, n/a–n/a, doi:10.1029/2003GB002134, URL http://dx.doi.org/10.1029/2003GB002134.

Sathyendranath, S., and T. Platt, 1988: The spectral irradiance field at the surface and in the interior of the ocean: a model for applications in oceanography and remote sensing. *Journal of Geophysical Research: Oceans*, **93 (C8)**, 9270–9280.

Serreze, M. C., and Coauthors, 2000: Observational evidence of recent change in the northern high-latitude environment. *Clim. Change*, **46 (1-2)**, 159–207, doi:10.1023/A:1005504031923.

Sharpless, C. M., and N. V. Blough, 2014: The importance of charge-transfer interactions in determining chromophoric dissolved organic matter (cdom) optical and photochemical properties. *Environ. Sci.: Processes Impacts*, **16**, 654–671, doi:10.1039/C3EM00573A, URL http://dx.doi.org/10.1039/C3EM00573A.

Siegel, D. A., S. Maritorena, N. B. Nelson, and M. J. Behrenfeld, 2005a: Independence

and interdependencies among global ocean color properties: Reassessing the bio-optical assumption. *Journal of Geophysical Research: Oceans*, **110 (C7)**, n/a–n/a, doi:10.1029/ 2004JC002527, URL http://dx.doi.org/10.1029/2004JC002527.

Siegel, D. A., S. Maritorena, N. B. Nelson, M. J. Behrenfeld, and C. R. McClain, 2005b: Colored dissolved organic matter and its influence on the satellite-based characterization of the ocean biosphere. *Geophysical Research Letters*, **32 (20)**, n/a–n/a, doi:10.1029/ 2005GL024310, l20605.

Spencer, R. G. M., P. J. Mann, T. Dittmar, T. I. Eglinton, C. McIntyre, R. M. Holmes, N. Zimov, and A. Stubbins, 2015: Detecting the signature of permafrost thaw in arctic rivers. *Geophysical Research Letters*, **42 (8)**, 2830–2835, doi:10.1002/2015GL063498, URL http://dx.doi.org/10.1002/2015GL063498, 2015GL063498.

Stedmon, C., R. Amon, A. Rinehart, and S. Walker, 2011: The supply and characteristics of colored dissolved organic matter (cdom) in the arctic ocean: Pan arctic trends and differences. *Marine Chemistry*, **124 (1–4)**, 108 – 118, doi:http://dx. doi.org/10.1016/j.marchem.2010.12.007, URL http://www.sciencedirect.com/science/ article/pii/S0304420311000065.

Strong, A., F. Arzayus, W. Skirving, and S. Heron, 2006: Identifying coral bleaching remotely via coral reef watch–improved integration and implications for changing climate. *Coral Reefs and Climate Change: Science and Management*, 163–180.

Troen, I. B., and L. Mahrt, 1986: A simple model of the atmospheric boundary layer;

sensitivity to surface evaporation. *Boundary-Layer Meteorology*, **37 (1)**, 129–148, doi: 10.1007/BF00122760, URL http://dx.doi.org/10.1007/BF00122760.

Ule, W., 1892: Die bestimmung der wasserfarbe in den seen. *Kleinere Mittheilungen. Dr. A. Petermanns Mittheilungen aus Justus Perthes geographischer Anstalt*, 70–71.

Welch, D. W., Y. Ishida, and K. Nagasawa, 1998: Thermal limits and ocean migrations of sockeye salmon (oncorhynchus nerka): long-term consequences of global warming. *Canadian Journal of Fisheries and Aquatic Sciences*, **55 (4)**, 937–948.

Werdell, P. J., and S. W. Bailey, 2005: An improved in-situ bio-optical data set for ocean color algorithm development and satellite data product validation. *Remote Sensing of Environment*, **98 (1)**, 122–140, doi:10.1016/j.rse.2005.07.001.

Wernand, M. R., H. J. van der Woerd, and W. W. C. Gieskes, 2013: Trends in ocean colour and chlorophyll concentration from 1889 to 2000, worldwide. *PLoS ONE*, **8 (6)**, 1–20, doi:10.1371/journal.pone.0063766, URL http://dx.doi.org/10.1371%2Fjournal.pone.0063766.

Wetzel, P., E. Maier-Reimer, M. Botzet, J. Jungclaus, N. Keenlyside, and M. Latif, 2006: Effects of Ocean Biology on the Penetrative Radiation in a Coupled Climate Model. *J. Climate*, **19 (16)**, 3973–3987, doi:10.1175/JCLI3828.1.

Williamson, C. E., E. P. Overholt, R. M. Pilla, T. H. Leach, J. A. Brentrup, L. B. Knoll,

1785   E. M. Mette, and R. E. Moeller, 2015: Ecological consequences of long-term browning

1786   in lakes. *Scientific reports*, **5**.

1787   Winton, M., 2000: A Reformulated Three-Layer Sea Ice Model. *J. Atmos. Oceanic Tech-*

1788   *nol.*, **17 (4)**, 525–531, doi:10.1175/1520-0426(2000)017⟨0525:ARTLSI⟩2.0.CO;2.

1789   Yoder, J. A., and M. A. Kennelly, 2003: Seasonal and enso variability in global ocean

1790   phytoplankton chlorophyll derived from 4 years of seawifs measurements. *Global Bio-*

1791   *geochemical Cycles*, **17 (4)**, n/a–n/a, doi:10.1029/2002GB001942, URL http://dx.doi.

1792   org/10.1029/2002GB001942.

Vita
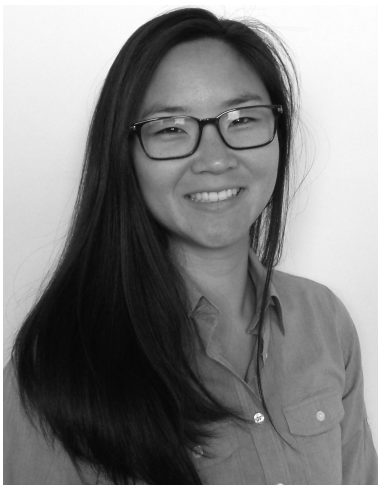
Grace E. Kim received the B. A. degree from Columbia University in 2009, and enrolled in the Department of Earth and Planetary Sciences Ph.D. program at Johns Hopkins University in 2012. She received a NASA Earth Science Foundation Graduate Research Fellowship in 2014. Her research focuses on the role of light in water on biogeochemistry and hydrodynamics in marine environments. Starting in January 2017, Grace will work as a postdoctoral researcher at the NASA Goddard Space Flight Center as an awardee of the NASA Postdoctoral Program, where she will investigate opportunities for satellite detection of marine microbial community assemblages using hyperspectral optical sensors.